RELEASE DATE:
APR 25 1950

Restriction/
Classification
Cancelled

CLASSIFICATION CANCELLED

CONFIDENTIAL

RM SA50D05

5525.4
Northrop
5511-A

NACA RM SA50D05

NACA

CLASSIFICATION CANCELLED

RESEARCH MEMORANDUM

for the

Air Materiel Command, U. S. Air Force

TESTS OF A NORTHROP XSSM-A-3 MISSILE IN THE

AMES 40- BY 80-FOOT WIND TUNNEL.-

STABILITY AND CONTROL

By Ralph L. Maki

Ames Aeronautical Laboratory
Moffett Field, Calif.

CLASSIFICATION CANCELLED

NATIONAL ADVISORY COMMITTEE
FOR AERONAUTICS

WASHINGTON

April 5, 1950

CONFIDENTIAL

CLASSIFICATION CANCELLED

NATIONAL ADVISORY COMMITTEE FOR AERONAUTICS

RESEARCH MEMORANDUM

for the

Air Materiel Command, U. S. Air Force

TESTS OF A NORTHROP XSSM-A-3 MISSILE IN THE AMES 40- BY 80-FOOT WIND TUNNEL.- STABILITY AND CONTROL

By Ralph L. Maki

SUMMARY

This report presents the results of wind-tunnel force tests which were conducted to determine the low-speed stability and control characteristics of a full-scale Northrop XSSM-A-3 missile. Tests were made through a range of angles of attack, sideslip, and control deflection, and at various Reynolds numbers. Characteristics of the complete missile are compared with the characteristics of the missile with the landing skids extended, with the vertical tail removed, and with the fuselage alone. No analysis of the data has been made in order to make the results available as soon as possible.

INTRODUCTION

At the request of the Air Materiel Command, U. S. Air Force, an investigation of the low-speed stability and control characteristics of a full-scale Northrop XSSM-A-3 missile was made. The first part of the investigation, reported in reference 1, consisted of tests of the missile with various wing modifications designed to extend the stable portion of the pitching-moment-coefficient curve to lift coefficients above 0.6. The final configuration chosen had a wing with an increased leading-edge radius. The present report gives the results of stability and control tests of this final configuration, hereinafter referred to as the missile.

NOTATION

The results of the tests are presented as standard NACA coefficients of forces and moments. All force data are referred to the wind axes, and all moment data are referred to the stability axes. The coefficients and symbols are defined below and in figure 1:

A aspect ratio $\left(\frac{b^2}{S}\right)$

b wing span, measured perpendicular to the plane of symmetry of the missile, feet

c wing chord, measured perpendicular to the 40-percent-chord line, feet

c_s wing chord, measured parallel to the plane of symmetry of the missile, feet

$\overline{c_s}$ mean aerodynamic chord, measured parallel to the plane of symmetry of the missile $\left(\frac{\int_0^{b/2} c_s^2\,dy}{\int_0^{b/2} c_s\,dy}\right)$, feet

C_D drag coefficient $\left(\frac{\text{drag}}{qS}\right)$

C_{D_T} increment of drag coefficient due to wind-tunnel-wall interference

C_L lift coefficient $\left(\frac{\text{lift}}{qS}\right)$

C_l rolling-moment coefficient $\left(\frac{\text{rolling moment}}{qSb}\right)$

C_m pitching-moment coefficient $\left(\frac{\text{pitching moment}}{qS\overline{c_s}}\right)$

C_n yawing-moment coefficient $\left(\frac{\text{yawing moment}}{qSb}\right)$

C_Y side-force coefficient $\left(\frac{\text{side force}}{qS}\right)$

q free-stream dynamic pressure, pounds per square foot

R Reynolds number $\left(\frac{V\overline{c_s}}{\nu}\right)$

S wing area, square feet

V free-stream velocity, feet per second

y spanwise distance outboard from wing center line, feet

α free-stream angle of attack, with reference to the wing-chord plane, degrees

α_T increment of angle of attack due to wind-tunnel-wall interference, degrees

β angle of sideslip, degrees

δ_e deflection of both elevons, measured perpendicular to the hinge line, degrees

δ_f trailing-edge split-flap deflection, measured perpendicular to the hinge line, degrees

δ_l deflection of the left elevon, measured perpendicular to the hinge line, degrees

δ_r deflection of the right elevon, measured perpendicular to the hinge line, degrees

ν kinematic viscosity, square feet per second

DESCRIPTION OF MISSILE AND APPARATUS

The investigation was conducted in the Ames 40- by 80-foot wind tunnel. A three-view drawing of the full-scale Northrop XSSM-A-3 missile used in these tests is shown in figure 2, with additional dimensional data given in table I. The wing dimensions are those of the original missile without the leading-edge-radius modification. The differences in the dimensions for wing span and area between table I and figure 2 are due to the neglect of the rounded wing tips for the data of figure 2.

As a result of the longitudinal-stability tests reported in reference 1, the missile was modified by increasing the leading-edge radius of the wing. The original airfoil sections perpendicular to the 40-percent-chord line were NACA 65-009 sections, modified by fairing straight lines from the 66-percent-chord point to the trailing edge. The profile and coordinates of the original section, together with the increased leading-edge radius, are given in figure 3. The increased leading-edge radius added 2.18 square feet of area to the original 300 square feet, and also introduced a slight amount of camber into the originally symmetrical section.

Photographs of the various configurations tested are shown in figure 4. Views of the model installed in the tunnel are shown in figures 4(a) and 4(b). The inboard trailing-edge flaps with which the wing was equipped are shown in figure 4(c). For most of the tests the tail exit pipe was faired over, with a camera box mounted upon a platform to the rear of the vertical tail. The camera was used in conjunction with several deflection target posts installed on the upper surface of the left wing panel (fig. 4(d)). Unless otherwise indicated, the target posts were removed for the tests. The NACA submerged-type duct inlet on the bottom surface of the fuselage was faired over, except as otherwise indicated. The small deflectors around the inlet were left on and are visible in figures 4(a) and 4(b). Figure 4(e) shows the duct inlet open. One series of tests was made with the landing skids extended as shown in figure 4(f). For tests of the fuselage alone, the wing, the vertical tail, and the nose boom were removed (fig. 4(g)). A faired tail cone, used in studies of the effects of the component parts of the missile, replaced the aft end of the fuselage from a station forward of the vertical tail (figs. 4(h) and 5). Slab-sided elevons, used in one test, were made of wood which fitted directly over the original elevons (figs. 4(i) and 6).

For the majority of the tests the elevons were operated by remotely controlled servo units. The elevons were divided approximately at their midspan positions to relieve possible binding along the hinge line from aeroelastic effects. When used as elevators, both elevons were operated simultaneously by a single drive, but calibrated potentiometers measured the actual deflection of each portion of both elevons near their inboard ends, giving four deflection readings at each test condition. Due to play in the system, the deflections of the four elevon panels varied at a given setting, and the average deflection was held as closely as possible to the desired value. When used as ailerons, one elevon was clamped in a fixed position and the other was remotely controlled.

Measurements were taken to check the inclination of the wing-chord plane. A bubble-type protractor was read at various spanwise stations on the upper surface of the wing near the trailing edge. Approximately 1.2° of washin of the right wing tip relative to the left was found.

TESTS AND RESULTS

An outline of the test conditions and the configurations investigated is given in table II, which also serves as an index to the test results which are presented in figures 7 to 41. The majority of the tests were made at a dynamic pressure of 72 pounds per square foot, with some tests at dynamic pressures of 25, 48, 99, and 113. The Reynolds numbers were approximately 6, 9, 11, 12.5, and 13.5×10^6, based on the mean aerodynamic chord. For tests of the missile in pitch, the maximum angle of attack tested at the higher dynamic pressures was limited by the allowable stress on the support fittings on the fuselage of the missile.

The dimensions of the missile as listed in table I were used to reduce the data to coefficient form. The slight changes in wing area and length and location of the mean aerodynamic chord, due to the increased leading-edge radius added to the wing, were neglected in the computation of the coefficients. The pitching moments are referred to a moment center 1 inch above the fuselage longitudinal axis and 256.81 inches aft of the fuselage nose, or at the fore-and-aft position corresponding to the quarter chord of the mean aerodynamic chord.

As explained in reference 1, the interference effects between the fuselage and support fittings and the drag of the fittings in the presence of the wing are unknown. Therefore, no drag or pitching-moment tares were applied to the data. The drag tare of the exposed part of the support-strut tips and ball sockets, without a model in the tunnel, is of the order of 0.0046 based on the wing dimensions of the missile. The camera box gave an increment of drag of 0.0028 at zero angle of attack. Corrections for stream-angle inclination and wind-tunnel-wall interference have been applied to the measured angles of attack and drag coefficients. The wall-interference corrections were as follows:

$$\alpha_T = 0.598\ C_L$$

$$C_{D_T} = 0.0104\ C_L{}^2$$

During the investigation of reference 1 an attempt was made to determine the source of the apparent scatter of the pitching-moment-coefficient data. Test points are computed by averaging five separate balance readings taken at approximately 5-second intervals for each test condition. Variations in C_m as high as 0.01 from the mean value were found in coefficients computed for each of the five separate balance readings at a given test condition. In the present investigation variations approaching 0.015 were occasionally found by this method. The possibility of abnormal scatter in all coefficients during the tests with variable elevons was similarly studied, with the following probable maximum variations being indicated:

$$\Delta C_L,\ \pm 0.010;\ \Delta C_m,\ \pm 0.010;\ \Delta C_D,\ \pm 0.001$$

$$\Delta C_Y,\ \pm 0.003;\ \Delta C_l,\ \pm 0.003;\ \Delta C_n,\ \pm 0.001$$

The scatter was apparently due to (1) the required narrow lift-strut mounting which allowed a slight yawing oscillation of the model, and (2) the drifting of the elevons from their initial settings during the 20-second interval required to obtain the five balance readings at a given test condition.

Variations in the deflections of the four elevon panels at a given nominal setting also contributed to the scatter of the data. In the tests with variable elevon deflections, a study of the probable differences in the four separate elevon deflection readings indicated that the deviations from the average reading was usually within 2° with occasional points deviating as much as 4°. In the tests at constant nominal elevon deflection, the variation in the readings was noticeably less, usually within 0.5° of the mean value. In all the tests the readings showed that the left elevon was usually more positively deflected than the right elevon. In all cases the average of the four readings was used to plot the data. For the data presented in figures 9, 10, and 11, the elevons were clamped at the proper deflections to help reduce the scatter of the data.

In order to show more clearly the Reynolds number effects on the drag coefficient, cross plots of data selected from figure 7 were made with a magnified drag-coefficient scale (fig. 8).

Photographic studies of the aeroelastic bending and twist are not presented, but concurrently taken force and moment data are included (figs. 29 to 35) to show the effects of the deflection target posts on the characteristics of the missile.

In the tests of the missile with the NACA submerged-type duct inlet open (fig. 36), the internal drag coefficient of the duct was not evaluated but was of the order of 0.0015, maximum, throughout the lift-coefficient range. This estimate was made from the results of studies of the internal drag of the duct on the fuselage alone with a modified tail exit pipe.

Ames Aeronautical Laboratory,
National Advisory Committee for Aeronautics,
Moffett Field, Calif.

REFERENCE

1. Graham, David: Tests of the Northrop XSSM-A-3 Missile in the Ames 40- by 80-Foot Wind Tunnel.- Wing Modifications. NACA RM SA50A05, 1950.

TABLE I.- GEOMETRIC DATA OF THE MISSILE

Wing	
Span, feet	42.26
Area, square feet	300
Mean aerodynamic chord, feet	7.51
Angle of incidence, degrees	0
Aspect ratio	6
Taper ratio	0.4
Fuselage	
Length, feet	52.67
Maximum diameter, feet	4.83

TABLE II.- SUMMARY OF CONFIGURATIONS TESTED

Figure	Configuration	Angle of attack, α, approximate (deg)	Angle of sideslip, β (deg)	[a]Control deflection (deg)	Reynolds number	Data presented
7	[b]Final	Variable	0	5, 0, −5, −10, −15, −18	6.4, 9, 11, 12.5, and 13.4×10^6	C_L vs C_D, α, C_m
8		0, 2, 4, 6, 8, 10, 12		0, −10, −18		C_D vs R
9		0, 3, 7, 10	Variable	0	11×10^6	C_D, C_L, C_m, C_Y, C_l, C_n vs β
10				−10		
11		Variable	−10	0, −10		C_L vs C_D, α, C_m, C_Y, C_l, C_n
12		0, 3, 7, 10	0	Variable	11 and 12.5×10^6	C_D, C_L, C_m vs δ_e
13	Final + δ_f, 15°					
14	Final + δ_f, 45°				11×10^6	
15	Final + slab-sided elevons				11 and 12.5×10^6	
16	Final		−3		11×10^6	C_D, C_L, C_m, C_Y, C_l, C_n vs δ_e
17			−7			
18			−10			
19			3			
20			7			
21			10			

[a]Unless otherwise specified, control deflection refers to both elevons.

[b]Final refers to the missile with the wing with increased leading-edge radius.

TABLE II. - CONTINUED

Figure	Configuration	Angle of attack, α, approximate (deg)	Angle of sideslip, β (deg)	[a]Control deflection (deg)	Reynolds number	Data presented
22	Final	–	0	δ_r, 0; δ_l variable	11×10^6	C_D, C_L, C_m, C_Y, C_l, C_n vs δ_l
23		0, 3, 7, 10	-3			
24			-7			
25			-10			
26			3			
27			7			
28			10			
29	Final + deflection target posts	Variable	0	0 -10 -18	11 and 13.4×10^6	C_L vs C_D, α, C_m
30		0, 3, 7, 10	Variable	0	11×10^6	C_D, C_L, C_m, C_Y, C_l, C_n vs β
31				0	12.5×10^6	
32				-10	11×10^6	
33				-10	12.5×10^6	
34				δ_r, 0; δ_l, -10	11×10^6	
35				δ_l, 15	11×10^6	
36	Final and final with duct open	Variable	0	0	9×10^6	C_L vs C_D, α, C_m
37	Final and final with skids extended			-10	13.4×10^6	

TABLE II. - CONCLUDED

Figure	Configuration	Angle of attack, α, approximate (deg)	Angle of sideslip, β (deg)	[a]Control deflection (deg)	Reynolds number	Data presented
38	Final, final without vertical tail, and fuselage alone	0	Variable	0	11×10^6	C_D, C_L, C_m, C_Y, C_l, C_n vs β
39		3				
40		7				
41		10				

FIGURE LEGENDS

Figure 1.– Sign convention for the standard NACA coefficients. The forces, moments, angles, and control-surface deflections are shown as positive.

Figure 2.– Three-view drawing of the Northrop XSSM-A-3 missile.

Figure 3.– Profile and coordinates of the NACA 65-009 (mod.) airfoil section with increased nose radius.

Figure 4.– Views of the Northrop XSSM-A-3 missile as installed in the Ames 40- by 80-foot wind tunnel. (a) Front view of the missile.

Figure 4.– Continued. (b) Rear view of the missile.

Figure 4.– Continued. (c) Close-up of the lower surface of the right wing showing the trailing-edge split flaps deflected 45°.

Figure 4.– Continued. (d) View showing the deflection target posts on the left wing panel and the camera position on the missile.

Figure 4.– Continued. (e) Close-up of the fuselage with the duct inlet open.

Figure 4.– Continued. (f) Side view showing the landing skids extended.

Figure 4.– Continued. (g) Front view of the fuselage alone.

Figure 4.– Continued. (h) Rear view of the missile with the vertical tail removed.

Figure 4.– Concluded. (i) Close-up of the lower surface of the left wing showing the slab-sided elevons.

Figure 5.– Details of the faired tail cone.

Figure 6.– Details of the slab-sided elevons.

Figure 7.– Aerodynamic characteristics in pitch of the missile with various fixed elevon deflections and at various Reynolds numbers. β, 0°. (a) δ_l, 5°.

Figure 7.– Continued. (b) δ_e, 0°.

Figure 7.– Continued. (c) δ_e, -5°.

Figure 7.– Continued. (d) δ_e, -10°.

Figure 7.– Continued. (e) δ_e, -15°.

Figure 7.– Concluded. (f) δ_e, -18° (approx.).

Figure 8.– Reynolds number effect on the drag coefficient of the missile at several angles of attack. β, 0°. (a) δ_e, 0°.

Figure 8.– Continued. (b) δ_e, -10°.

Figure 8.– Concluded. (c) δ_e, -18° (approx.).

Figure 9.– Aerodynamic characteristics in sideslip of the missile at several angles of attack. R, 11×10^6; δ_e, 0°. (a) C_D, C_L, C_m vs β.

Figure 9.– Concluded. (b) C_Y, C_l, C_n vs β.

Figure 10.– Aerodynamic characteristics in sideslip of the missile at several angles of attack. R, 11×10^6; δ_e, -10°. (a) C_D, C_L, C_m vs β.

Figure 10.– Concluded. (b) C_Y, C_l, C_n vs β.

Figure 11.– Aerodynamic characteristics in pitch of the missile with fixed elevon deflections. R, 11×10^6; β, -10°. (a) C_L vs C_D, α, C_m.

Figure 11.– Concluded. (b) C_L vs C_Y, C_l, C_n.

Figure 12.– Variation, with elevon deflection, of the aerodynamic characteristics of the missile at several angles of attack. β, 0°. (a) R, 11×10^6.

Figure 12.– Concluded. (b) R, 12.5×10^6.

Figure 13.– Variation, with elevon deflection, of the aerodynamic characteristics of the missile at several angles of attack with trailing-edge flaps deflected 15°. β, 0°. (a) R, 11×10^6.

Figure 13.– Concluded. (b) R, 12×10^6.

Figure 14.– Variation, with elevon deflection, of the aerodynamic characteristics of the missile at several angles of attack with trailing-edge flaps deflected 45°. β, 0°; R, 11×10^6.

Figure 15.– Variation, with elevon deflection, of the aerodynamic characteristics of the missile at several angles of attack with slab-sided elevons. β, 0°. (a) R, 11×10^6.

Figure 15.– Concluded. (b) R, 12.5×10^6.

Figure 16.– Variation, with elevon deflection, of the aerodynamic characteristics of the missile at several angles of attack. R, 11×10^6; β, -3°. (a) C_D, C_L, C_m vs δ_e.

Figure 16.– Concluded. (b) C_Y, C_l, C_n vs δ_e.

Figure 17.– Variation, with elevon deflection, of the aerodynamic characteristics of the missile at several angles of attack. R, 11×10^6; β, -7°. (a) C_D, C_L, C_m vs δ_e.

Figure 17.– Concluded. (b) C_Y, C_l, C_n vs δ_e.

Figure 18.– Variation, with elevon deflection, of the aerodynamic characteristics of the missile at several angles of attack. R, 11×10^6; β, -10°. (a) C_D, C_L, C_m vs δ_e.

Figure 18.– Concluded. (b) C_Y, C_l, C_n vs δ_e.

Figure 19.– Variation, with elevon deflection, of the aerodynamic characteristics of the missile at several angles of attack. R, 11×10^6; β, 3°. (a) C_D, C_L, C_m vs δ_e.

Figure 19.– Concluded. (b) C_Y, C_l, C_n vs δ_e.

Figure 20.– Variation, with elevon deflection, of the aerodynamic characteristics of the missile at several angles of attack. R, 11×10^6; β, 7°. (a) C_D, C_L, C_m vs δ_e.

Figure 20.– Concluded. (b) C_Y, C_l, C_n vs δ_e.

Figure 21.– Variation, with elevon deflection, of the aerodynamic characteristics of the missile at several angles of attack. R, 11×10^6; β, 10°. (a) C_D, C_L, C_m vs δ_e.

Figure 21.– Concluded. (b) C_Y, C_l, C_n vs δ_e.

Figure 22.– Variation, with left elevon deflection, of the aerodynamic characteristics of the missile at several angles of attack. δ_r, 0°; R, 11×10^6; β, 0°. (a) C_D, C_L, C_m vs δ_l.

Figure 22.– Concluded. (b) C_Y, C_l, C_n vs δ_l.

Figure 23.– Variation, with left elevon deflection, of the aerodynamic characteristics of the missile at several angles of attack. δ_r, 0°; R, 11×10^6; β, -3°. (a) C_D, C_L, C_m vs δ_l.

Figure 23.– Concluded. (b) C_Y, C_l, C_n vs δ_l.

Figure 24.– Variation, with left elevon deflection, of the aerodynamic characteristics of the missile at several angles of attack. δ_r, 0°; R, 11×10^6; β, -7°. (a) C_D, C_L, C_m vs δ_l.

Figure 24.– Concluded. (b) C_Y, C_l, C_n vs δ_l.

Figure 25.– Variation, with left elevon deflection, of the aerodynamic characteristics of the missile at several angles of attack. δ_r, 0°; R, 11×10^6; β, -10°. (a) C_D, C_L, C_m vs δ_l.

Figure 25.– Concluded. (b) C_Y, C_l, C_n vs δ_l.

Figure 26.– Variation, with left elevon deflection, of the aerodynamic characteristics of the missile at several angles of attack. δ_r, 0°; R, 11×10^6; β, 3°. (a) C_D, C_L, C_m vs δ_l.

Figure 26.– Concluded. (b) C_Y, C_l, C_n vs δ_l.

Figure 27.– Variation, with left elevon deflection, of the aerodynamic characteristics of the missile at several angles of attack. δ_r, 0°; R, 11×10^6; β, 7°. (a) C_D, C_L, C_m vs δ_l.

Figure 27.– Concluded. (b) C_Y, C_l, C_n vs δ_l.

Figure 28.– Variation, with left elevon deflection, of the aerodynamic characteristics of the missile at several angles of attack. δ_r, 0°; R, 11×10^6; β, 10°. (a) C_D, C_L, C_m vs δ_l.

Figure 28.– Concluded. (b) C_Y, C_l, C_n vs δ_l.

Figure 29.– Aerodynamic characteristics in pitch of the missile with deflection target posts on the left wing panel. Two Reynolds numbers; β, 0°. (a) δ_e, 0°.

Figure 29.– Continued. (b) δ_e, -10°.

Figure 29.– Concluded. (c) δ_e, -18°.

Figure 30.– Aerodynamic characteristics in sideslip of the missile at several angles of attack with deflection target posts on the left panel. δ_e, 0°; R, 11×10^6. (a) C_D, C_L, C_m vs β.

Figure 30.– Concluded. (b) C_Y, C_l, C_n vs β.

Figure 31.– Aerodynamic characteristics in sideslip of the missile at several angles of attack with deflection target posts on the left wing panel. δ_e, 0°; R, 12.5×10^6. (a) C_D, C_L, C_m vs β.

Figure 31.– Concluded. (b) C_Y, C_l, C_n vs β.

Figure 32.– Aerodynamic characteristics in sideslip of the missile at several angles of attack with deflection target posts on the left wing panel. δ_e, -10°; R, 11×10^6. (a) C_D, C_L, C_m vs β.

Figure 32.– Concluded. (b) C_Y, C_l, C_n vs β.

Figure 33.– Aerodynamic characteristics in sideslip of the missile at several angles of attack with deflection target posts on the left wing panel. δ_e, -10°; R, 12.5×10^6. (a) C_D, C_L, C_m vs β.

Figure 33.– Concluded. (b) C_Y, C_l, C_n vs β.

Figure 34.– Aerodynamic characteristics in sideslip of the missile at several angles of attack with deflection target posts on the left wing panel. δ_r, 0°; δ_l, -10°; R, 11×10^6. (a) C_D, C_L, C_m vs β.

Figure 34.– Concluded. (b) C_Y, C_l, C_n vs β.

Figure 35.– Aerodynamic characteristics in sideslip of the missile at several angles of attack with deflection target posts on the left wing panel. δ_r, 0°; δ_l, 15°; R, 11×10^6. (a) C_D, C_L, C_m vs β.

Figure 35.– Concluded. (b) C_Y, C_l, C_n vs β.

Figure 36.– Comparison of the aerodynamic characteristics in pitch of the missile with duct open and closed. β, 0°; δ_e, 0°; R, 9×10^6.

Figure 37.– Effect of the landing skids on the aerodynamic characteristics of the missile in pitch. β, 0°; δ_e, -10°; R, 13.4×10^6.

Figure 38.– Comparison of the aerodynamic characteristics in sideslip of the complete missile with the characteristics of the missile with the vertical tail removed, and with the fuselage alone. R, 11×10^6; δ_e, 0°; α, 0°. (a) C_D, C_L, C_m vs β.

Figure 38.– Concluded. (b) C_Y, C_l, C_n vs β.

Figure 39.– Comparison of the aerodynamic characteristics in sideslip of the complete missile with the characteristics of the missile with the vertical tail removed, and with the fuselage alone. R, 11×10^6; δ_e, 0°; α, 3°. (a) C_D, C_L, C_m vs β.

Figure 39.– Concluded. (b) C_Y, C_l, C_n vs β.

Figure 40.– Comparison of the aerodynamic characteristics in sideslip of the complete missile with the characteristics of the missile with the vertical tail removed, and with the fuselage alone. R, 11×10^6; δ_e, 0°; α, 7°. (a) C_D, C_L, C_m vs β.

Figure 40.– Concluded. (b) C_Y, C_l, C_n vs β.

Figure 41.- Comparison of the aerodynamic characteristics in sideslip of the complete missile with the characteristics of the missile with the vertical tail removed, and with the fuselage alone. R, 11×10^6; δ_e, 0°; α, 10°. (a) C_D, C_L, C_m vs β.

Figure 41.- Concluded. (b) C_Y, C_l, C_n vs β.

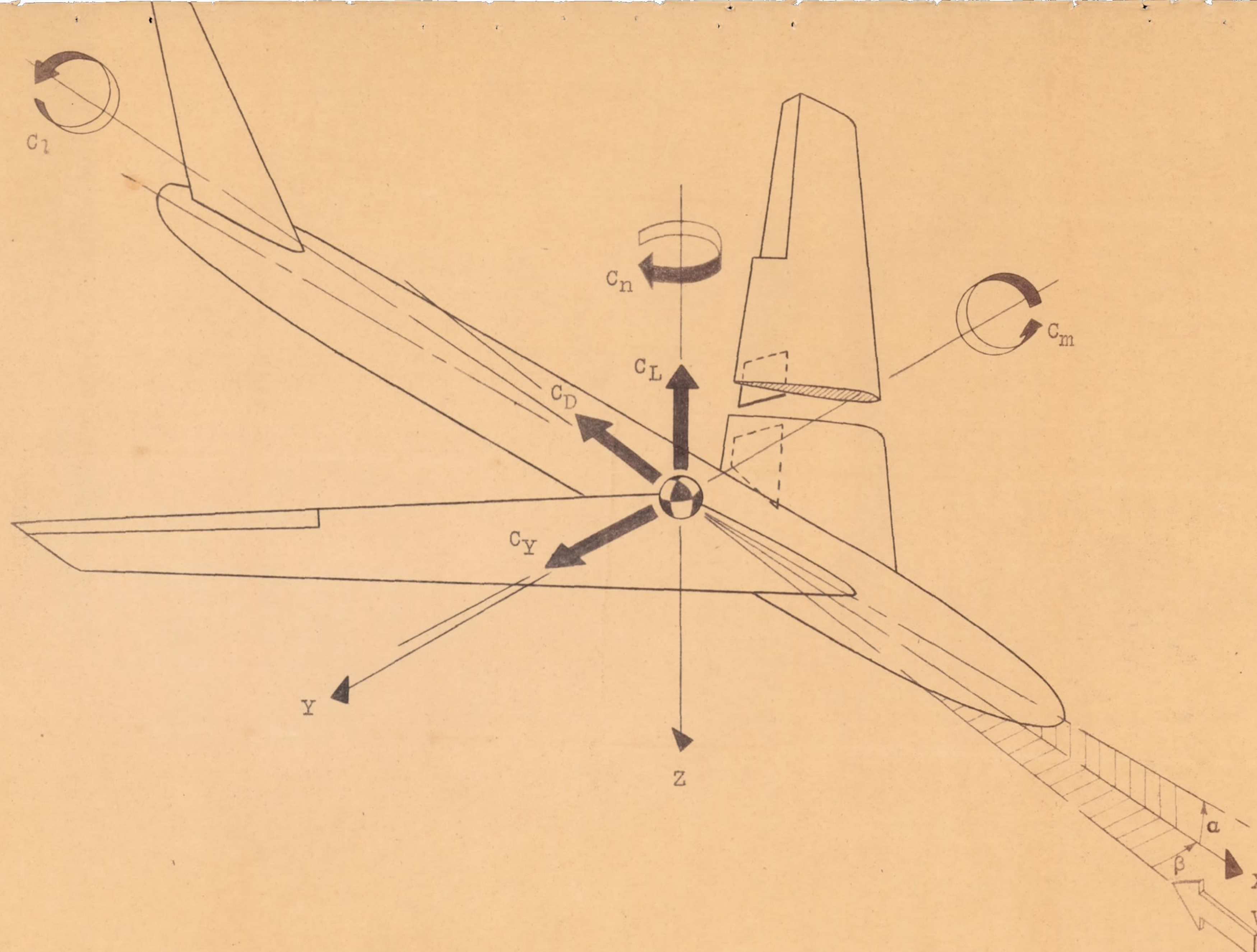

Figure 1.- Sign convention for the standard NACA coefficients. The forces, moments, angles, and control-surface deflections are shown as positive.

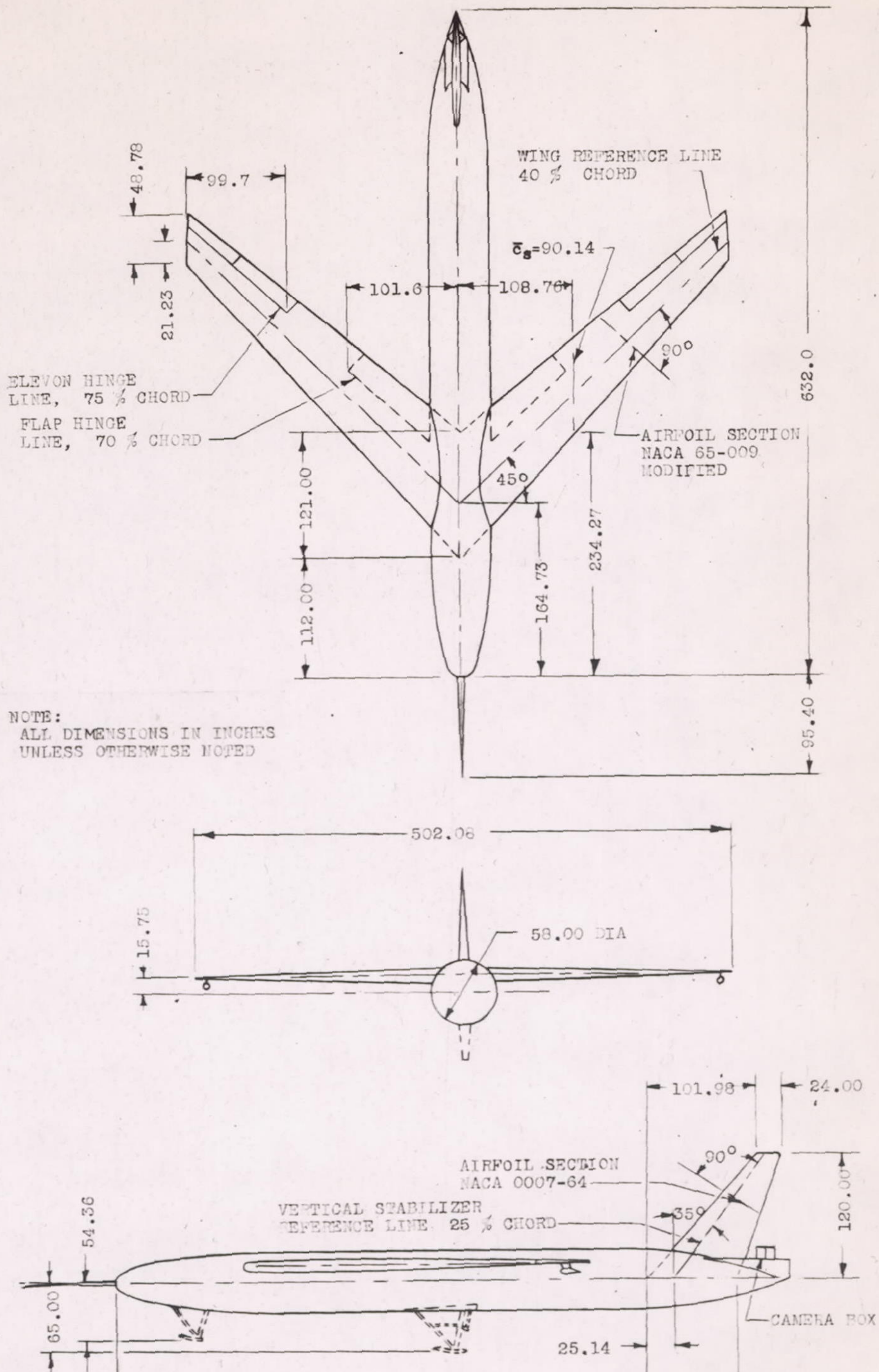

FIGURE 2.- THREE-VIEW DRAWING OF THE NORTHROP XSSM-A-3 MISSILE.

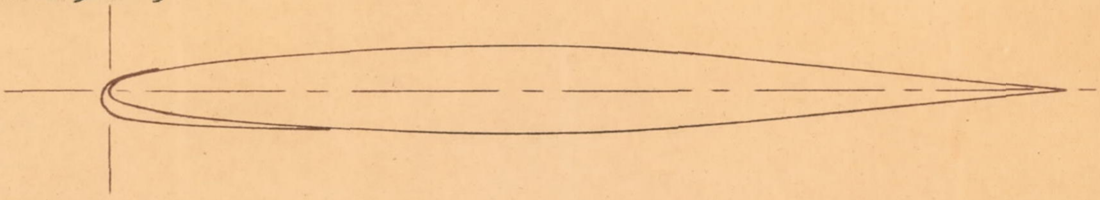

COORDINATES

ORIGINAL SECTION

Station (Percent of chord)	Ordinate (Percent of chord)
0	0
.50	.700
.75	.845
1.25	1.058
2.50	1.421
5.00	1.961
7.50	2.383
10.00	2.736
15.00	3.299
20.00	3.727
25.00	4.050
30.00	4.282
35.00	4.431
40.00	4.496
45.00	4.469
50.00	4.336
55.00	4.086
60.00	3.743
65.00	3.328
66.00[a]	3.241
100.00	0
L.E. radius: .552	

[a]Section faired from 66-percent-chord point to the trailing edge by straight lines.

INCREASED LEADING-EDGE RADIUS

Station (Percent of chord)	Ordinates (Percent of chord)	
	Upper	Lower
-0.727	-0.872	-0.872
-.363	.145	-1.816
0	.465	-2.136
.363	.697	-2.339
.727	.886	-2.477
1.453	1.191	-2.674
2.180	1.387	-2.826
3.633	1.729	-3.065
5.085	2.005	-3.219
6.538		-3.305
7.991		-3.385
10.171		-3.458
12.349		-3.508
14.529		-3.537
16.708		-3.596
18.888		-3.719
21.068		-3.865
23.246		-3.981
L.E. radius: 1.60; center at station .872; ordinate -.872		

Figure 3.- Profile and coordinates of the NACA 65-009 (mod.) airfoil section with increased nose radius.

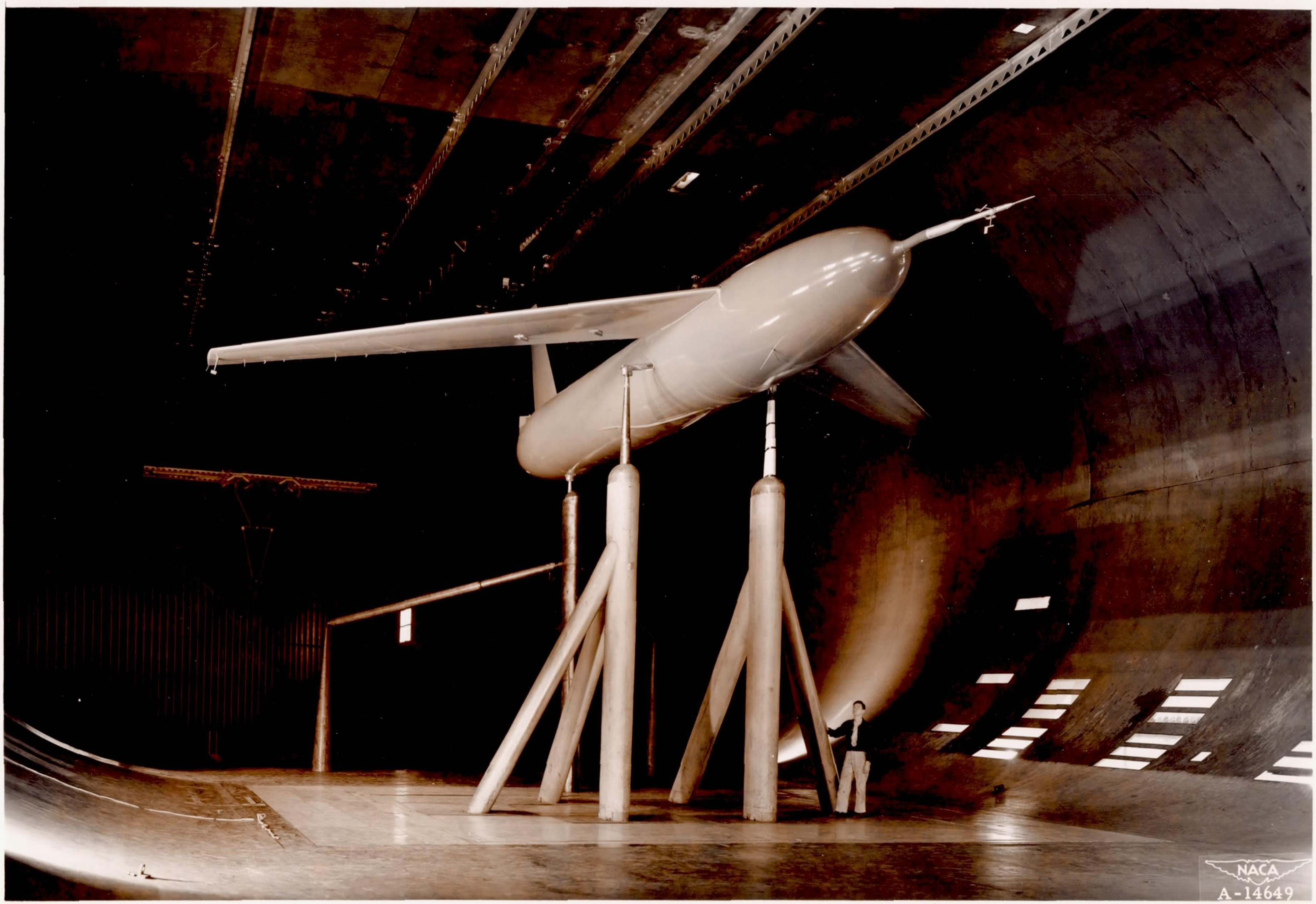

(a) Front view of the missile.

Figure 4.- Views of the Northrop XSSM-A-3 missile as installed in the Ames 40- by 80-foot wind tunnel.

(b) Rear view of the missile.

Figure 4.- Continued.

(c) Close-up of the lower surface of the right wing showing the trailing-edge split flaps deflected 45°.

Figure 4.- Continued.

(d) View showing the deflection target posts on the left wing panel and the camera position on the missile.

Figure 4.- Continued.

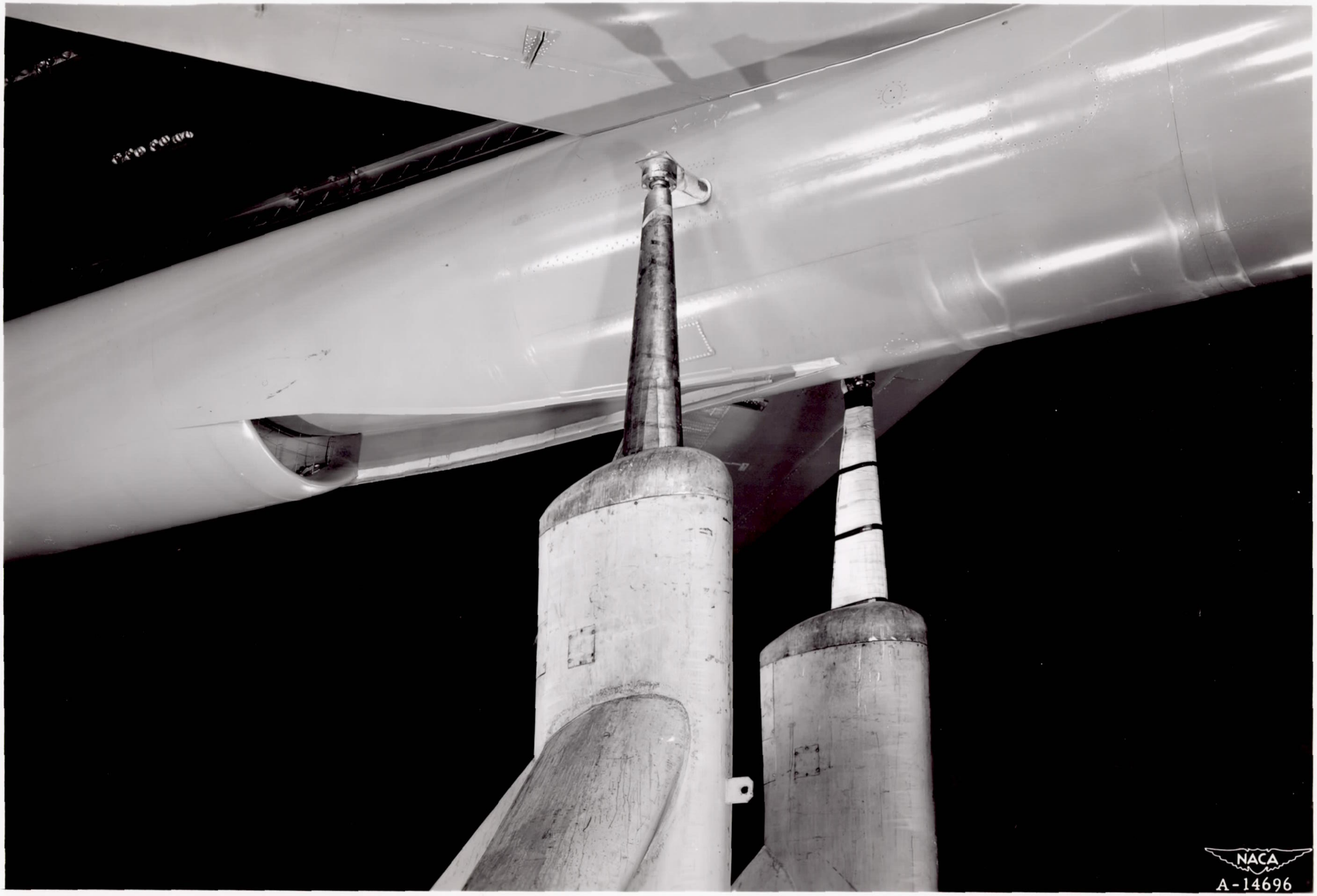

(e) Close-up of the fuselage with the duct inlet open.

Figure 4.- Continued.

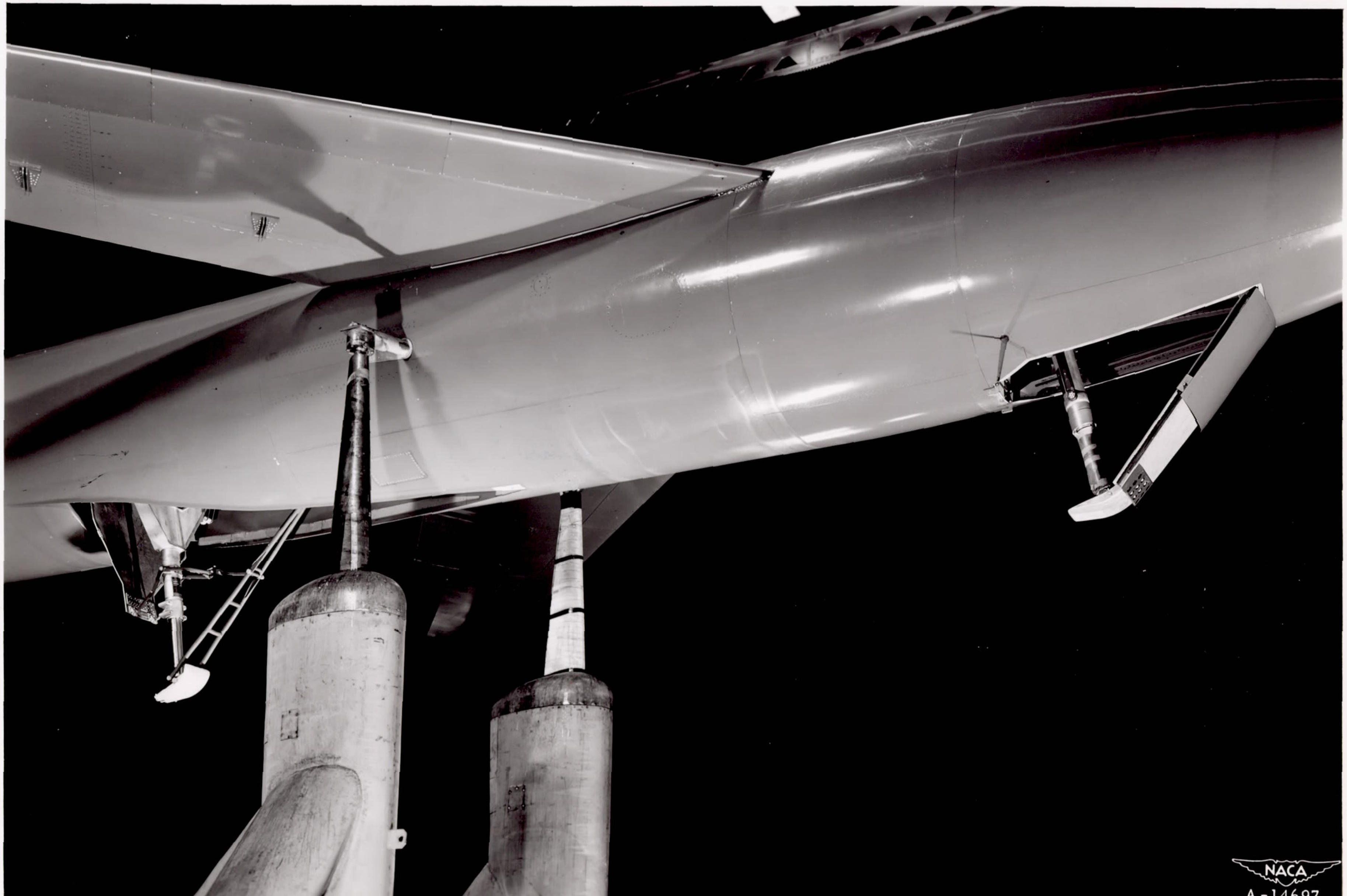

(f) Side view showing the landing skids extended.

Figure 4.- Continued.

(g) Front view of the fuselage alone.

Figure 4.- Continued.

(h) Rear view of the missile with the vertical tail removed.

Figure 4.- Continued.

(i) Close-up of the lower surface of the left wing showing the slab-sided elevons.

Figure 4.- Concluded.

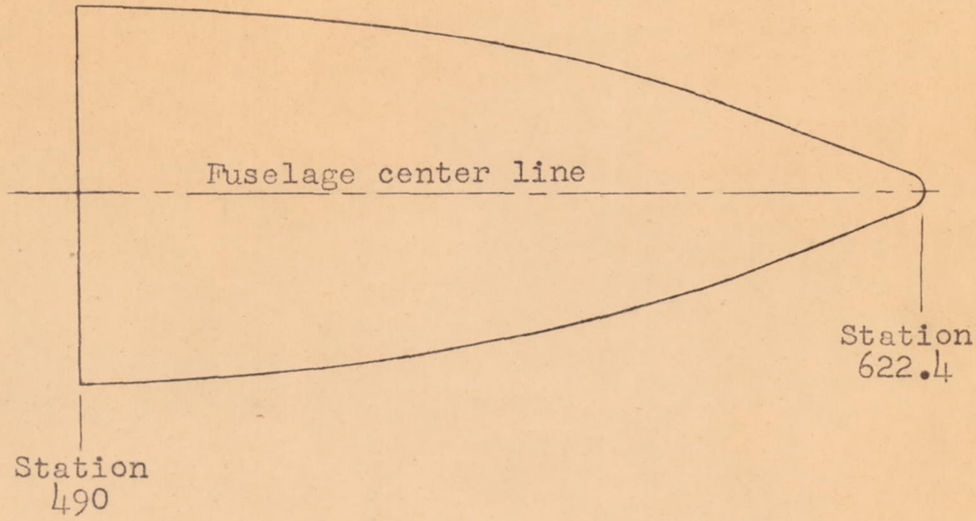

[a] Station (in.)	Radius (in.)
490	29.0
500	28.9
510	28.5
520	27.8
530	26.8
540	25.6
550	24.1
560	22.2
570	20.0
580	17.3
590	14.1
600	10.5
610	6.9
620	3.2

[a]Stations are measured from nose of fuselage

Figure 5.- Details of the faired tail cone.

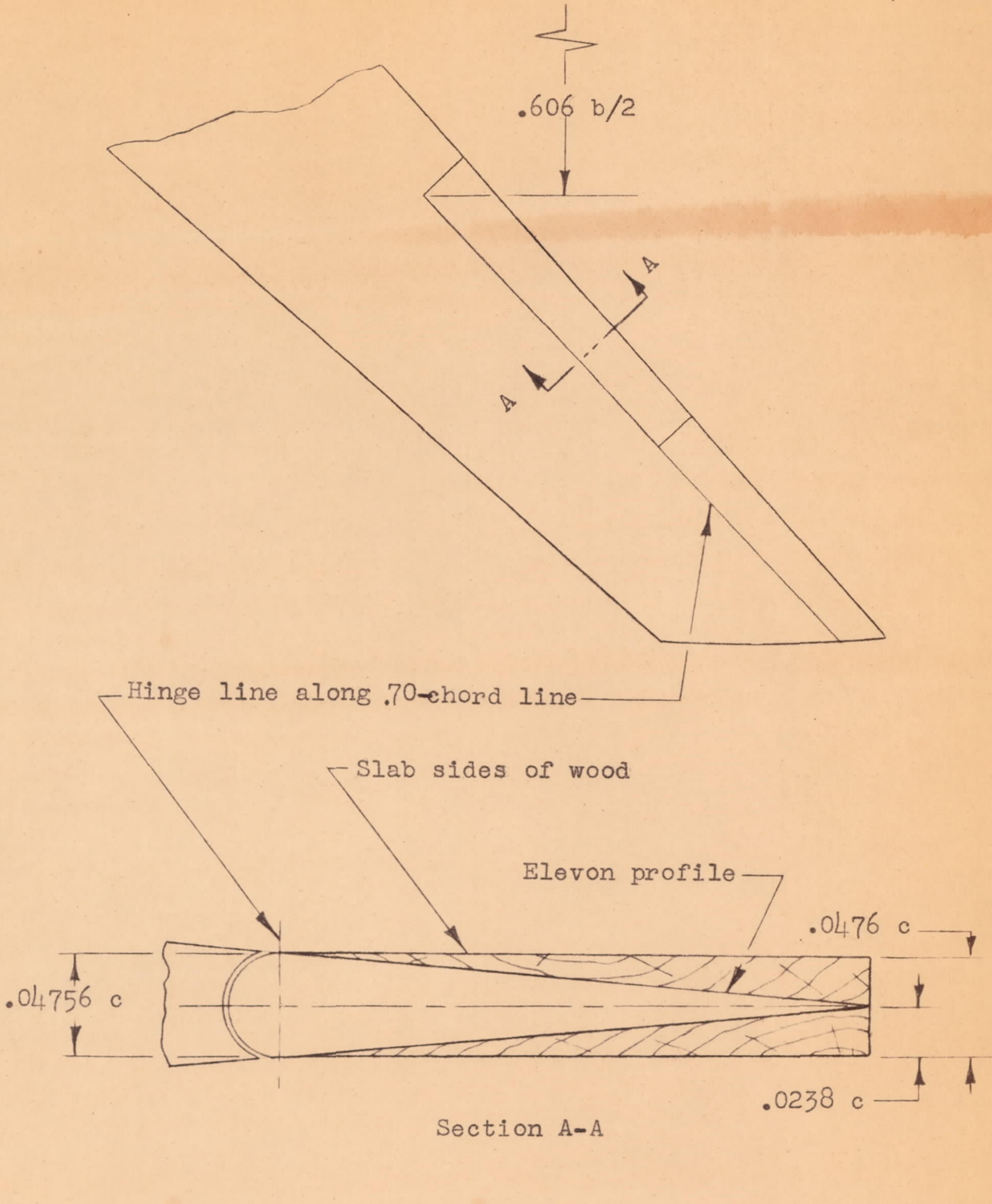

Figure 6.- Details of the slab-sided elevons.

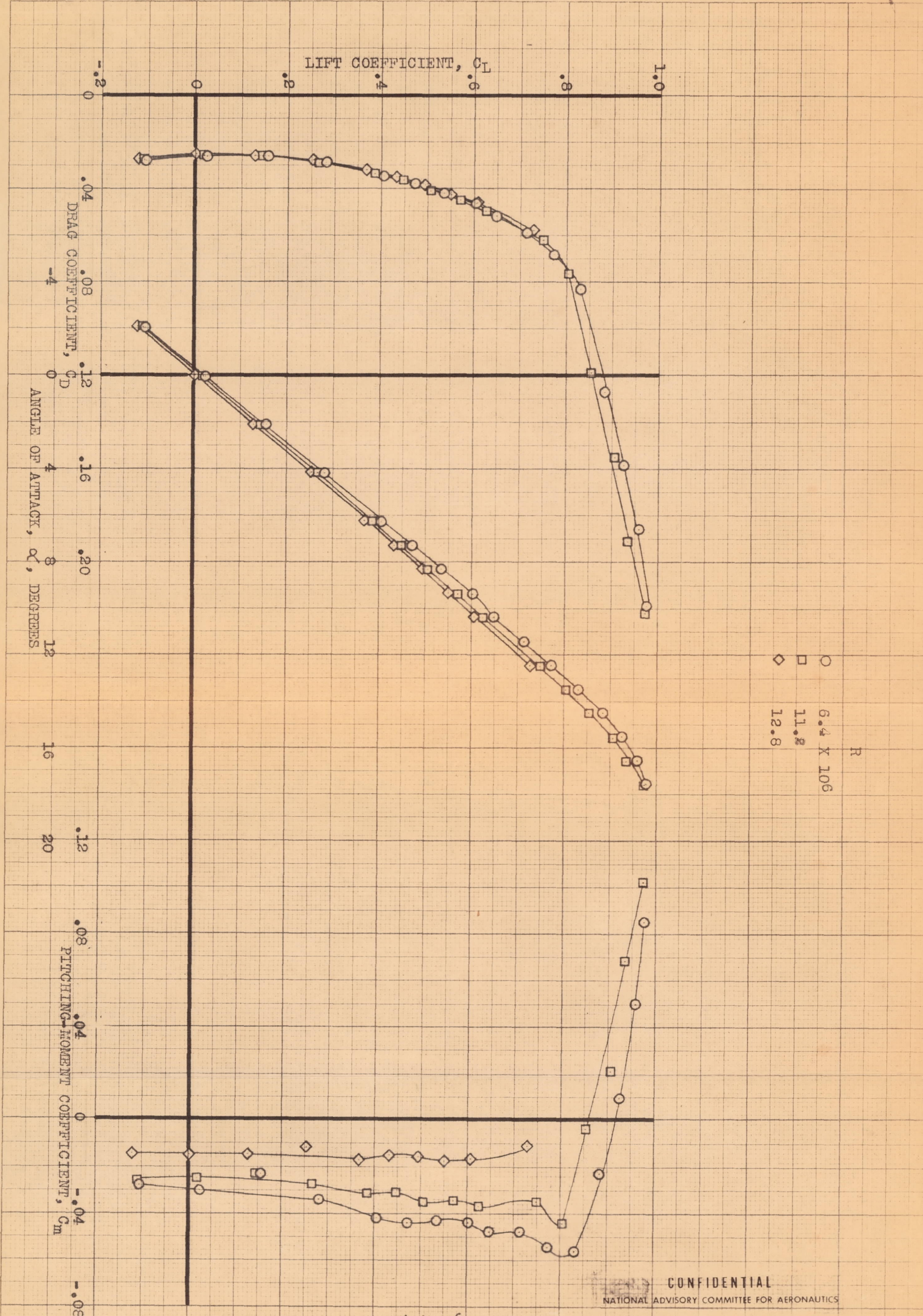

(a) δ_e, 5°.

FIGURE 7.- AERODYNAMIC CHARACTERISTICS IN PITCH OF THE MISSILE WITH VARIOUS FIXED ELEVON DEFLECTIONS AND AT VARIOUS REYNOLDS NUMBERS. β, 0°.

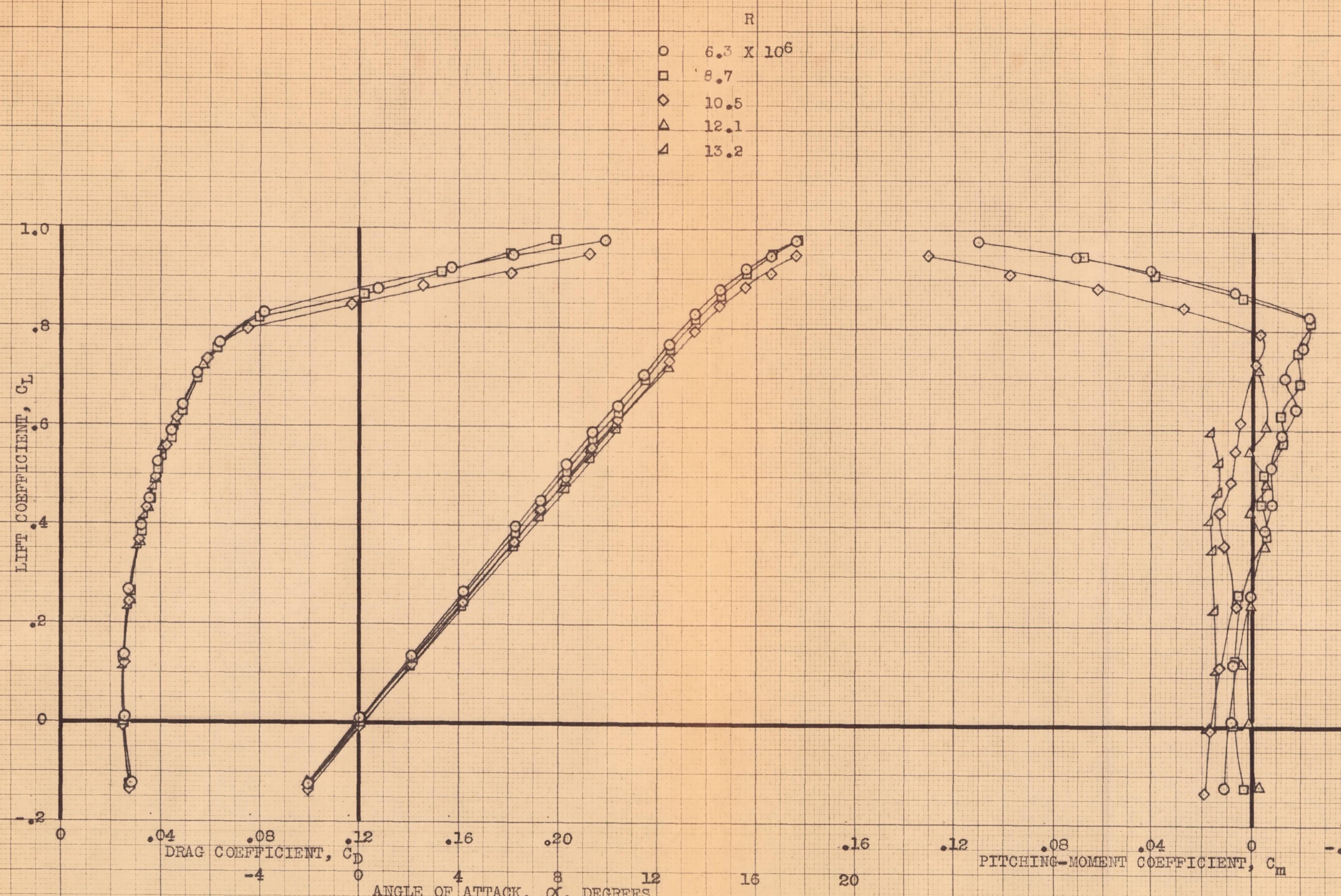

(b) δ_e, 0°.

FIGURE 7.- CONTINUED.

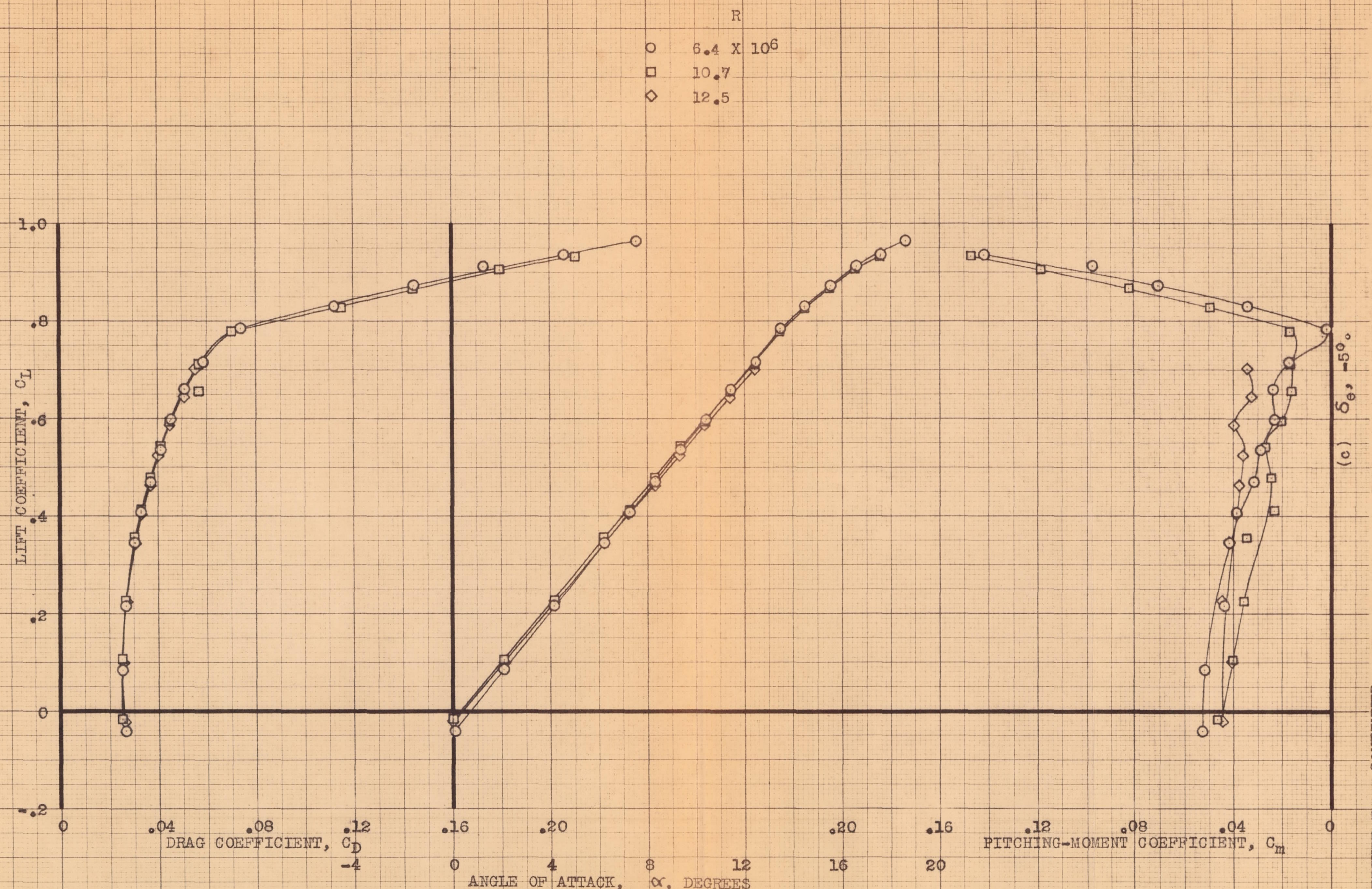

FIGURE 7.- CONTINUED.

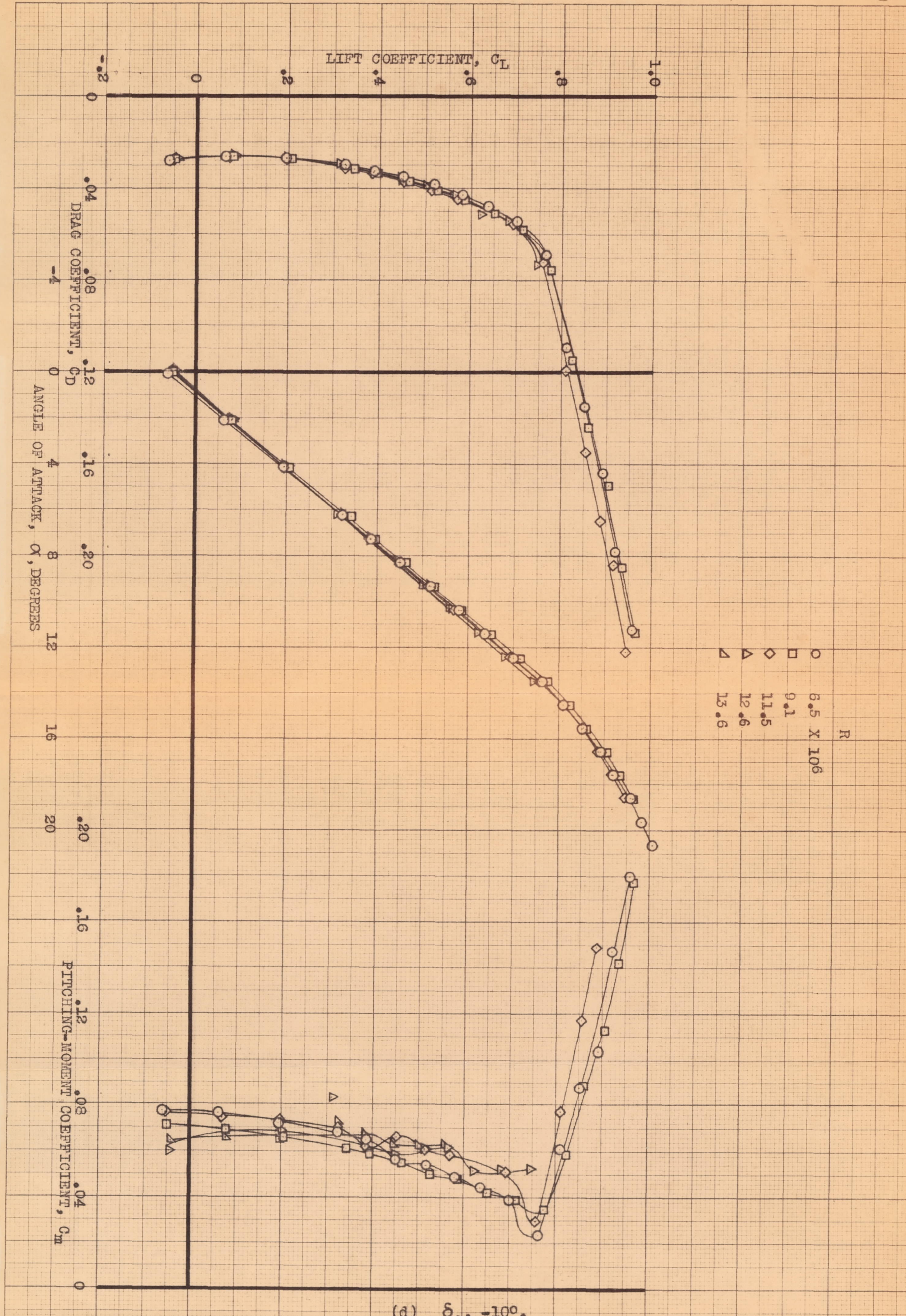

(d) δ_e, $-10°$.

FIGURE 7.- CONTINUED.

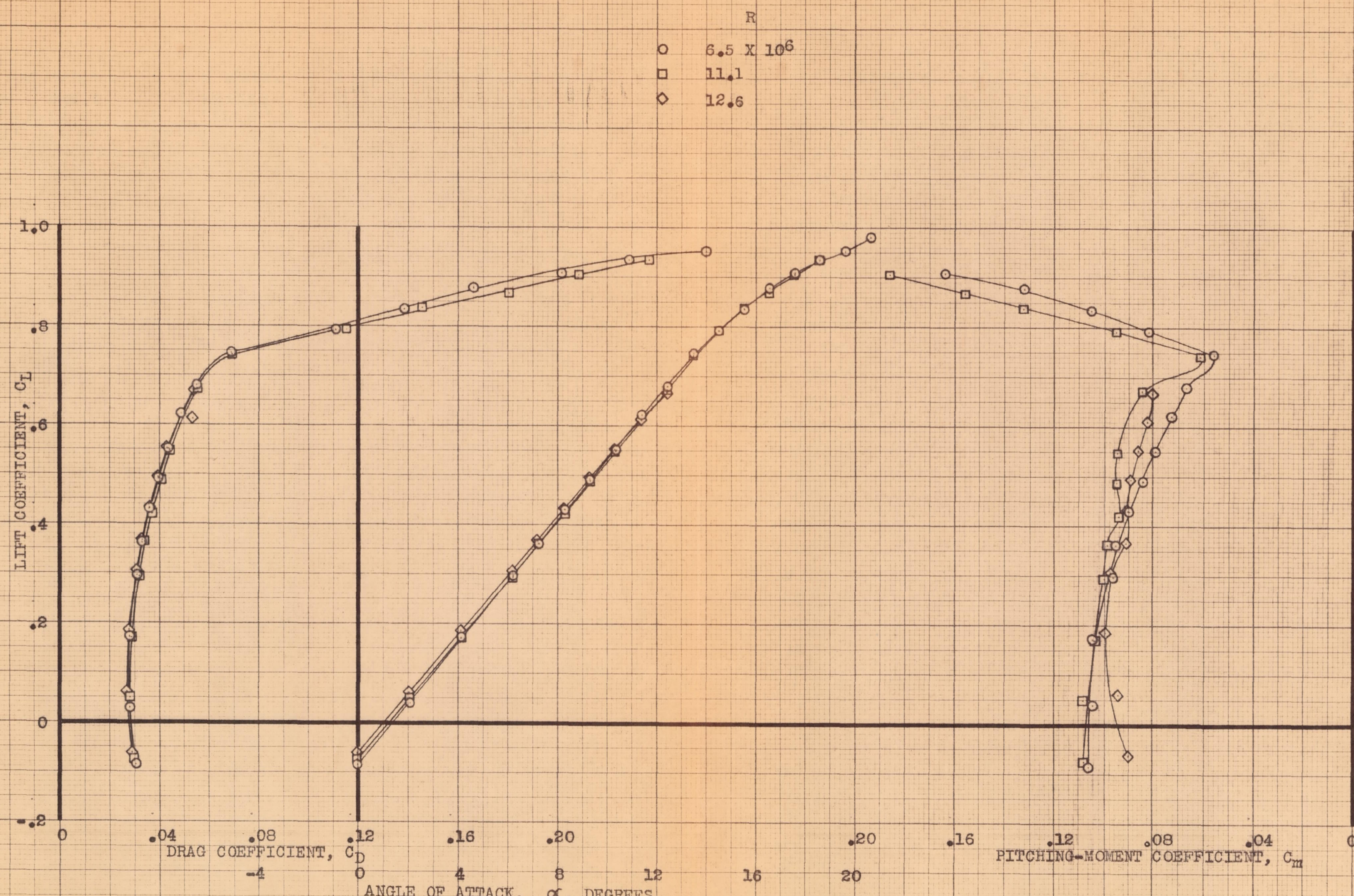

(e) δ_e, -15°.

FIGURE 7.- CONTINUED.

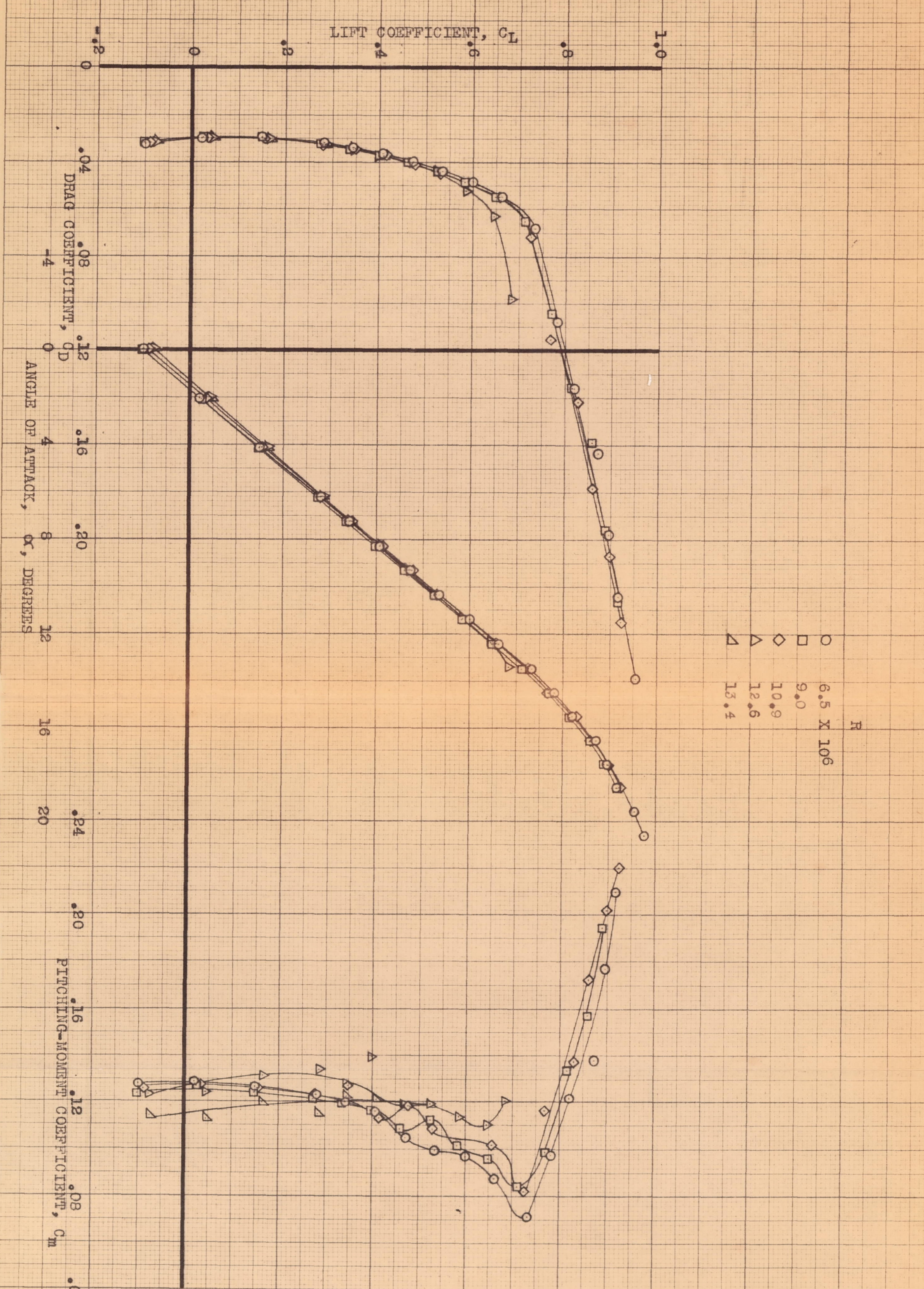

(f) δ_e, -18° (approx.).

FIGURE 7.- CONCLUDED.

NATIONAL ADVISORY COMMITTEE FOR AERONAUTICS

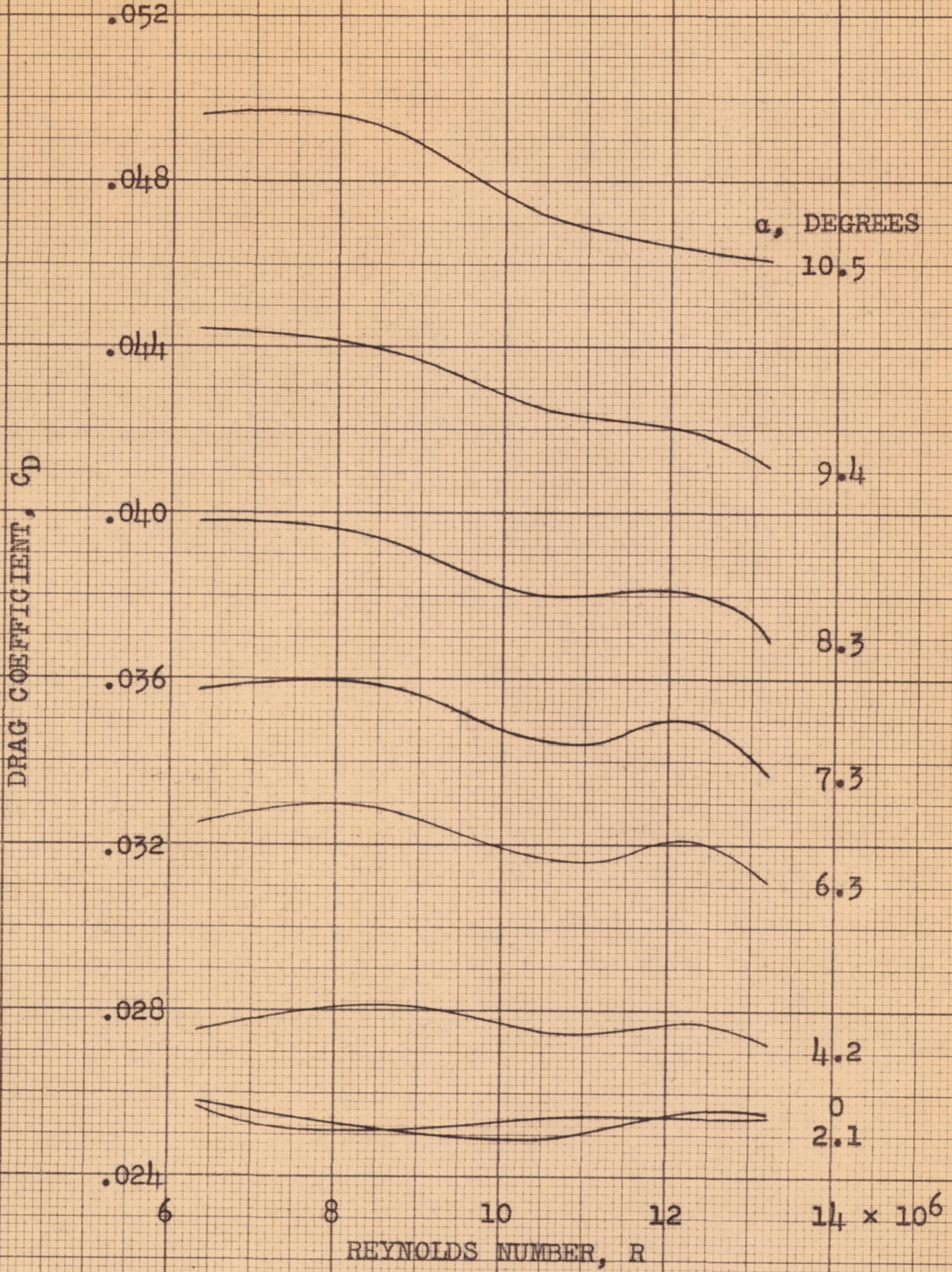

(a) δ_e, 0°.

FIGURE 8.- REYNOLDS NUMBER EFFECT ON THE DRAG COEFFICIENT OF THE MISSILE AT SEVERAL ANGLES OF ATTACK. β, 0°.

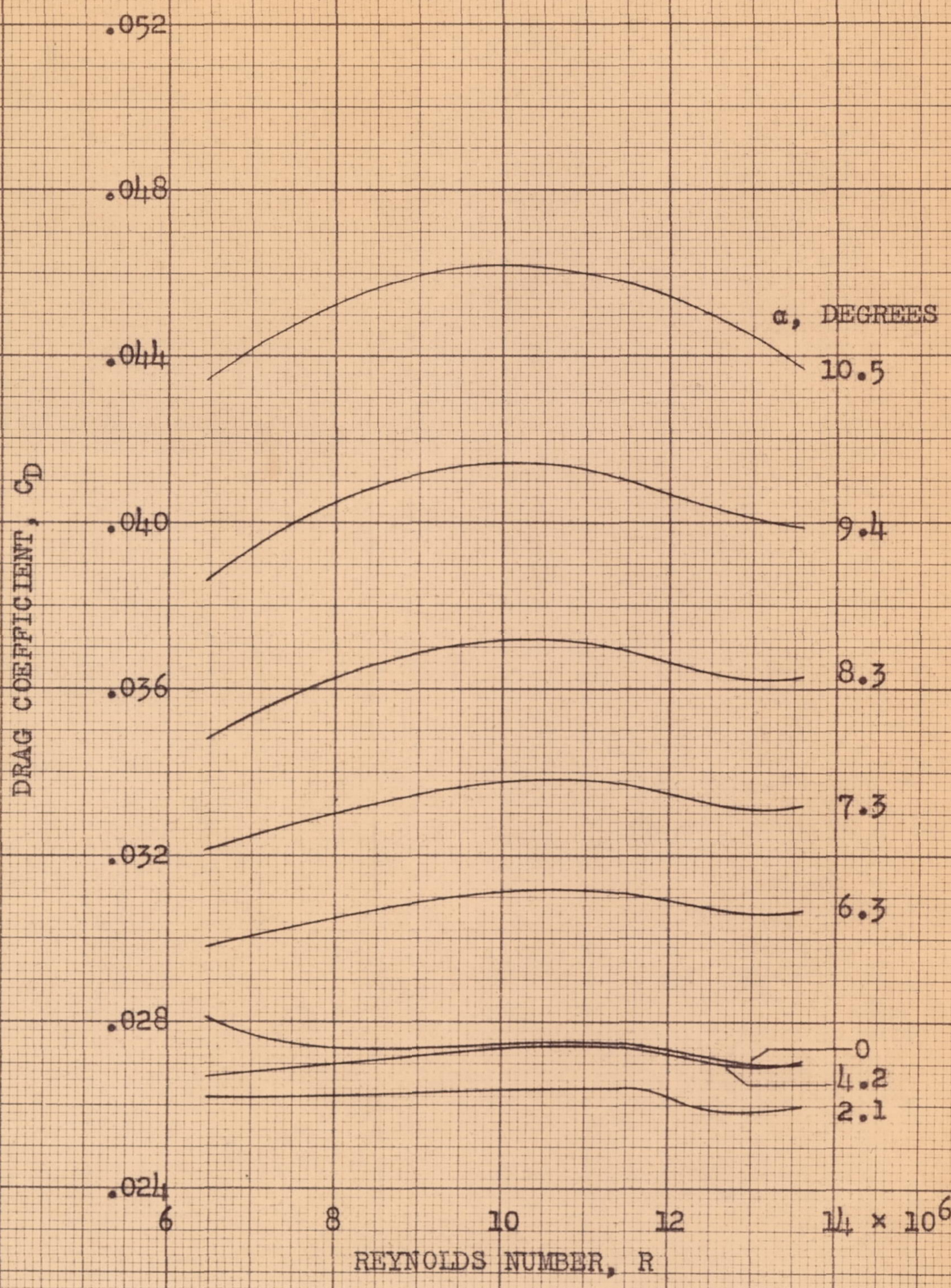

(b) δ_e, -10°.

FIGURE 8.- CONTINUED.

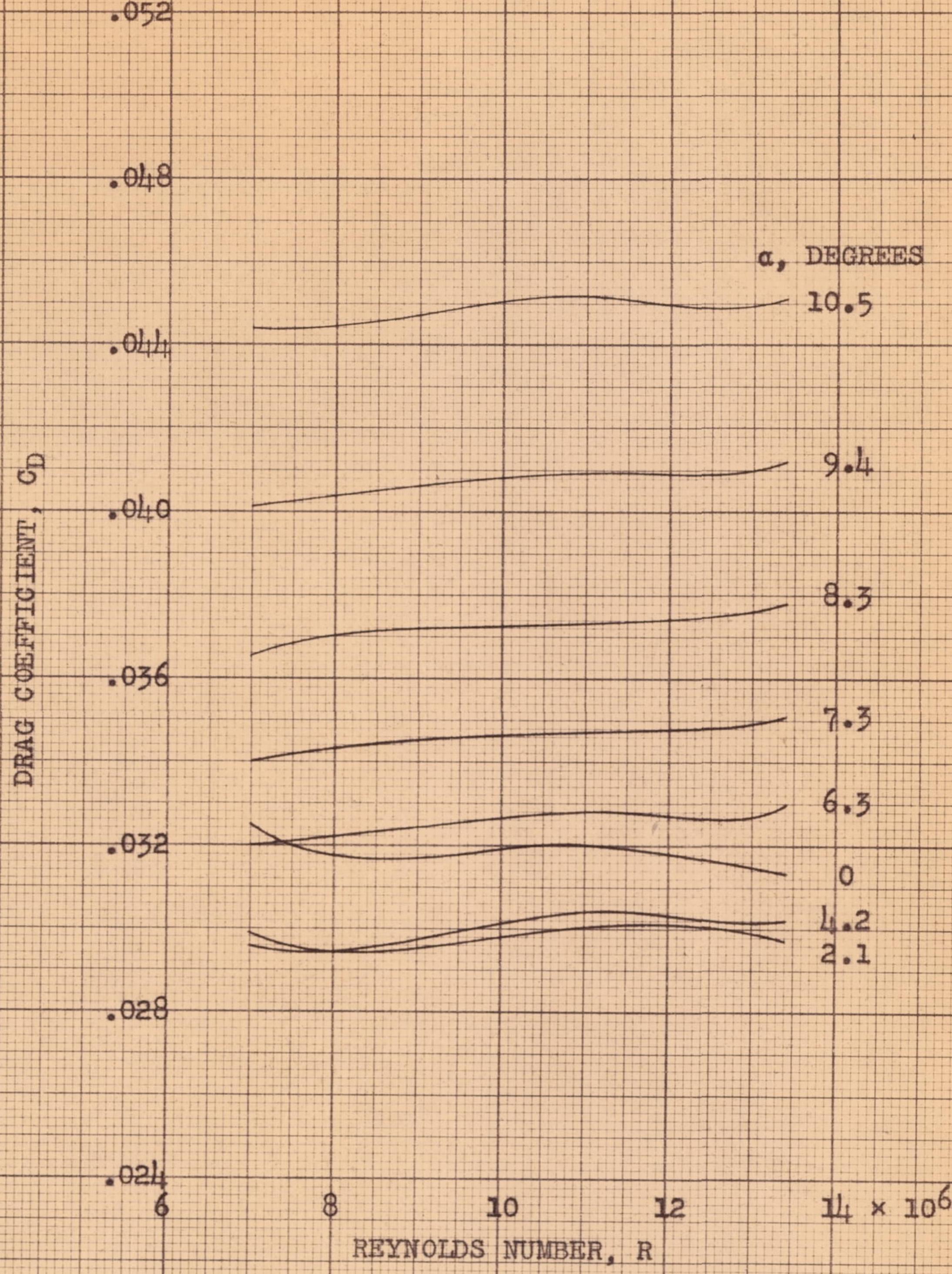

(c) δ_e, -18° (approx.).

FIGURE 8.- CONCLUDED.

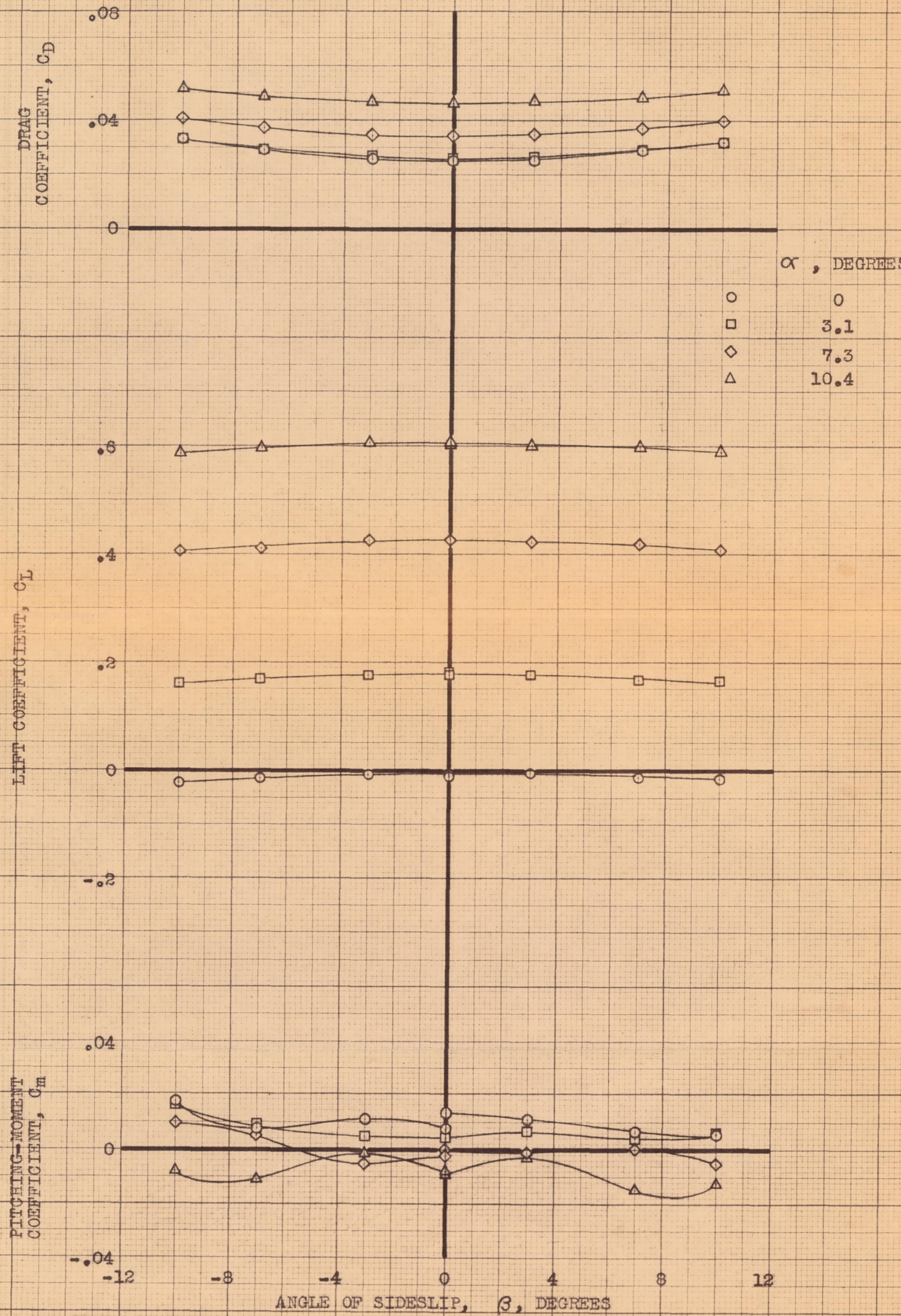

(a) C_D, C_L, C_m vs β.

FIGURE 9.- AERODYNAMIC CHARACTERISTICS IN SIDESLIP OF THE MISSILE AT SEVERAL ANGLES OF ATTACK. R, 11 X 10^6; δ_e, 0°.

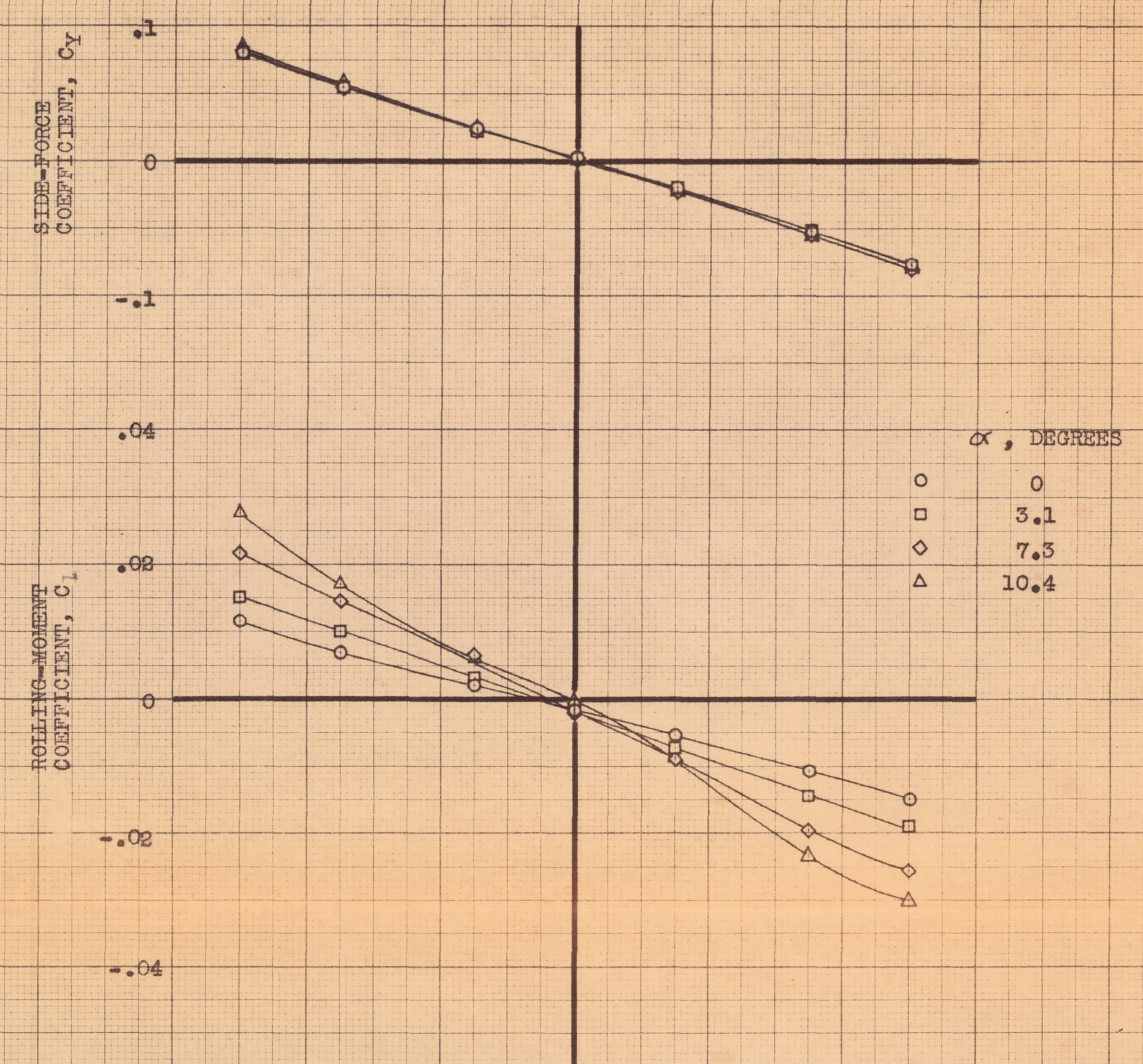

(b) C_Y, C_l, C_n vs β.

FIGURE 9.- CONCLUDED.

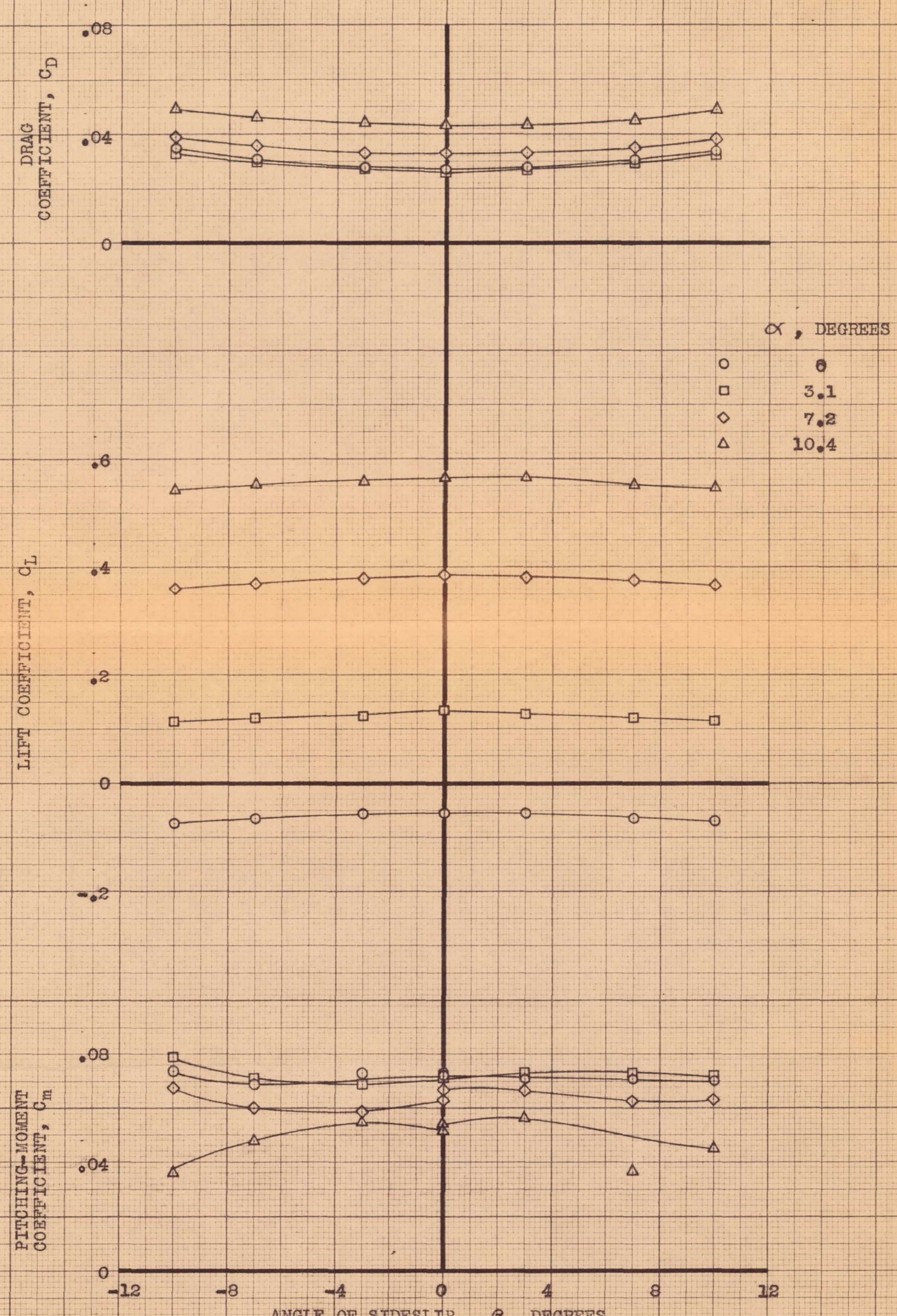

(a) C_D, C_L, C_m vs β.

FIGURE 10.- AERODYNAMIC CHARACTERISTICS IN SIDESLIP OF THE MISSILE AT SEVERAL ANGLES OF ATTACK. R, 11 X 10^6; δ_e, -10°.

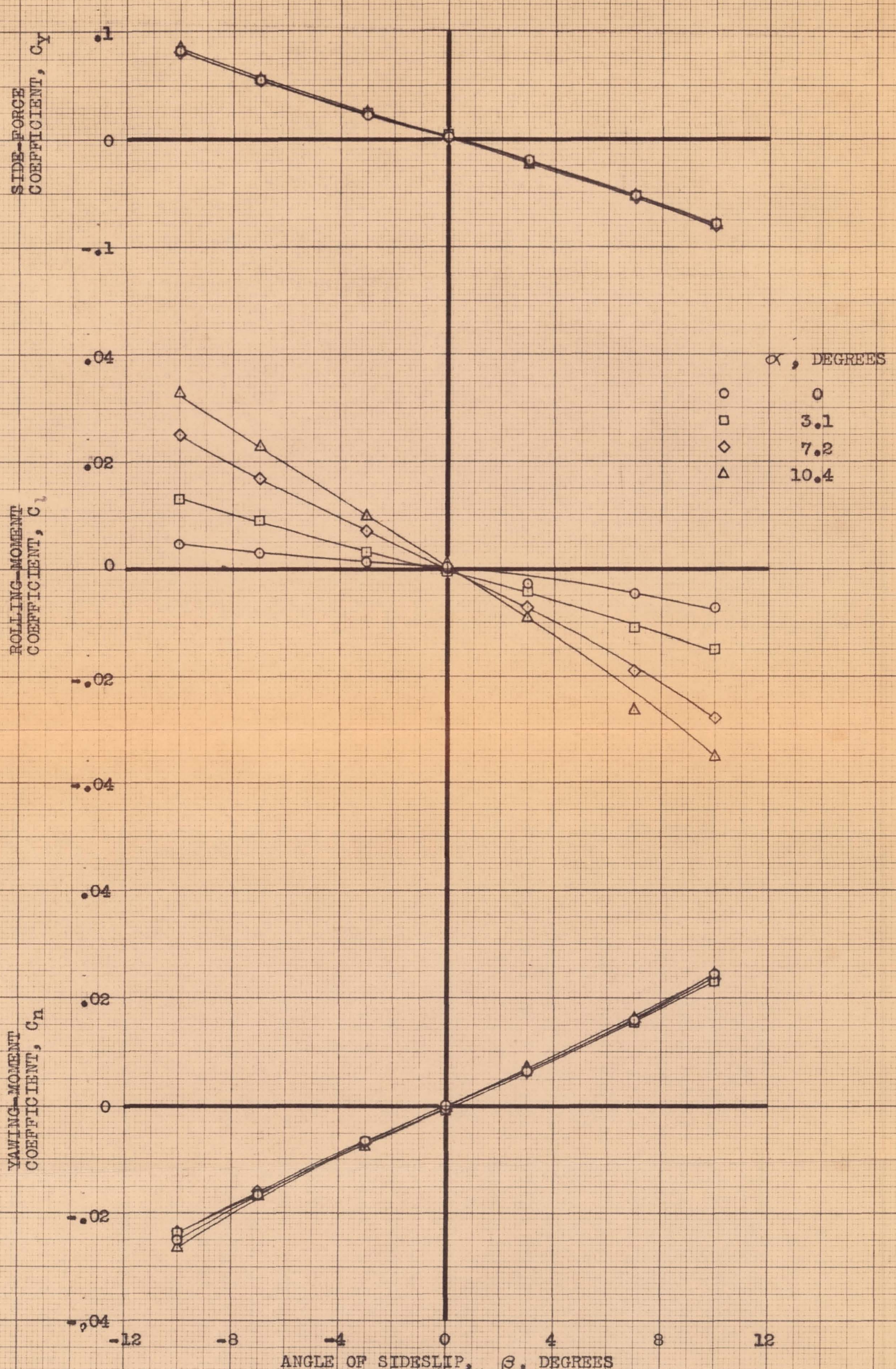

(b) C_Y, C_l, C_n vs β.

FIGURE 10.- CONCLUDED.

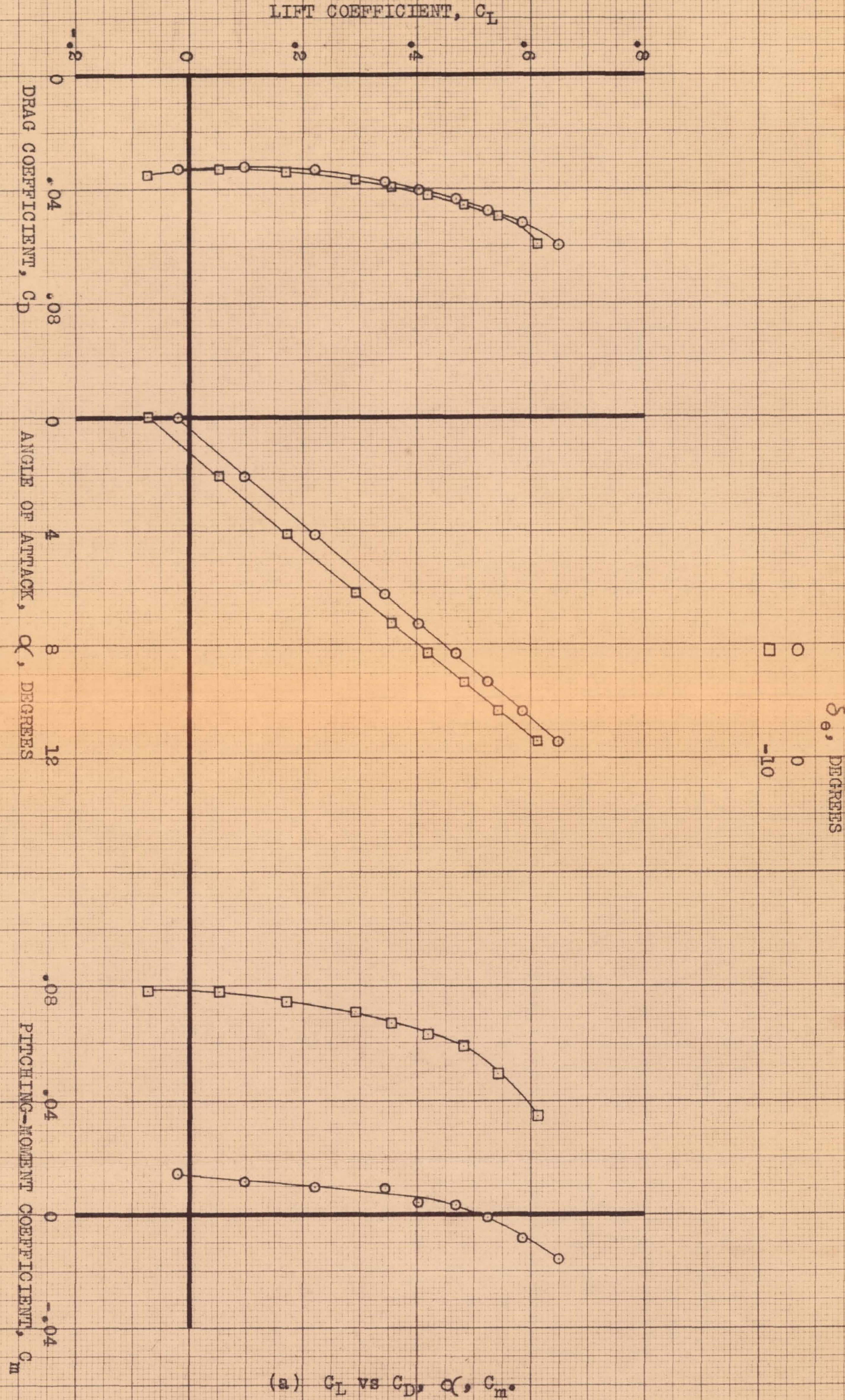

(a) C_L vs C_D, α, C_m.

FIGURE 11.- AERODYNAMIC CHARACTERISTICS IN PITCH OF THE MISSILE WITH FIXED ELEVON DEFLECTIONS. R, 11 X 10^6; β, -10°.

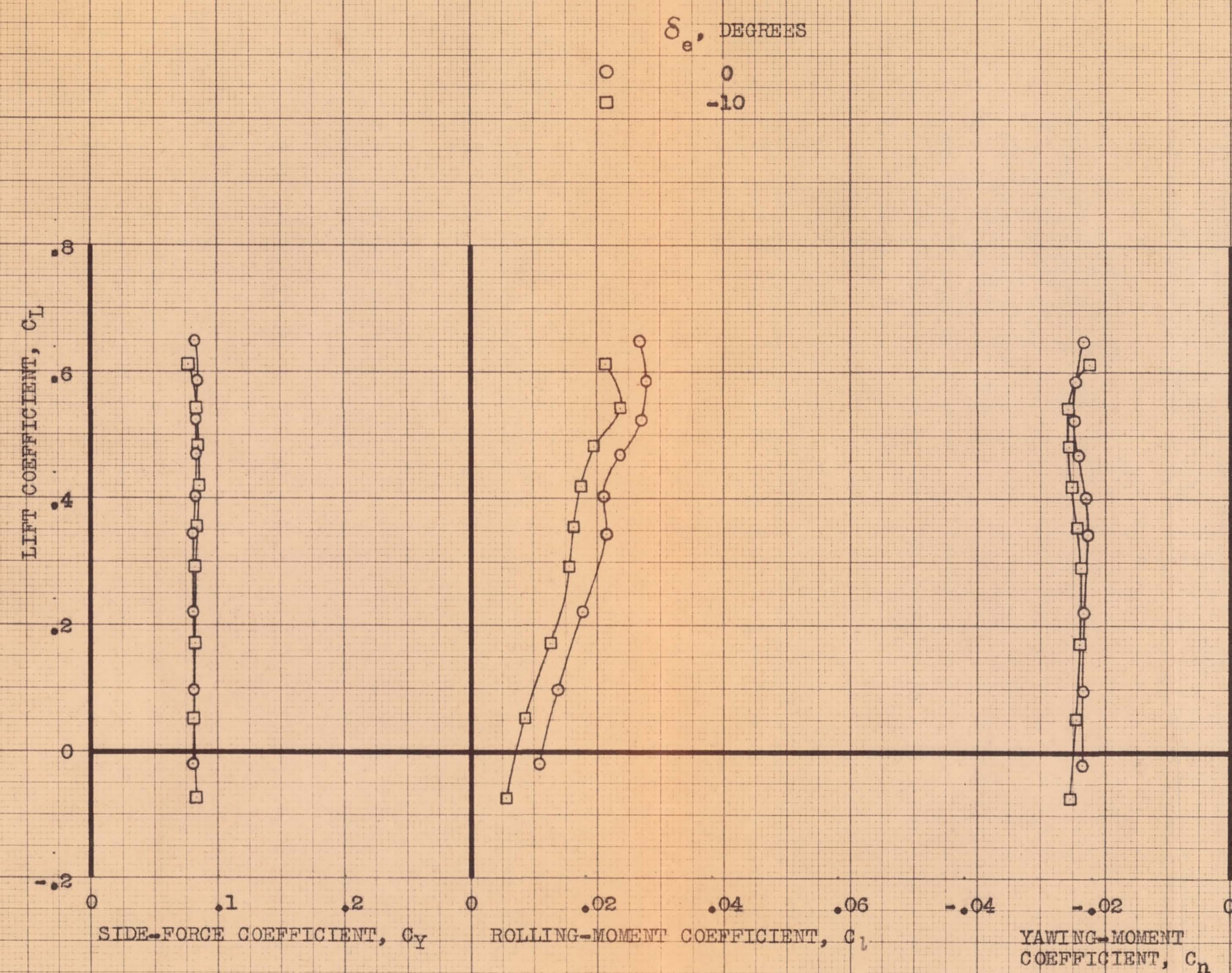

(b) C_L vs C_Y, C_l, C_n.

FIGURE 11.- CONCLUDED.

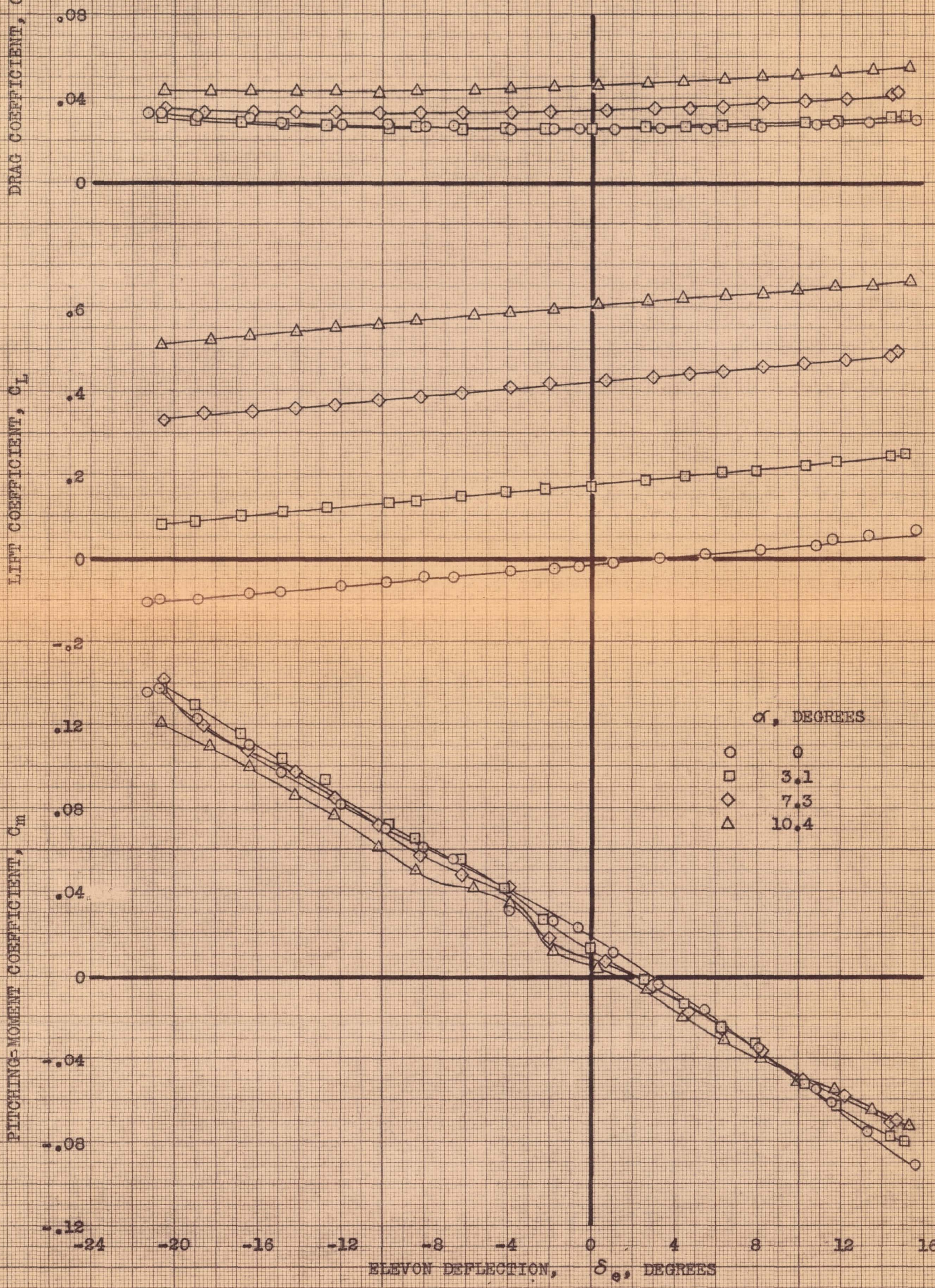

(a) R, 11×10^6.

FIGURE 12.- VARIATION, WITH ELEVON DEFLECTION, OF THE AERODYNAMIC CHARACTERISTICS OF THE MISSILE AT SEVERAL ANGLES OF ATTACK. β, 0°.

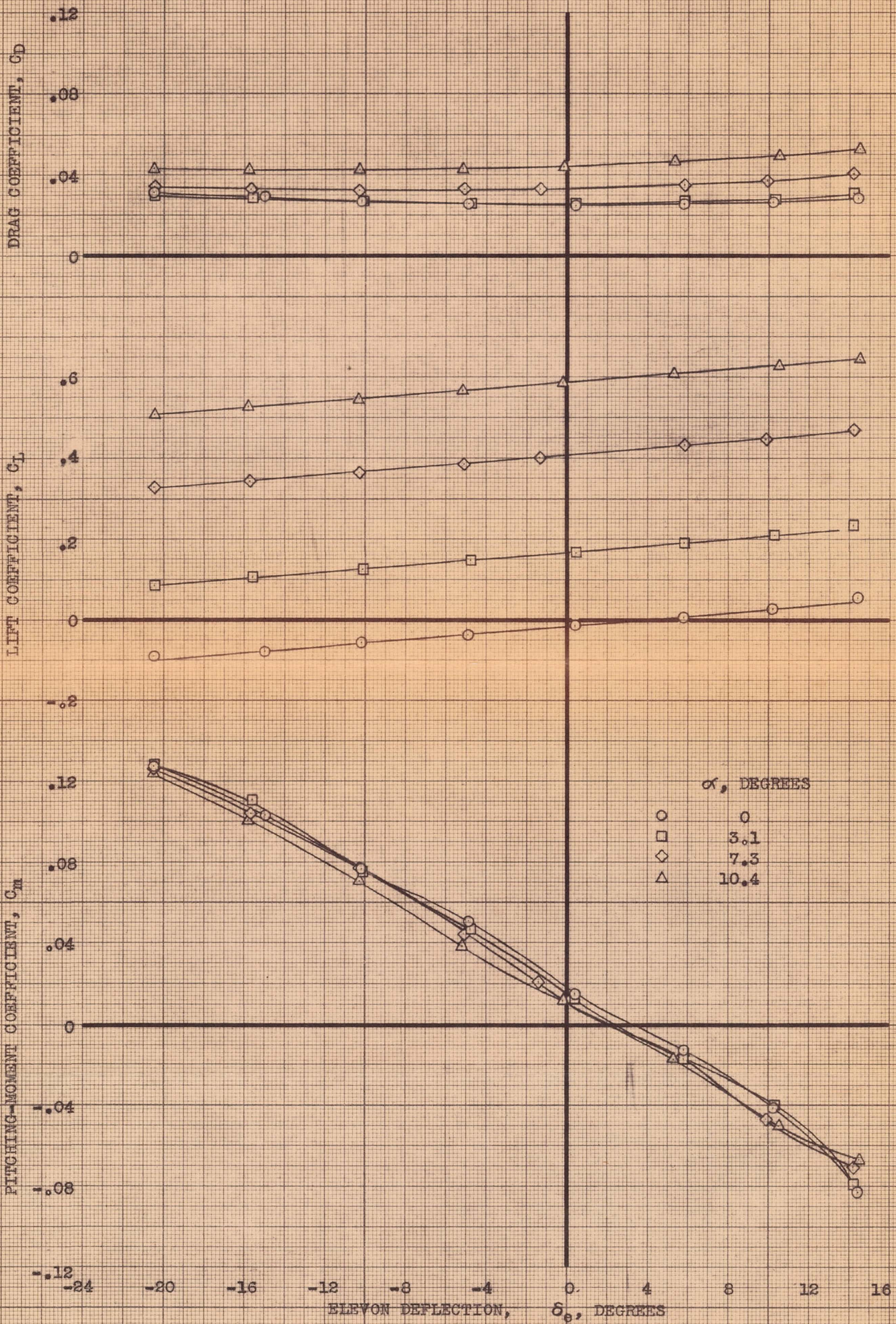

(b) R, 12.5 X 10^6.

FIGURE 12.- CONCLUDED.

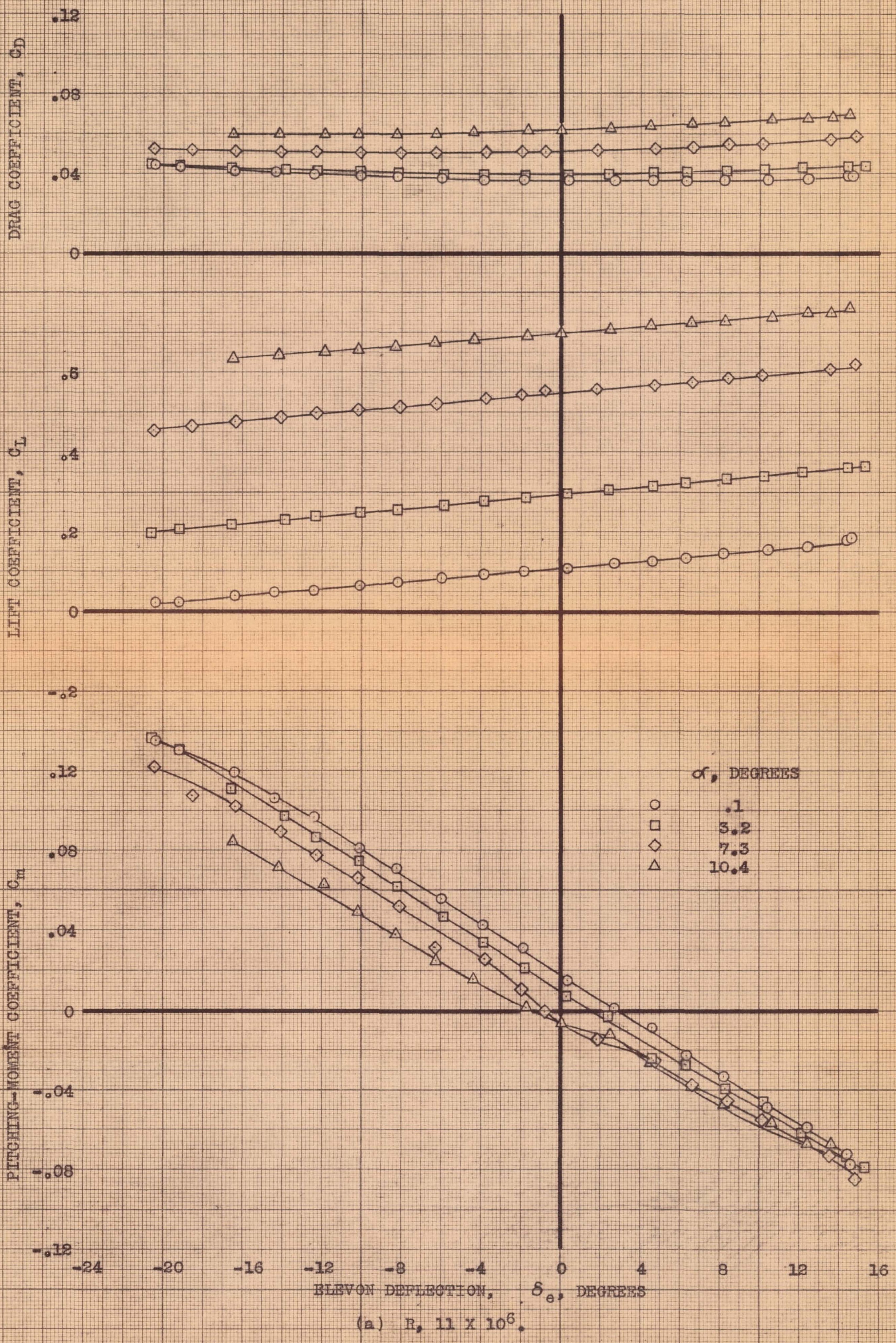

(a) R, 11 X 10[6].

FIGURE 13.- VARIATION, WITH ELEVON DEFLECTION, OF THE AERODYNAMIC CHARACTERISTICS OF THE MISSILE AT SEVERAL ANGLES OF ATTACK WITH TRAILING-EDGE FLAPS DEFLECTED 15°. β, 0°.

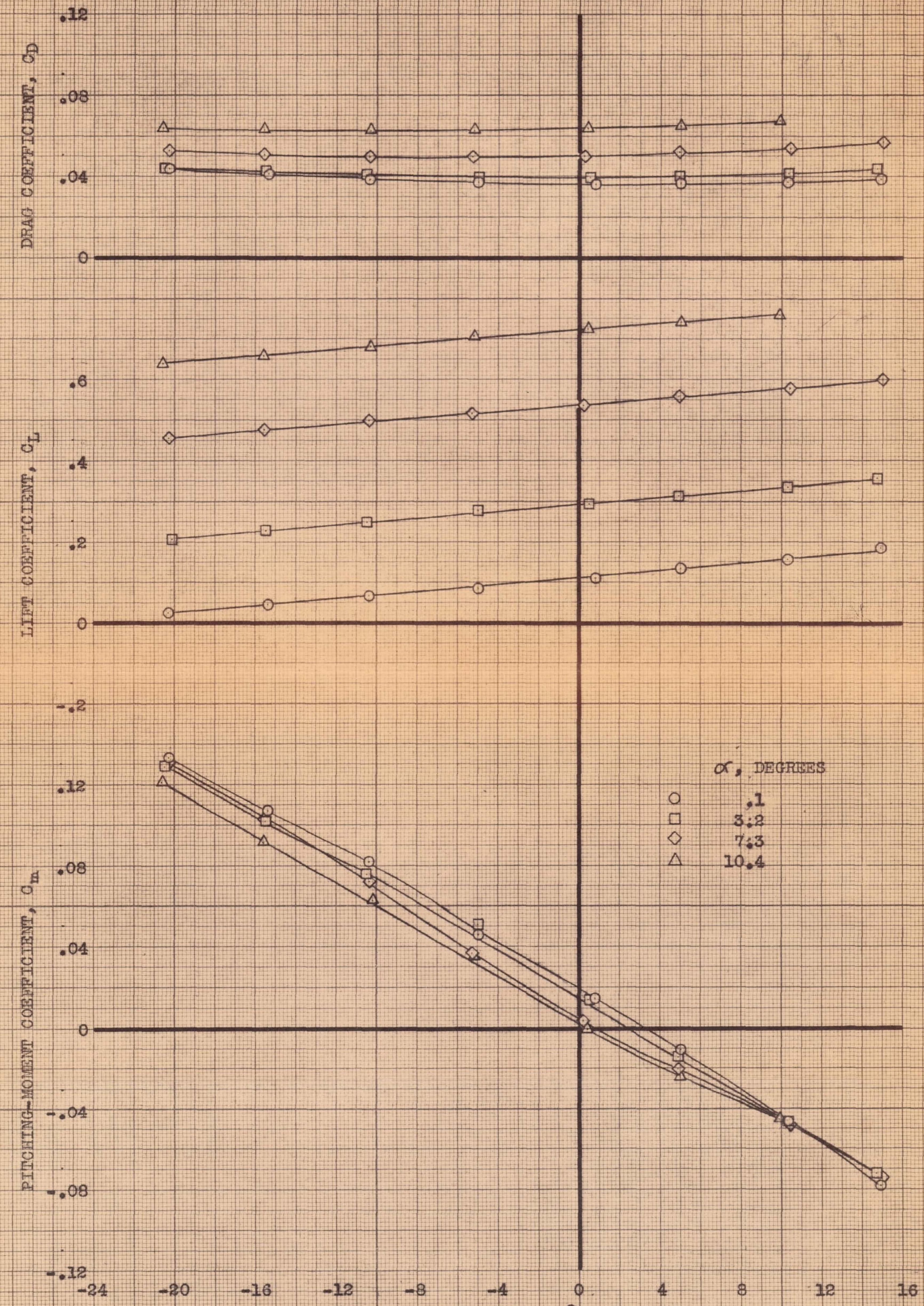

(b) R, 12 X 10^6.

FIGURE 13.- CONCLUDED.

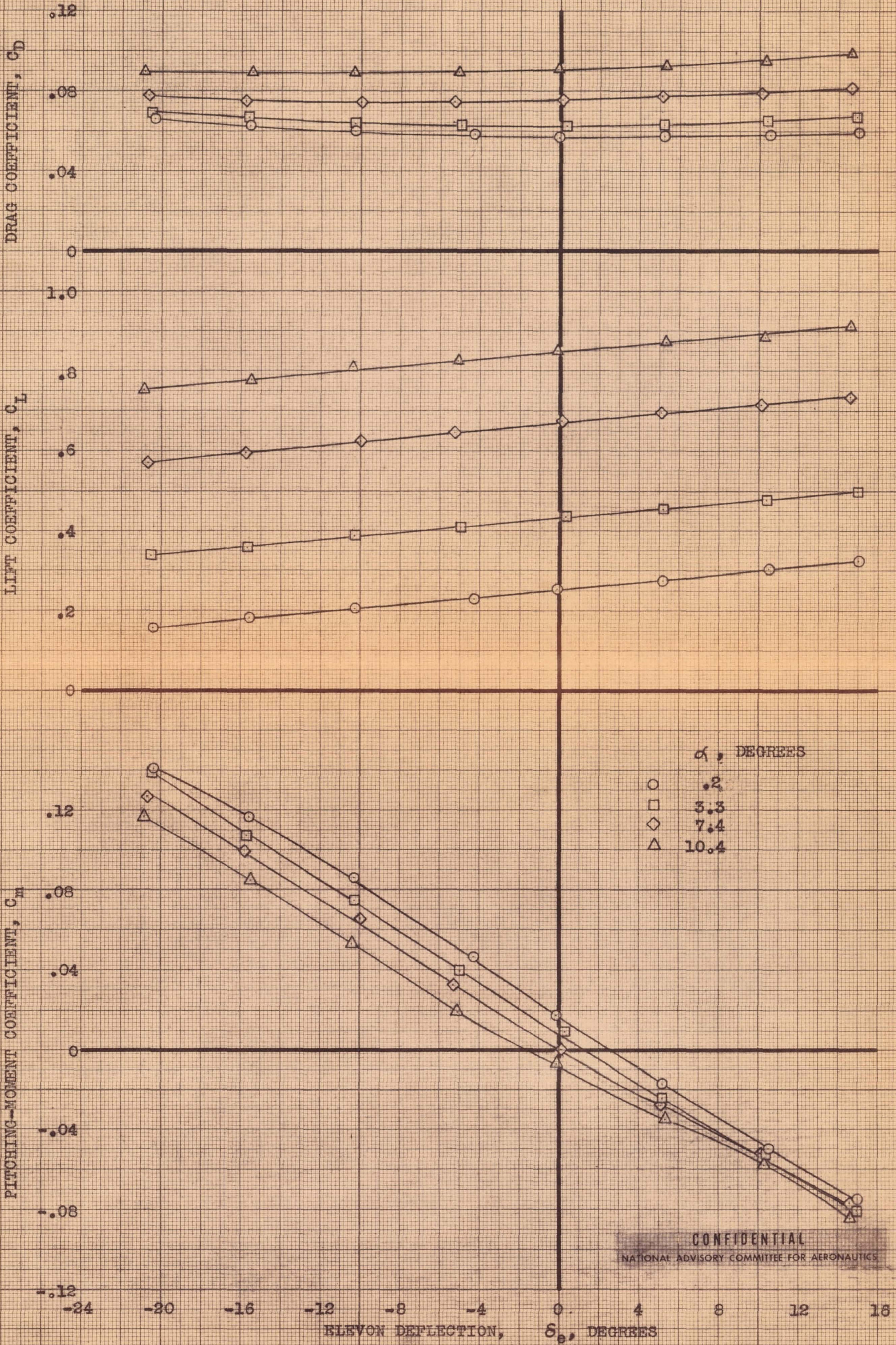

FIGURE 14.- VARIATION, WITH ELEVON DEFLECTION, OF THE AERODYNAMIC CHARACTERISTICS OF THE MISSILE AT SEVERAL ANGLES OF ATTACK WITH TRAILING-EDGE FLAPS DEFLECTED 45°. β, 0°; R, 11×10^6.

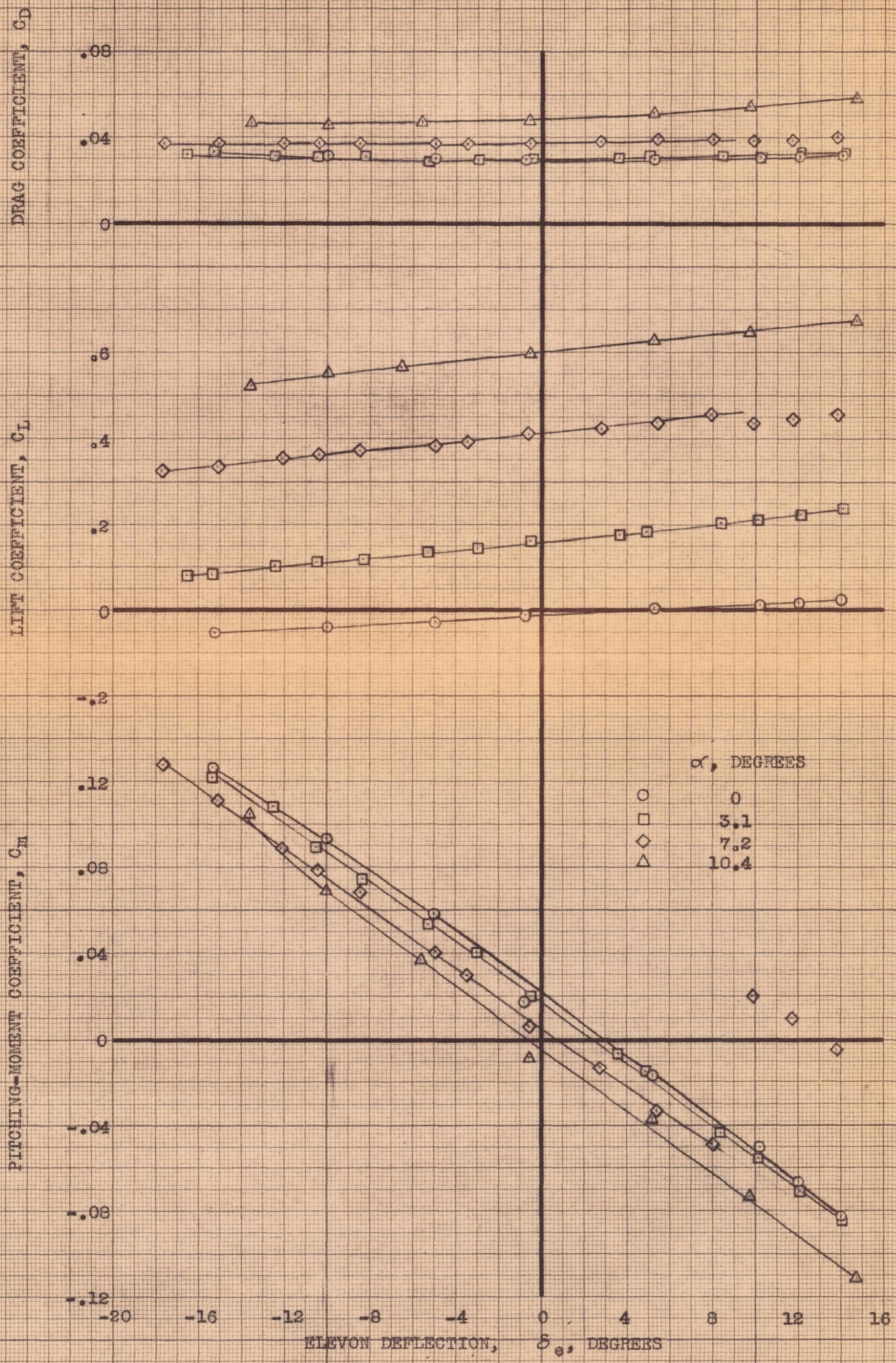

(a) R, 11 X 10^6.

FIGURE 15.- VARIATION, WITH ELEVON DEFLECTION, OF THE AERODYNAMIC CHARACTERISTICS OF THE MISSILE AT SEVERAL ANGLES OF ATTACK WITH SLAB-SIDED ELEVONS. β, 0°.

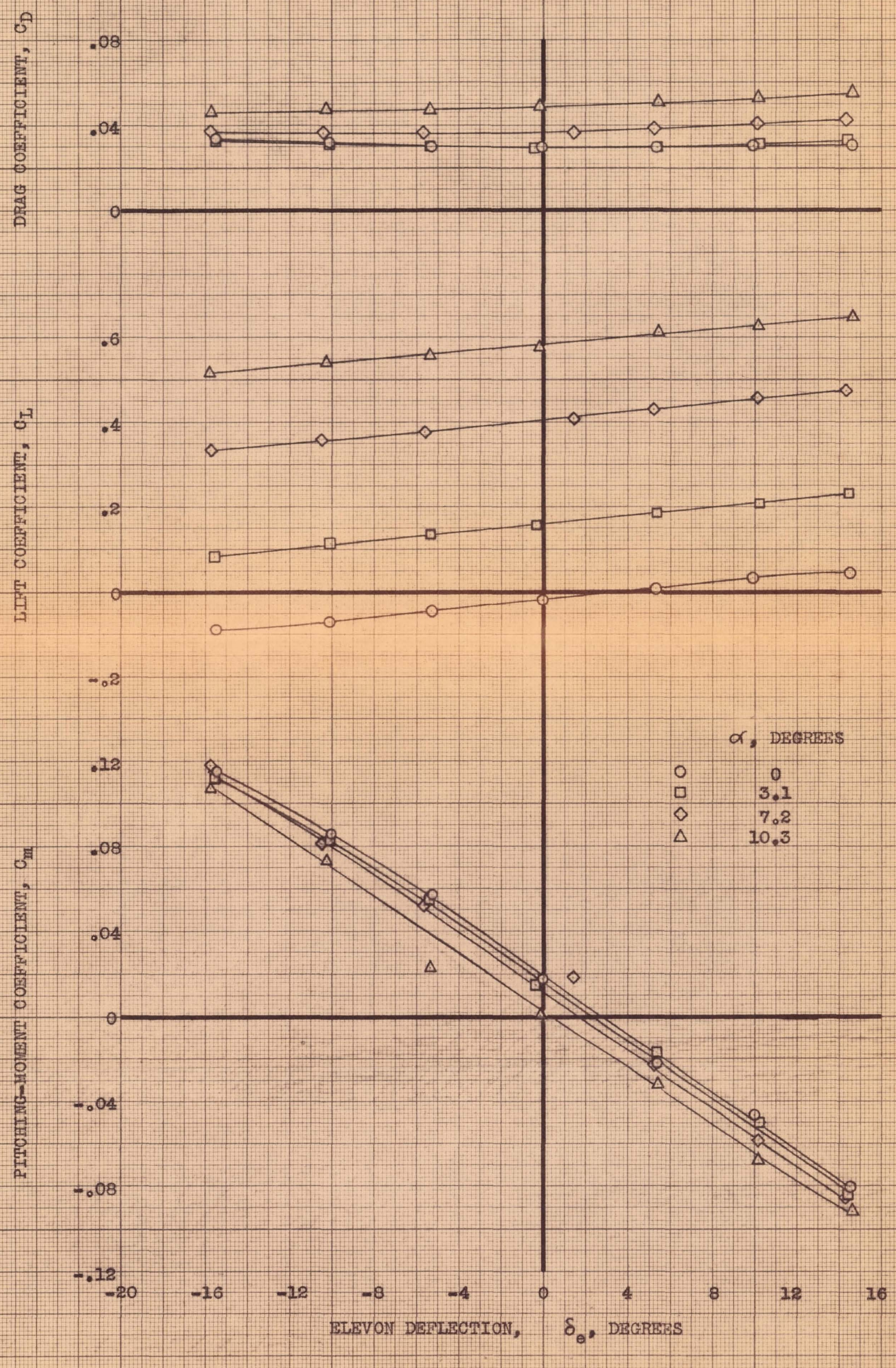

(b) R, 12.5 X 10^6.

FIGURE 15.- CONCLUDED.

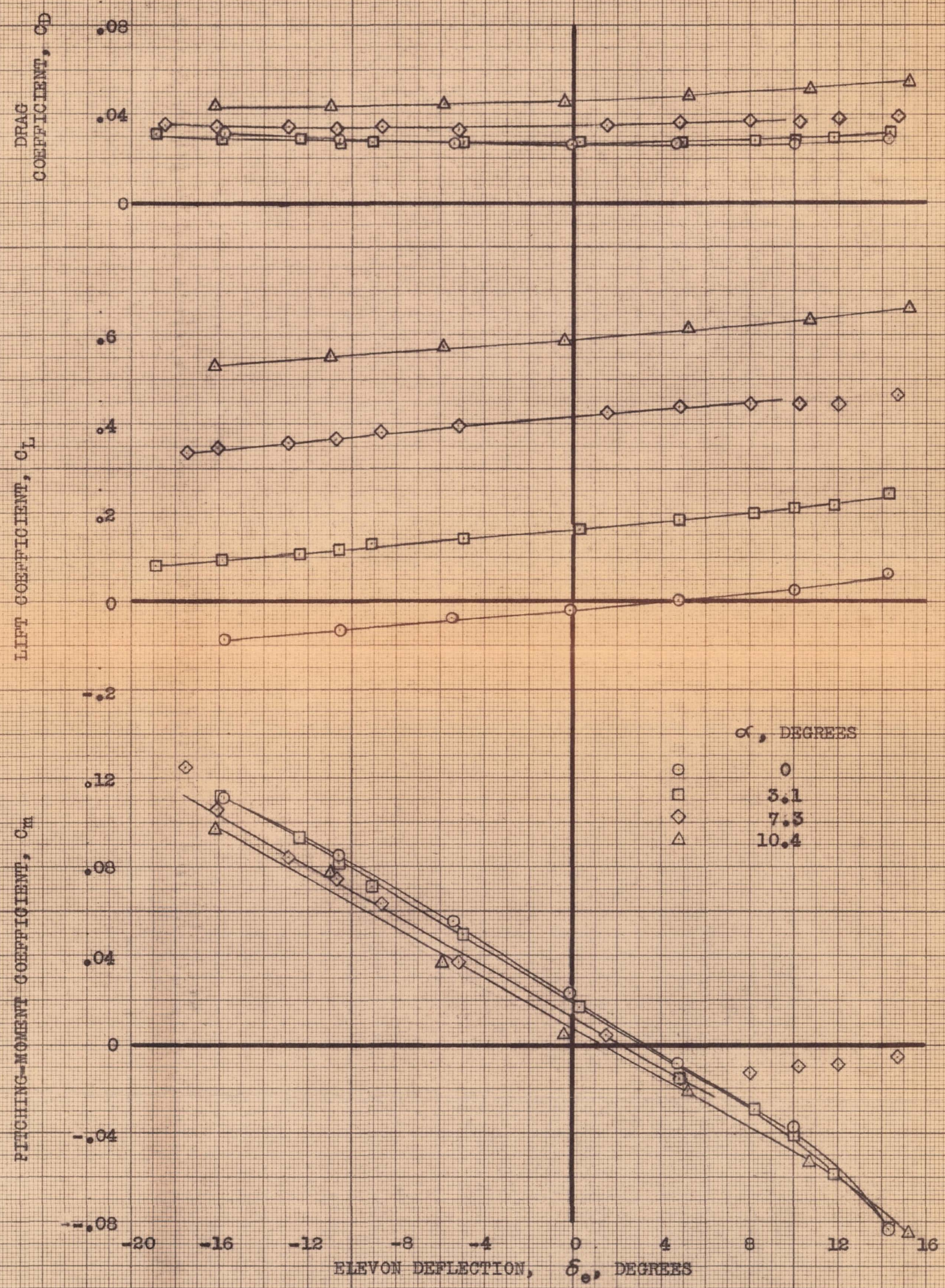

(a) C_D, C_L, C_m vs δ_e.

FIGURE 16.- VARIATION, WITH ELEVON DEFLECTION, OF THE AERODYNAMIC CHARACTERISTICS OF THE MISSILE AT SEVERAL ANGLES OF ATTACK. R, 11 X 10^6; β, - 3°.

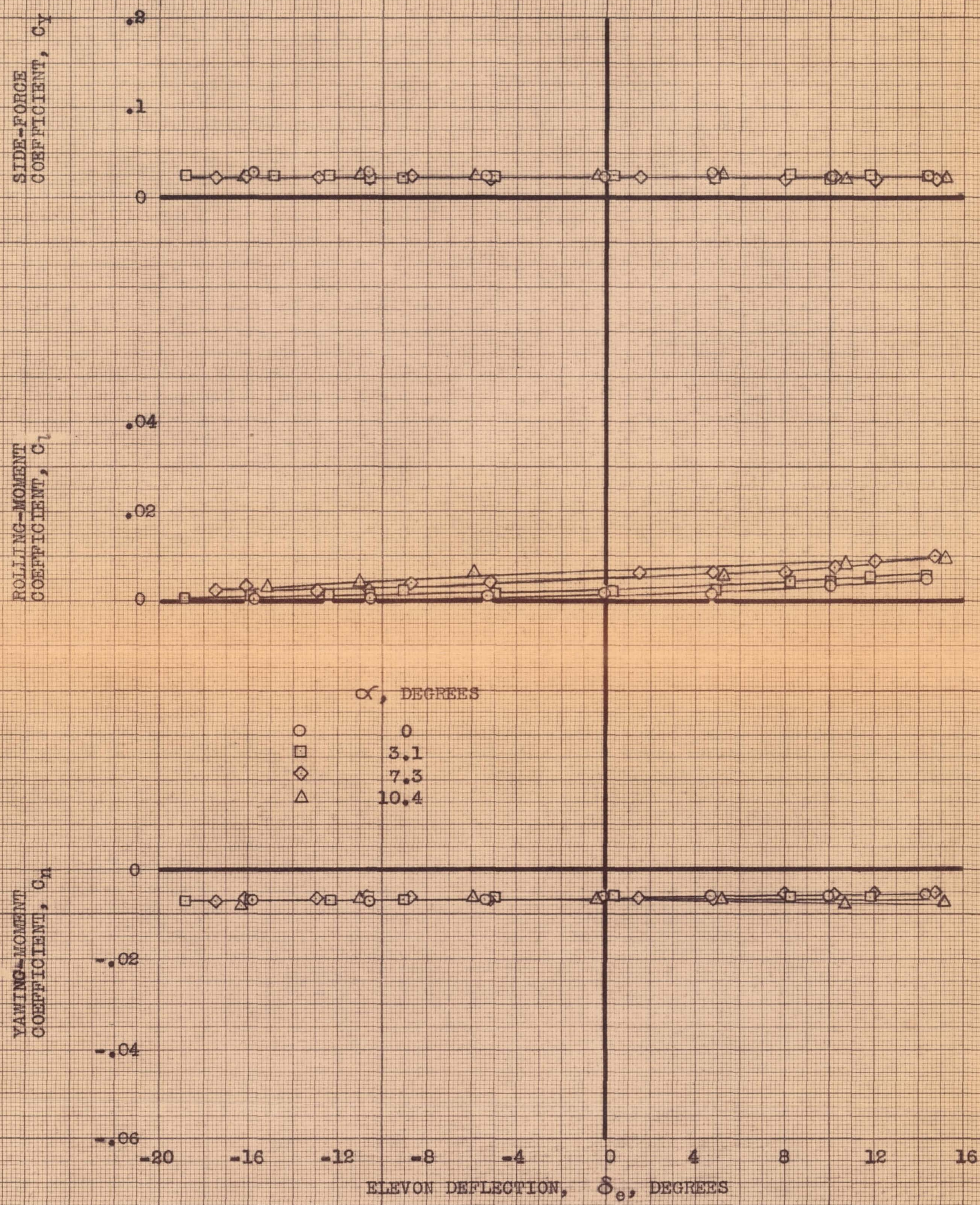

(b) C_Y, C_l, C_n vs δ_e.

FIGURE 16.- CONCLUDED.

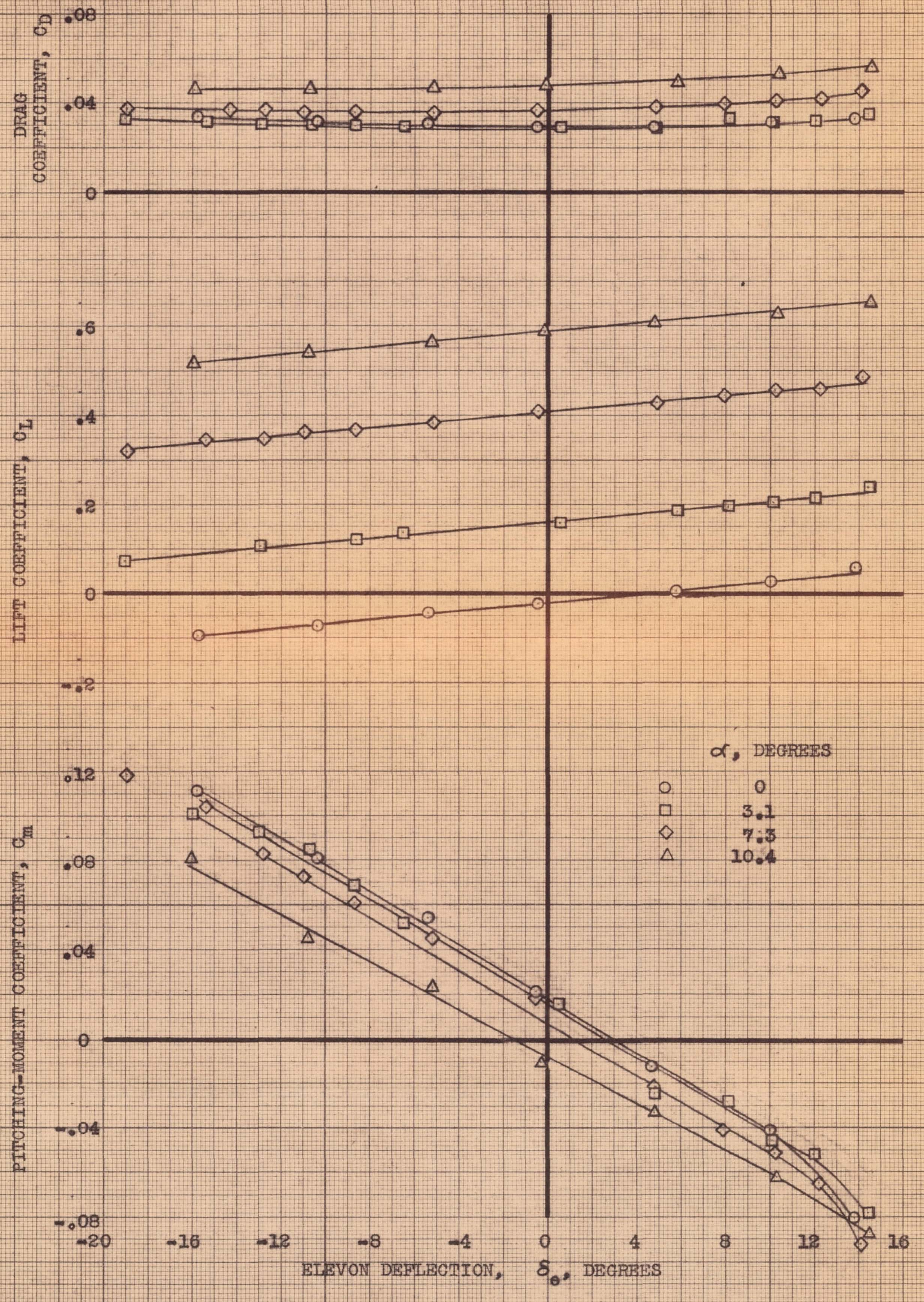

(a) C_D, C_L, C_m vs δ_e.

FIGURE 17.- VARIATION, WITH ELEVON DEFLECTION, OF THE AERODYNAMIC CHARACTERISTICS OF THE MISSILE AT SEVERAL ANGLES OF ATTACK. R, 11 X 10^6; β, -7°.

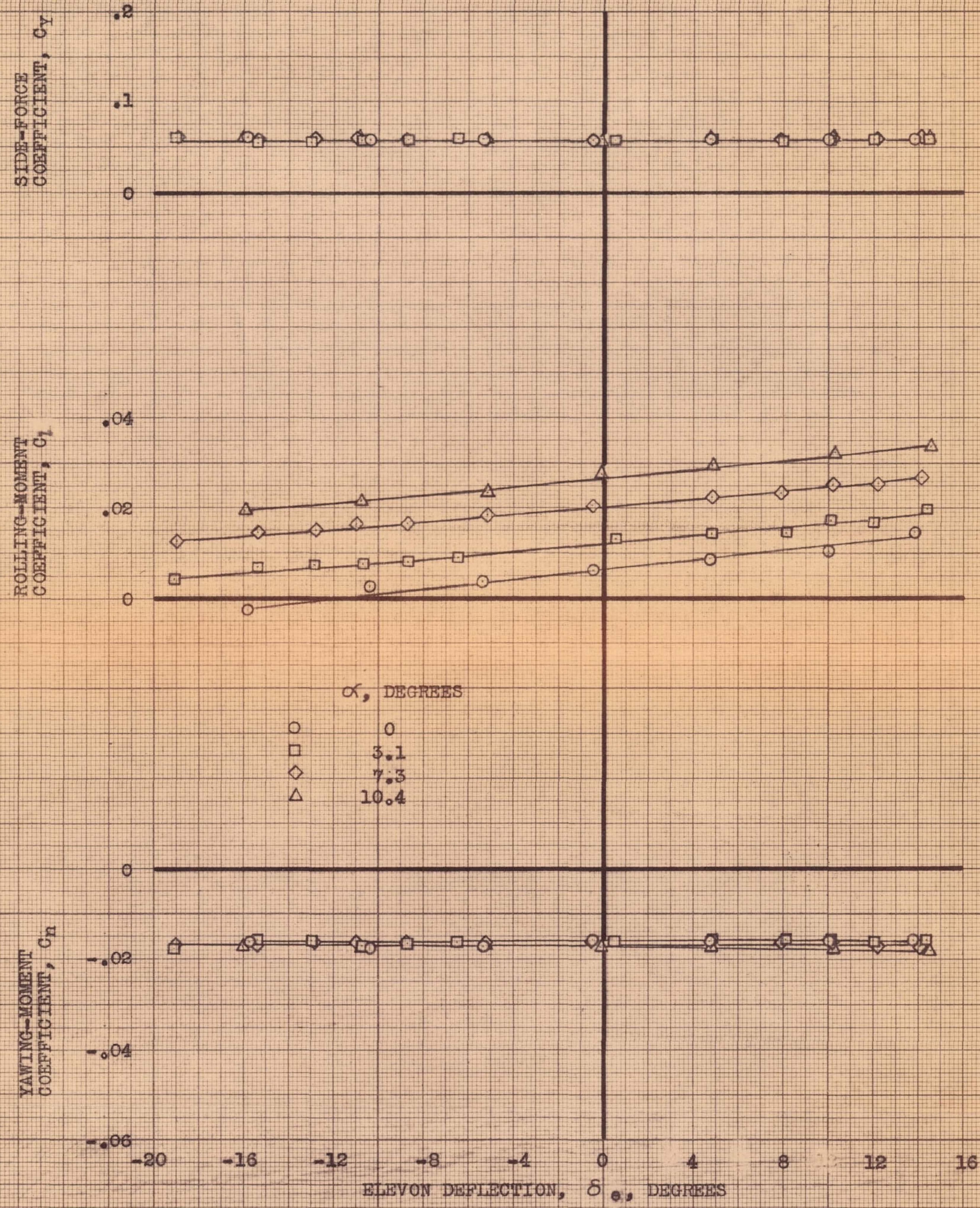

(b) C_Y, C_l, C_n vs δ_e.

FIGURE 17.- CONCLUDED.

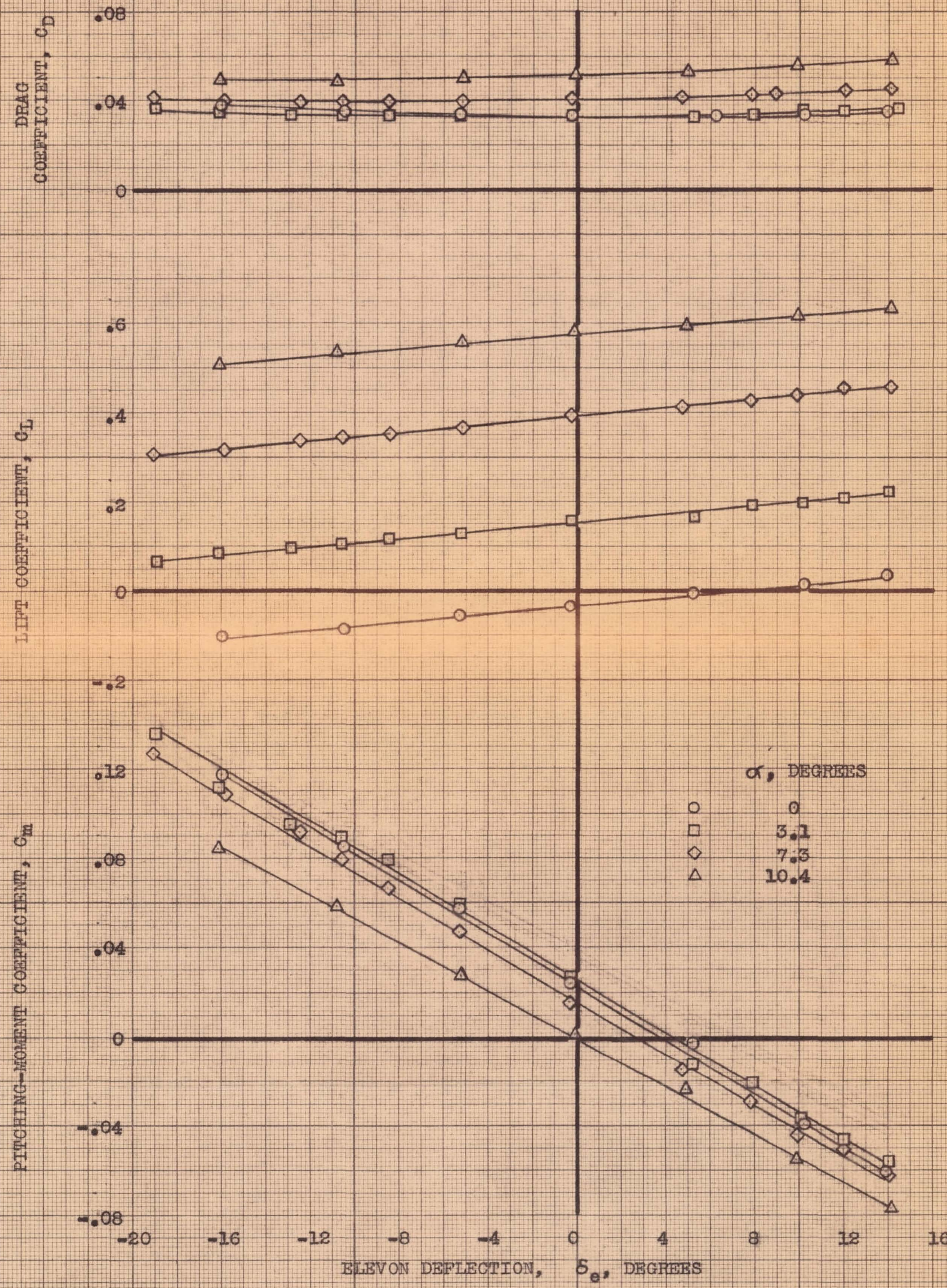

(a) C_D, C_L, C_m vs δ_e.

FIGURE 18.- VARIATION, WITH ELEVON DEFLECTION, OF THE AERODYNAMIC CHARACTERISTICS OF THE MISSILE AT SEVERAL ANGLES OF ATTACK. R, 11 x 10^6; β, -10°.

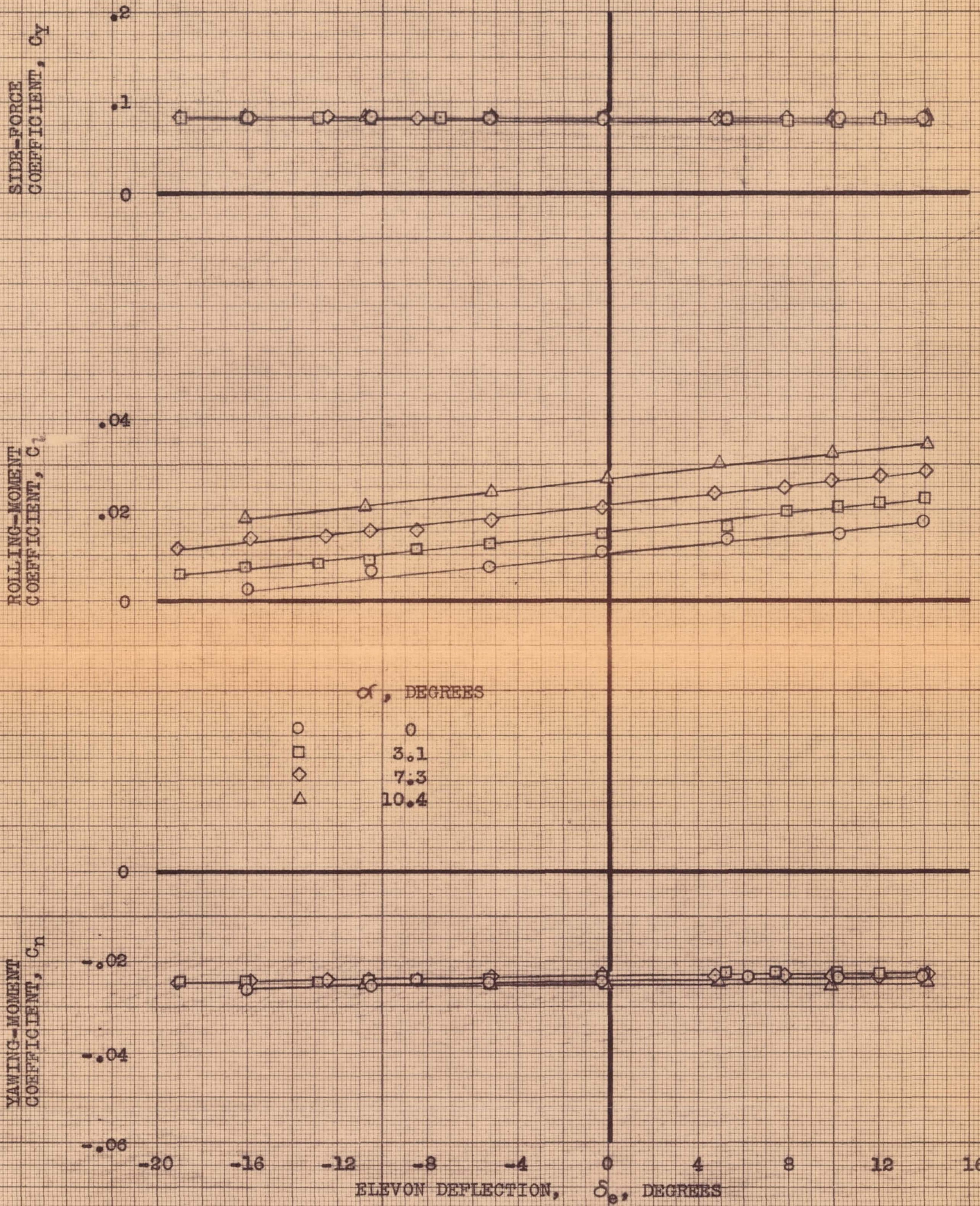

(b) C_Y, C_l, C_n vs δ_e.

FIGURE 18.- CONCLUDED.

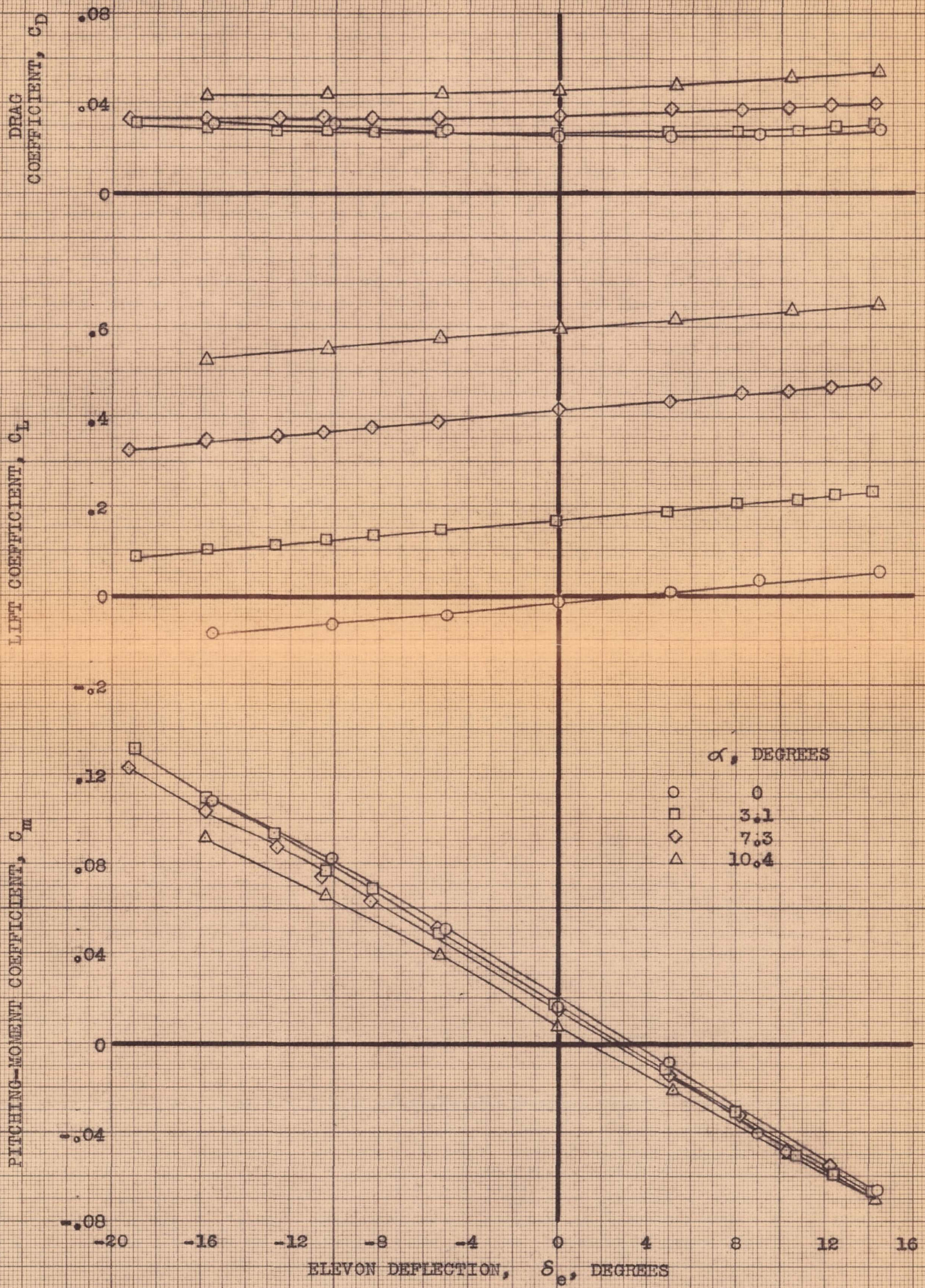

(a) C_D, C_L, C_m vs δ_e.

FIGURE 19.- VARIATION, WITH ELEVON DEFLECTION, OF THE AERODYNAMIC CHARACTERISTICS OF THE MISSILE AT SEVERAL ANGLES OF ATTACK. R, 11 X 10^6; β, 3°.

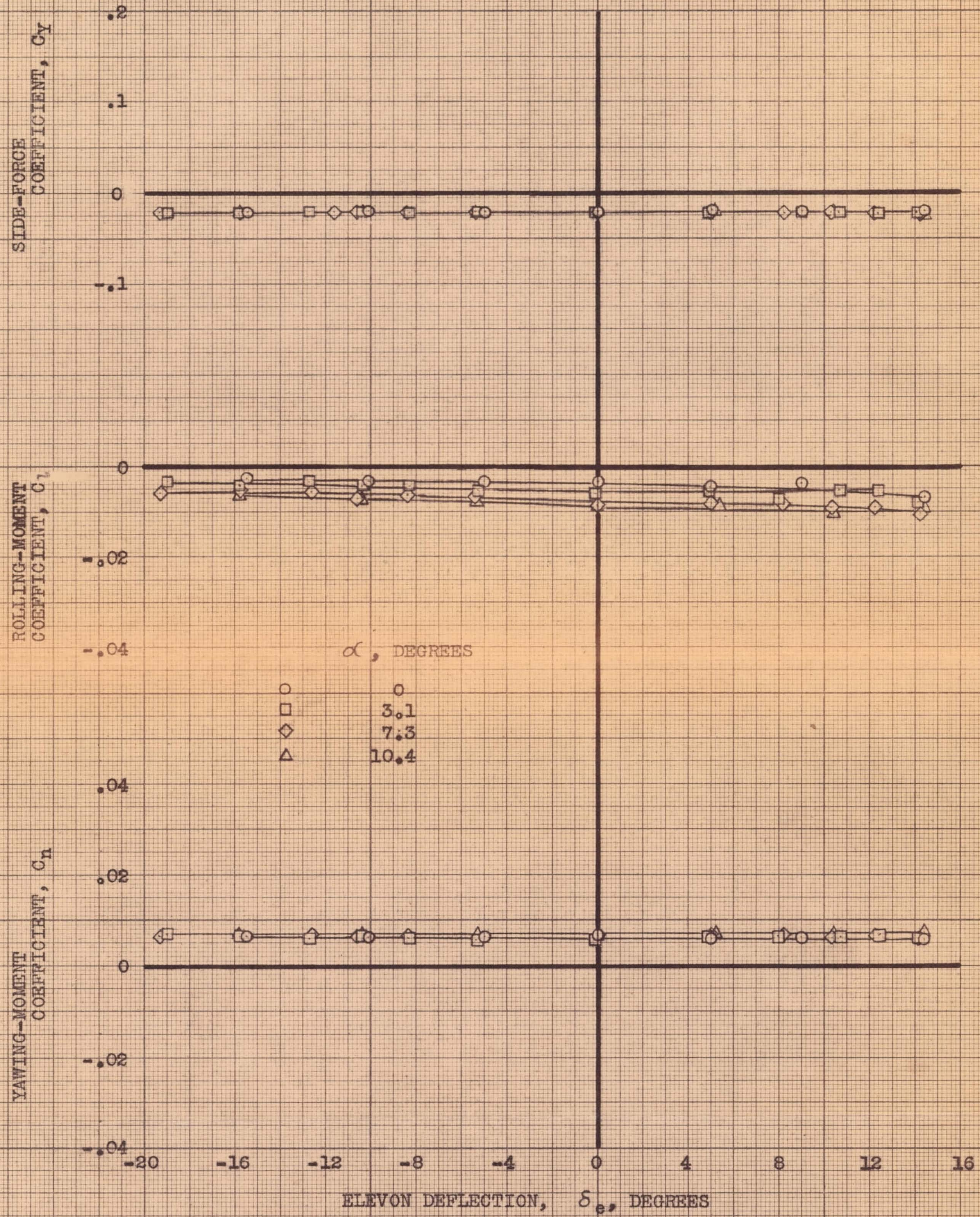

(b) C_Y, C_l, C_n vs δ_e.

FIGURE 19.- CONCLUDED.

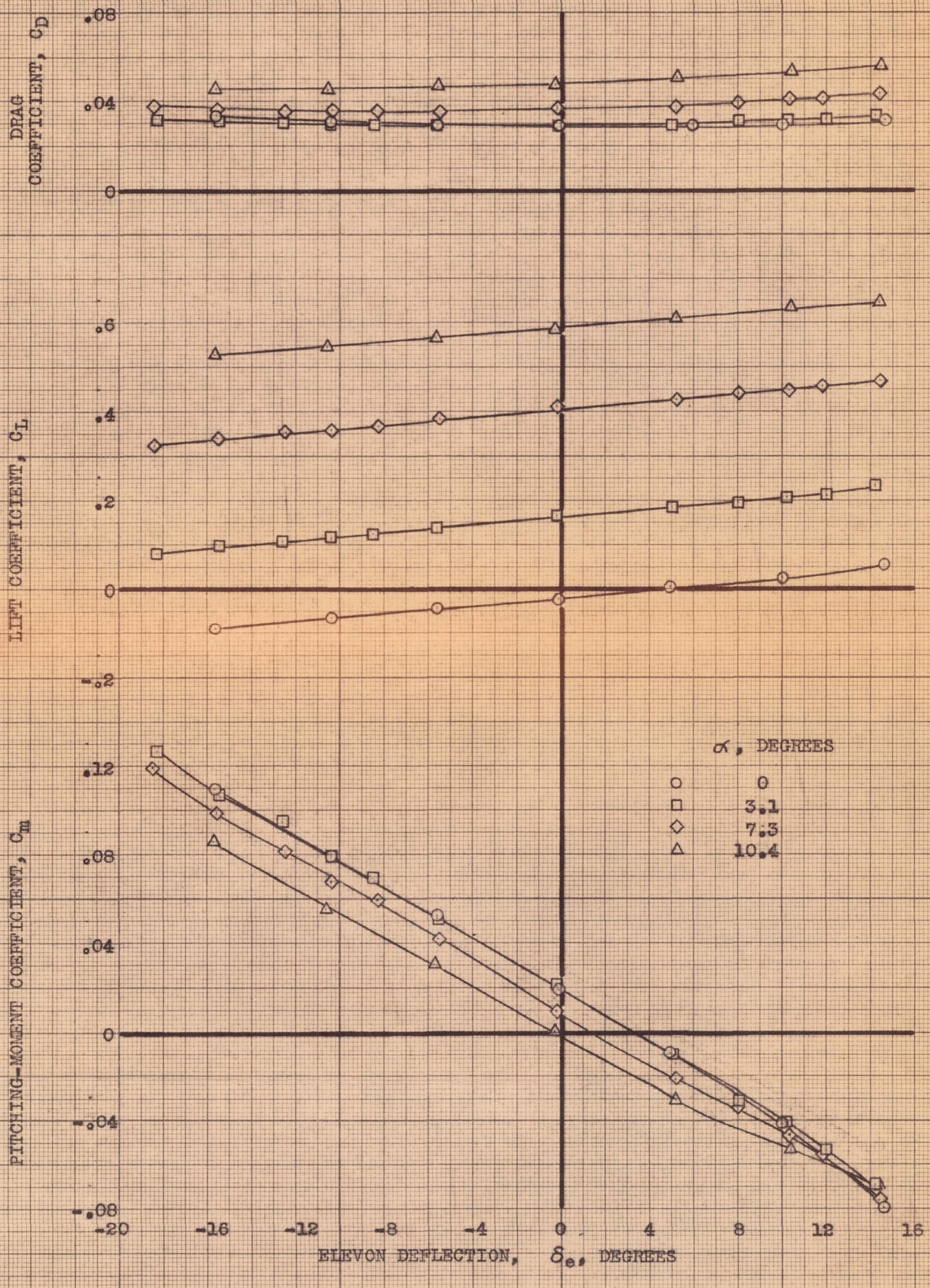

(a) C_D, C_L, C_m vs δ_e.

FIGURE 20.- VARIATION, WITH ELEVON DEFLECTION, OF THE AERODYNAMIC CHARACTERISTICS OF THE MISSILE AT SEVERAL ANGLES OF ATTACK. R, 11 X 10^6; β, 7°.

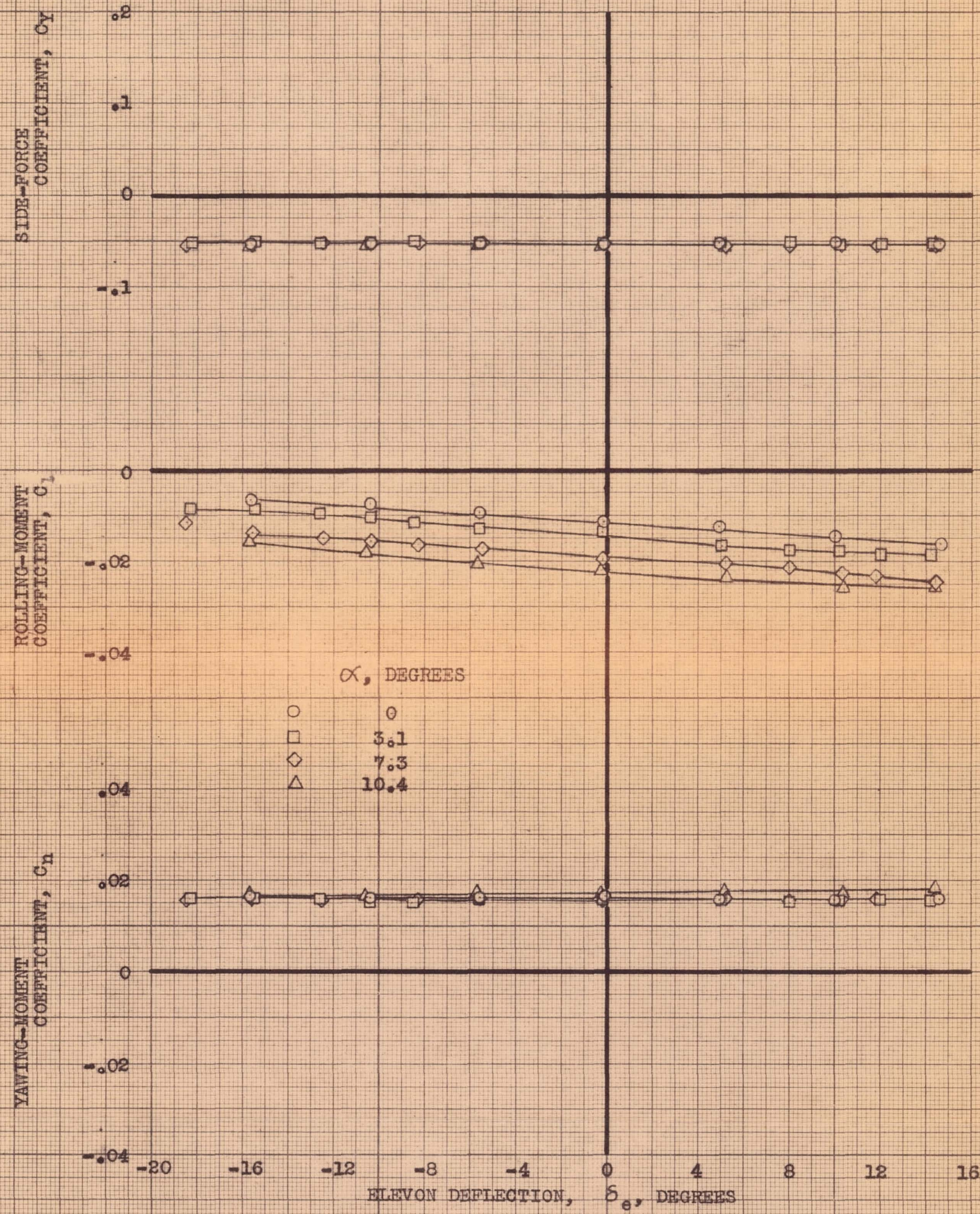

(b) C_Y, C_l, C_n vs δ_e.

FIGURE 20.- CONCLUDED.

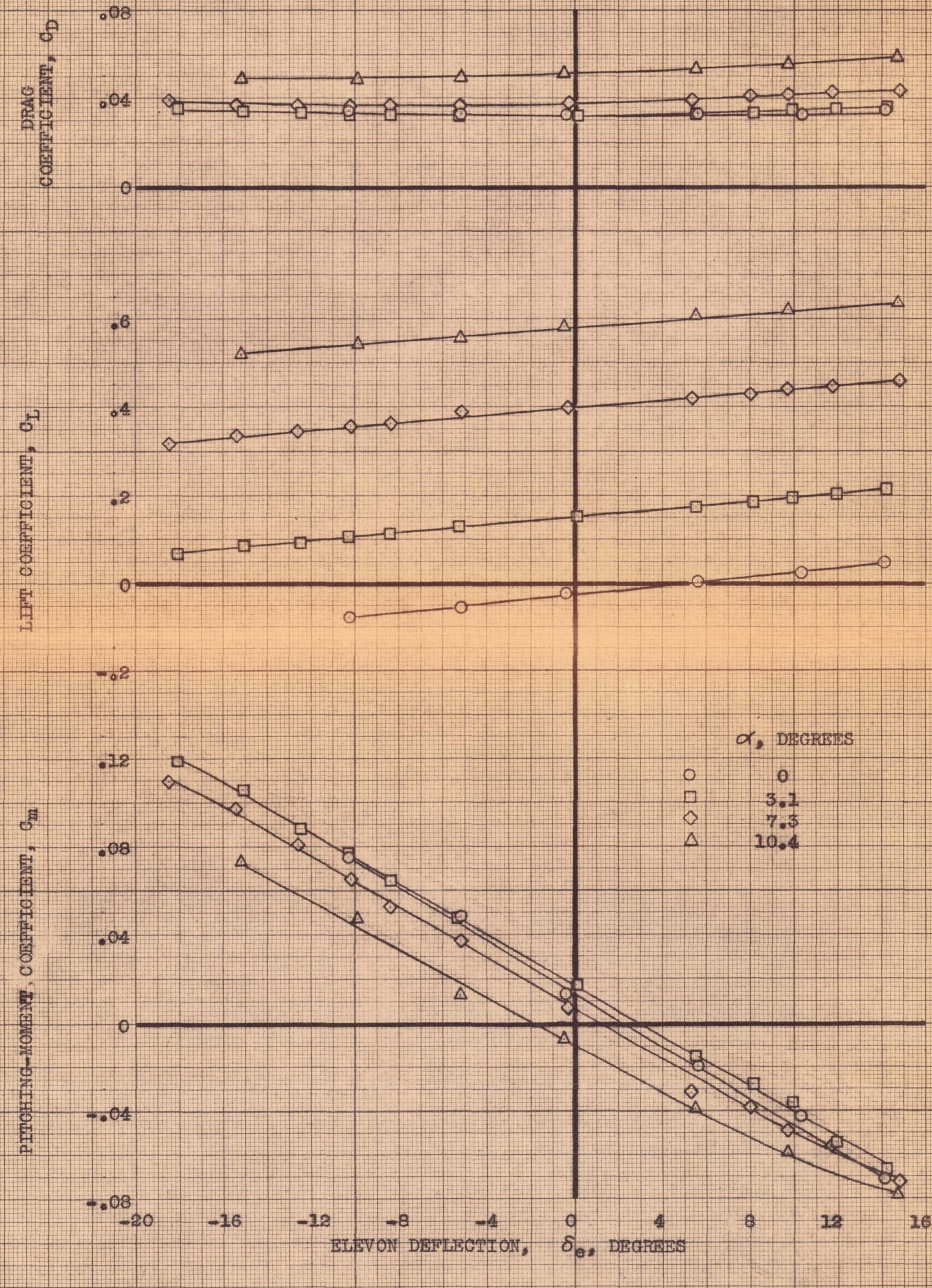

(a) C_D, C_L, C_m vs δ_e.

FIGURE 21.- VARIATION, WITH ELEVON DEFLECTION, OF THE AERODYNAMIC CHARACTERISTICS OF THE MISSILE AT SEVERAL ANGLES OF ATTACK. R, 11 X 10^6; β, 10°.

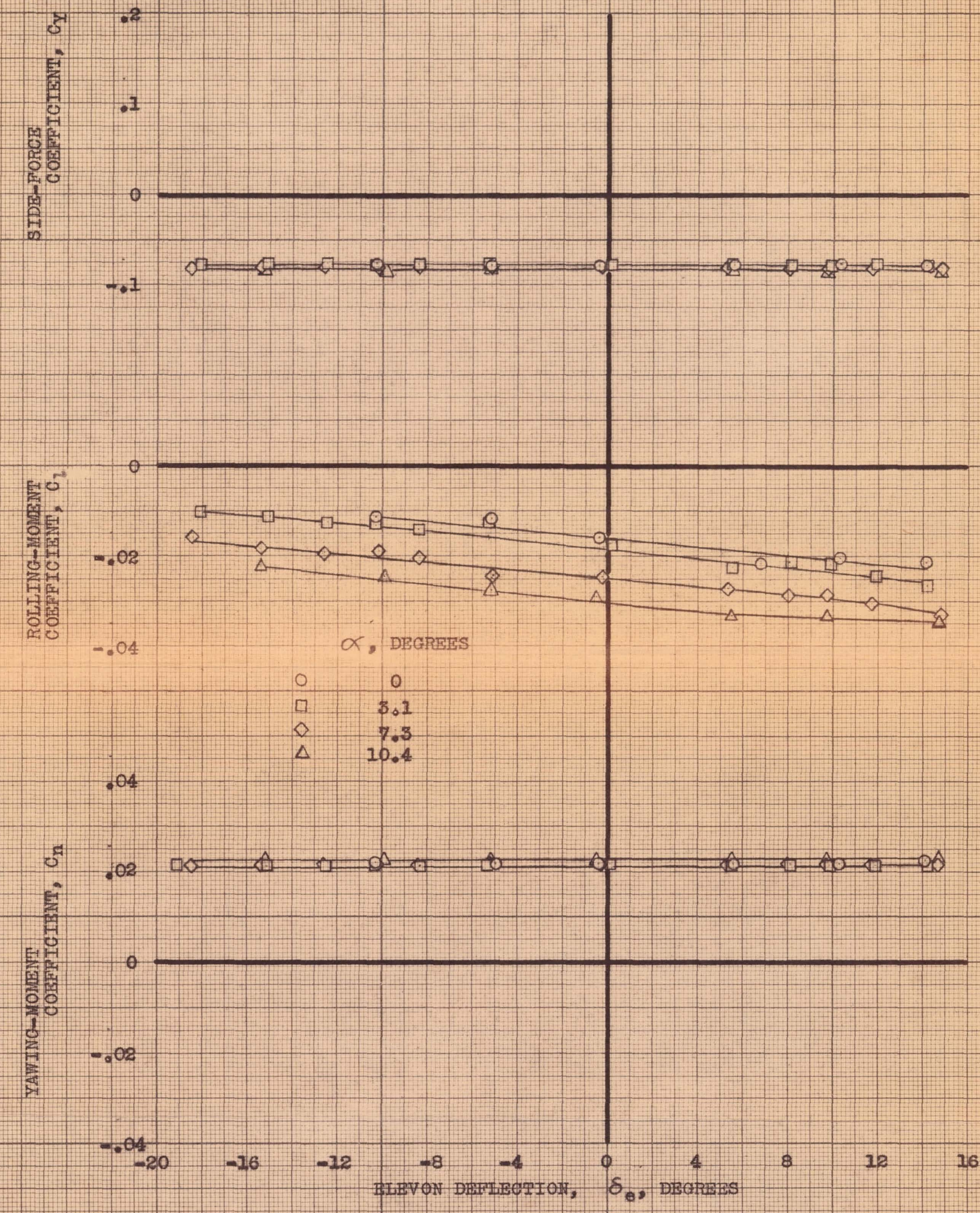

(b) C_Y, C_l, C_n vs δ_e.

FIGURE 21.- CONCLUDED.

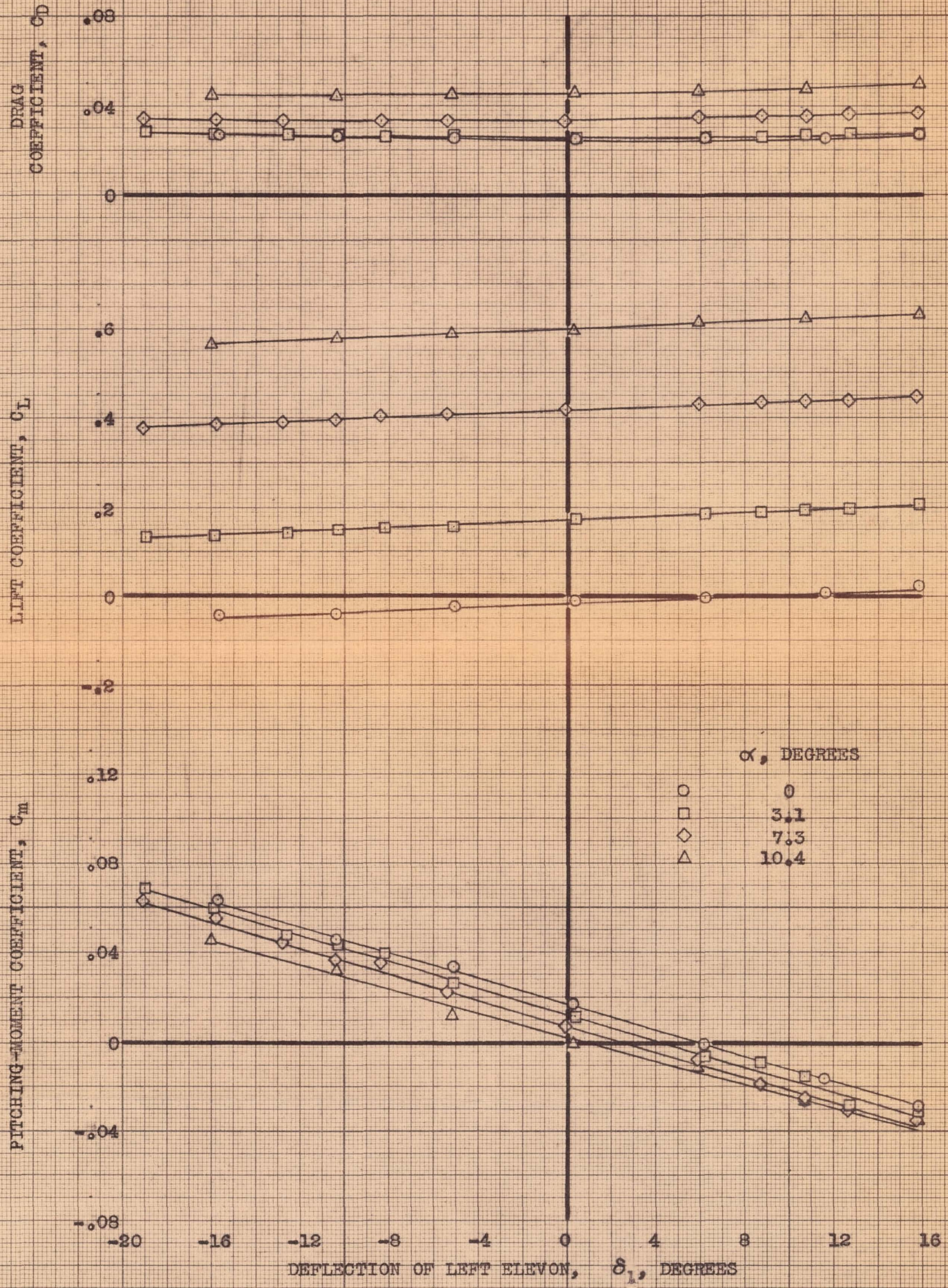

(a) C_D, C_L, C_m vs δ_l.

FIGURE 22.- VARIATION, WITH LEFT ELEVON DEFLECTION, OF THE AERODYNAMIC CHARACTERISTICS OF THE MISSILE AT SEVERAL ANGLES OF ATTACK. δ_r, 0°; R, 11 X 10^6; β, 0°.

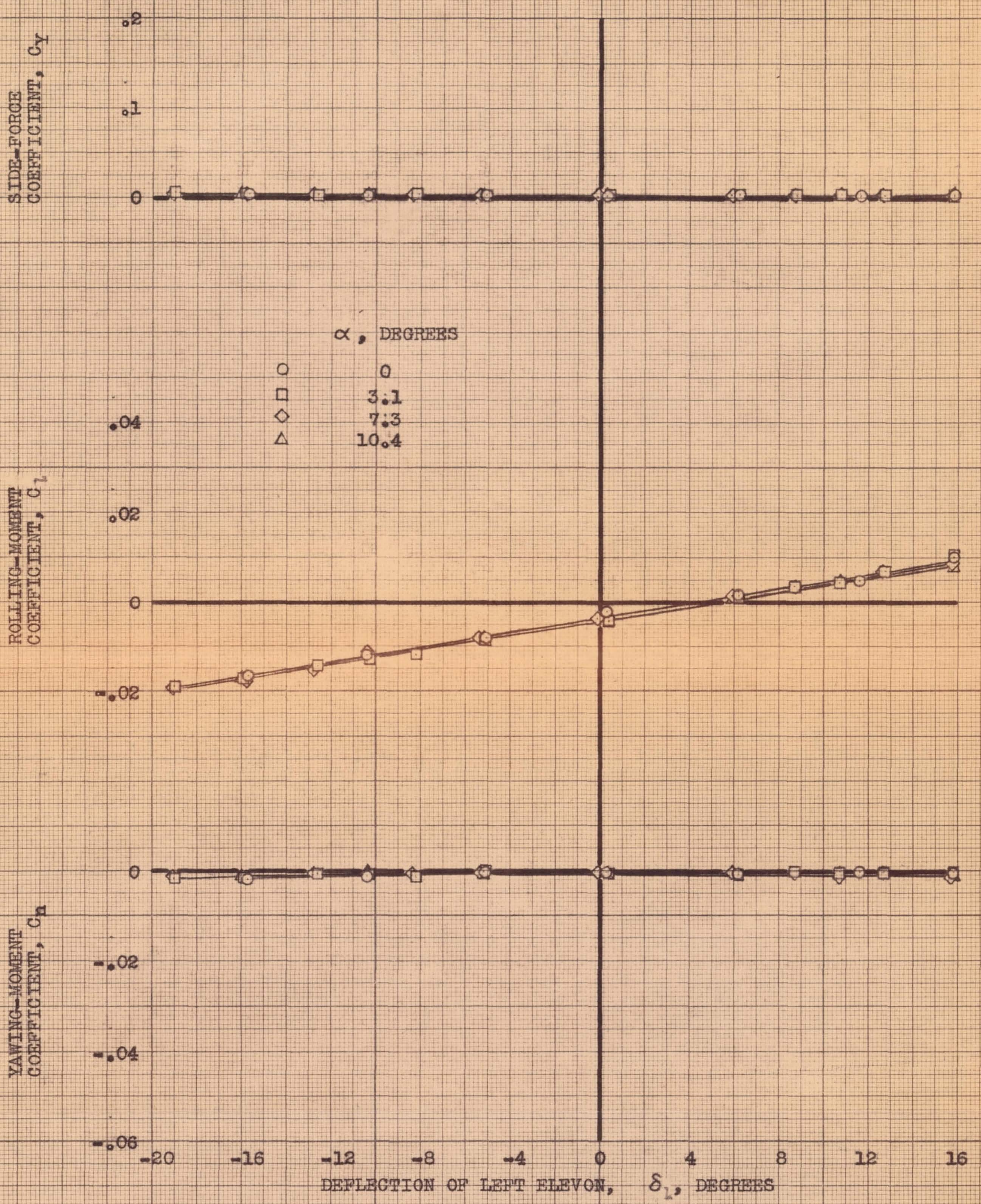

(b) C_Y, C_l, C_n vs δ_l.

FIGURE 22.- CONCLUDED.

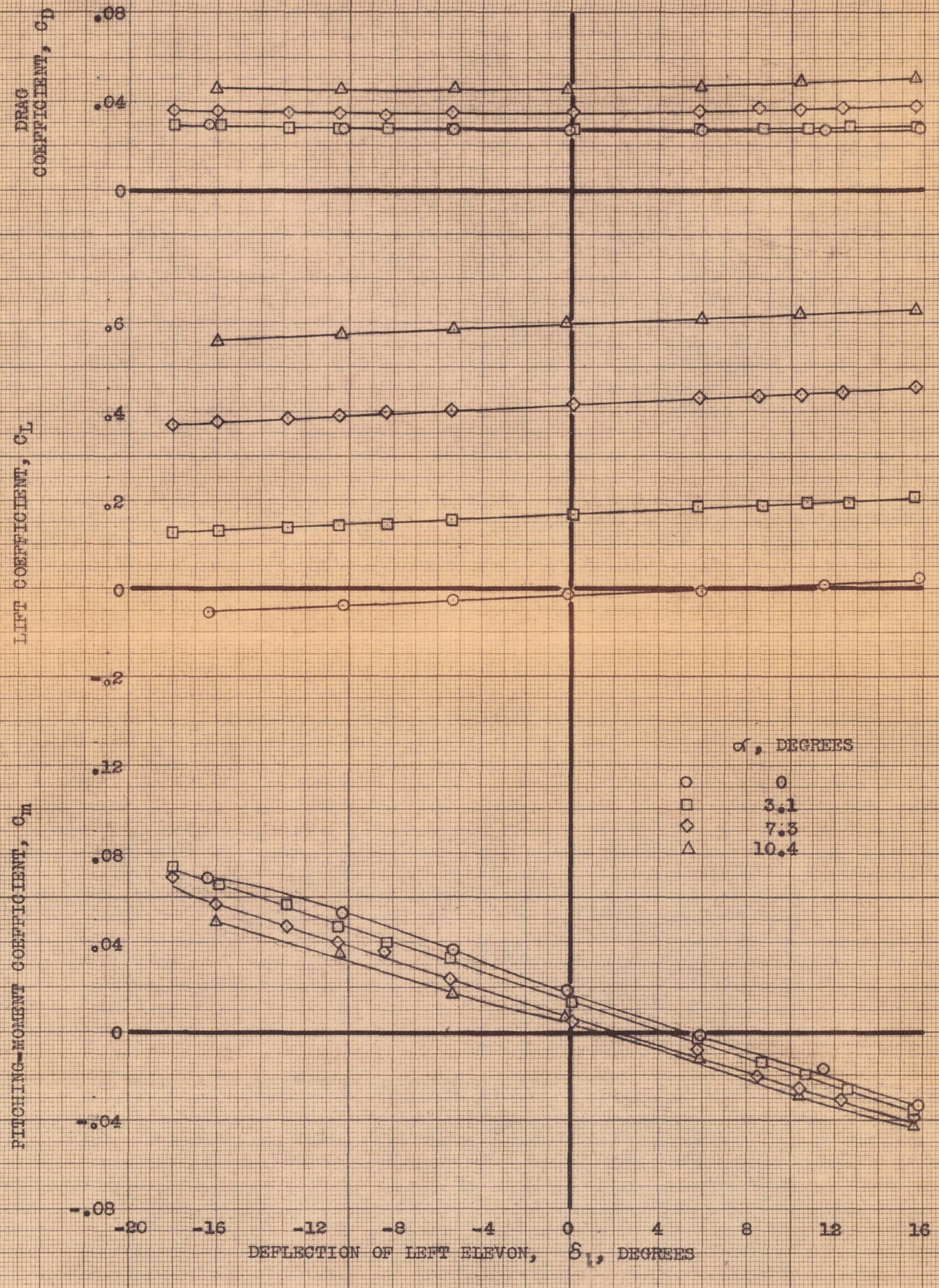

(a) C_D, C_L, C_m vs δ_l.

FIGURE 23.- VARIATION, WITH LEFT ELEVON DEFLECTION, OF THE AERODYNAMIC CHARACTERISTICS OF THE MISSILE AT SEVERAL ANGLES OF ATTACK. δ_r, 0°; R, 11 X 10^6; β, -3°.

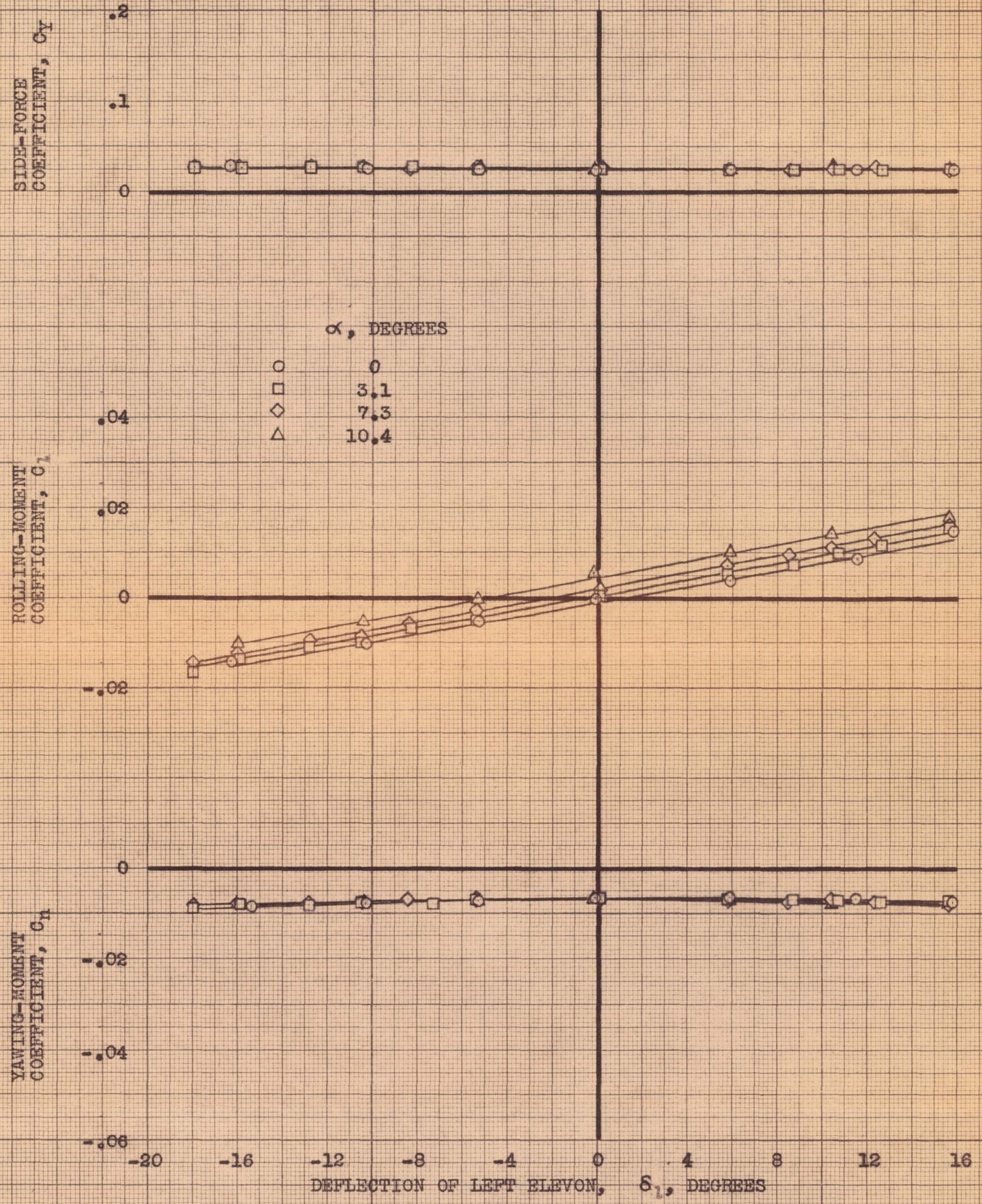

(b) C_Y, C_l, C_n vs δ_l.

FIGURE 23.- CONCLUDED.

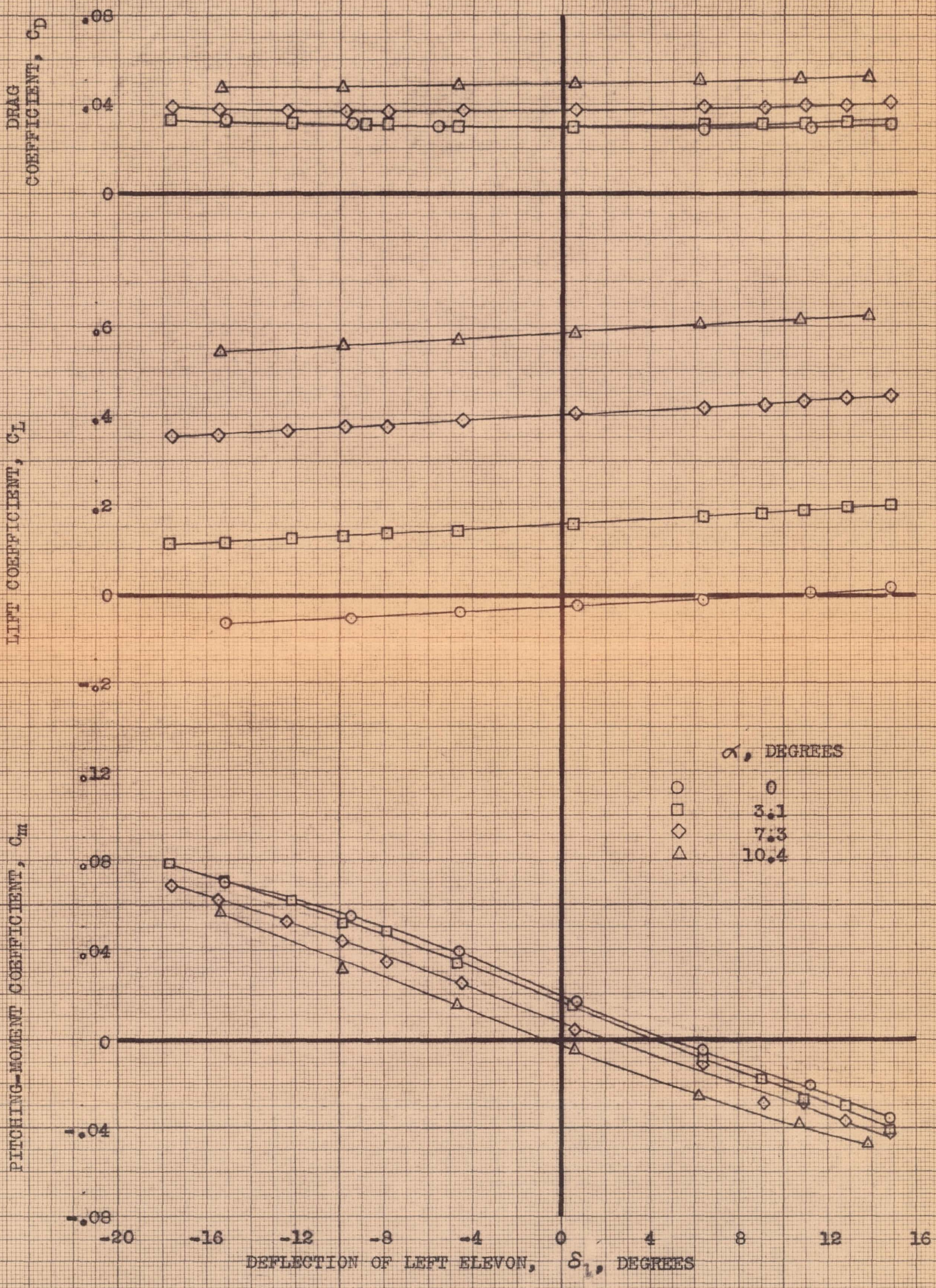

(a) C_D, C_L, C_m vs δ_l.

FIGURE 24.- VARIATION, WITH LEFT ELEVON DEFLECTION, OF THE AERODYNAMIC CHARACTERISTICS OF THE MISSILE AT SEVERAL ANGLES OF ATTACK. δ_r, 0°; R, 11×10^6; β, -7°.

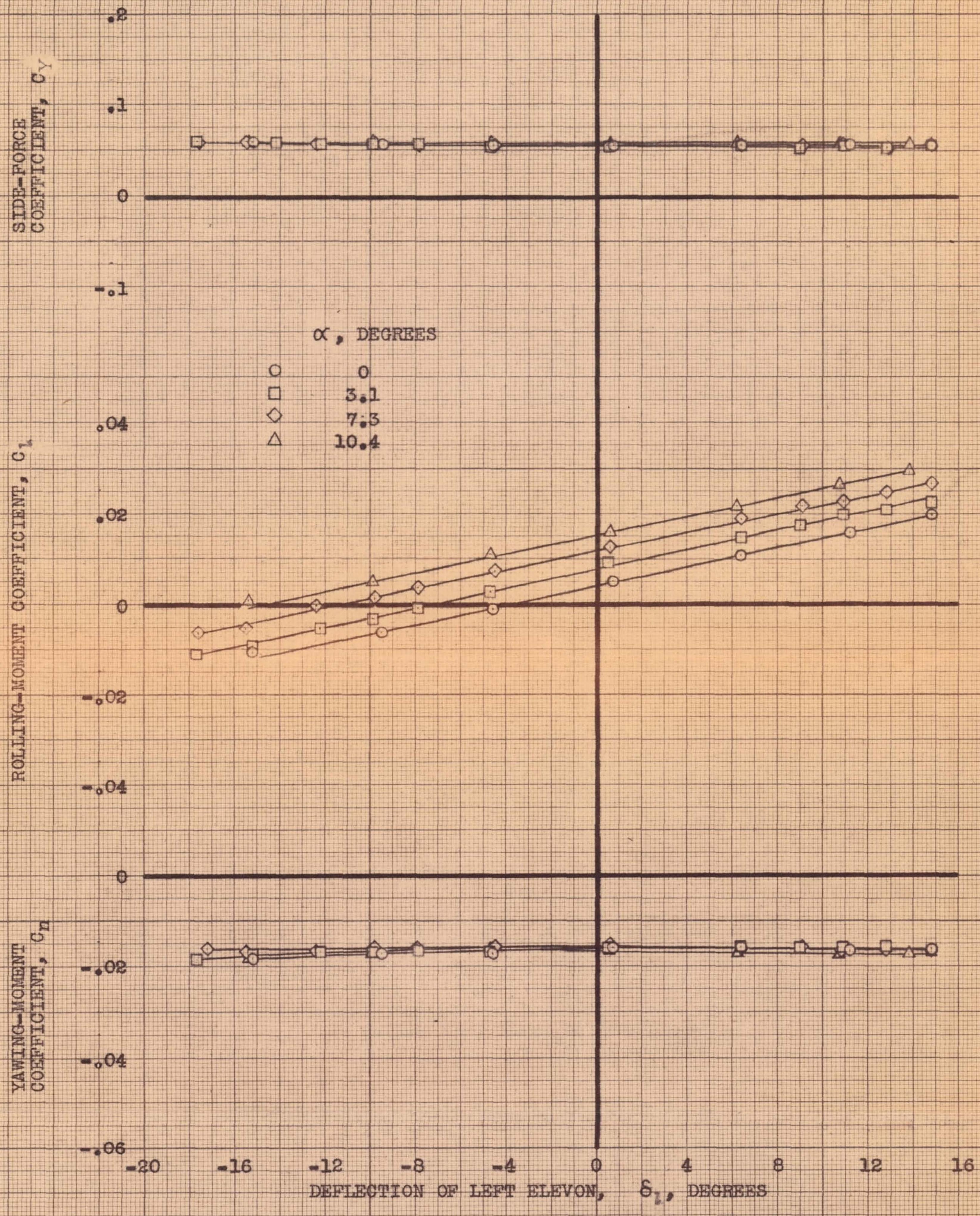

(b) C_Y, C_l, C_n vs δ_l.

FIGURE 24.- CONCLUDED.

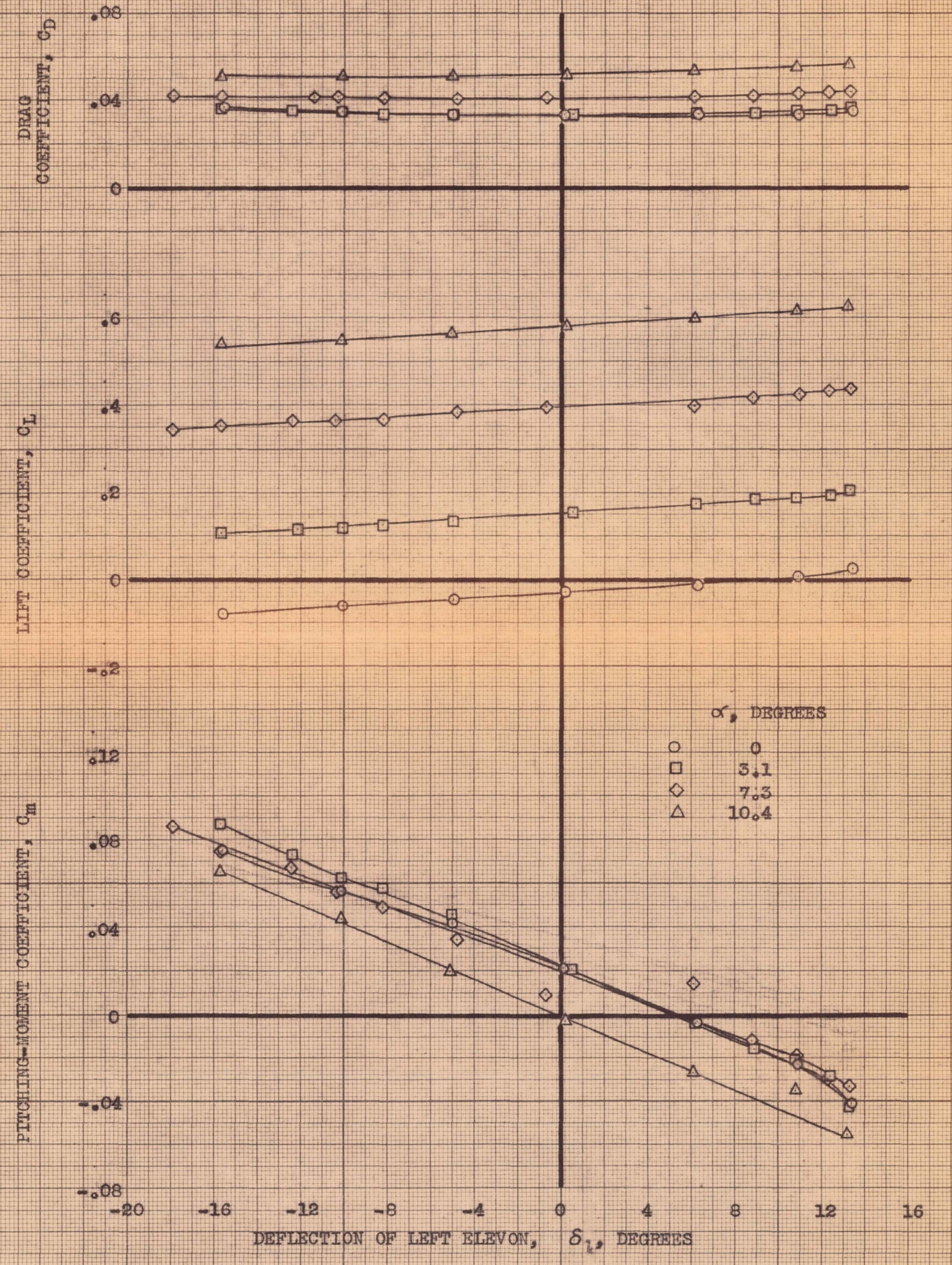

(a) C_D, C_L, C_m vs δ_l.

FIGURE 25.- VARIATION, WITH LEFT ELEVON DEFLECTION, OF THE AERODYNAMIC CHARACTERISTICS OF THE MISSILE AT SEVERAL ANGLES OF ATTACK. δ_r, 0°; R, 11 X 10^6; β, -10°.

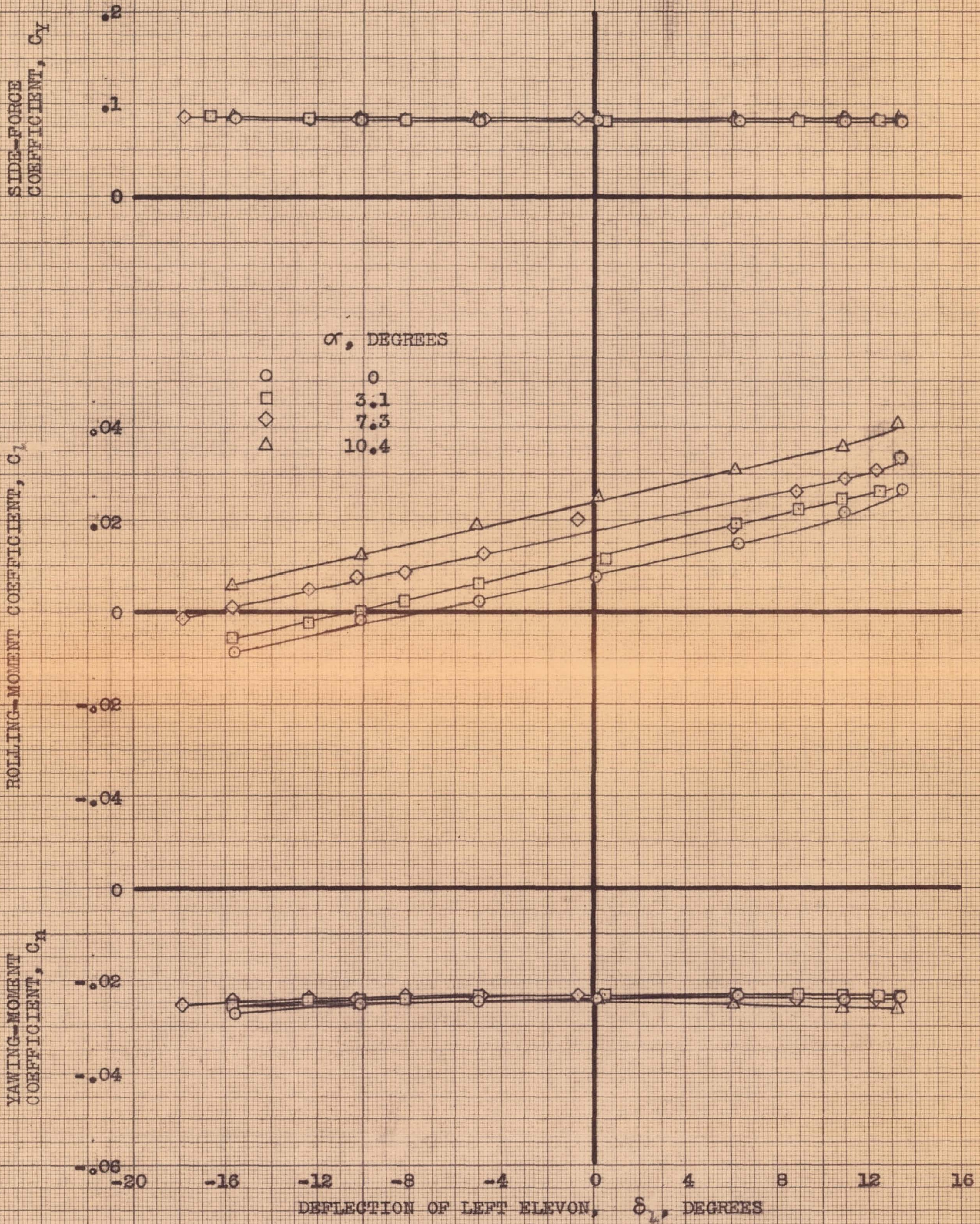

(b) C_Y, C_l, C_n vs δ_l.

FIGURE 25.- CONCLUDED.

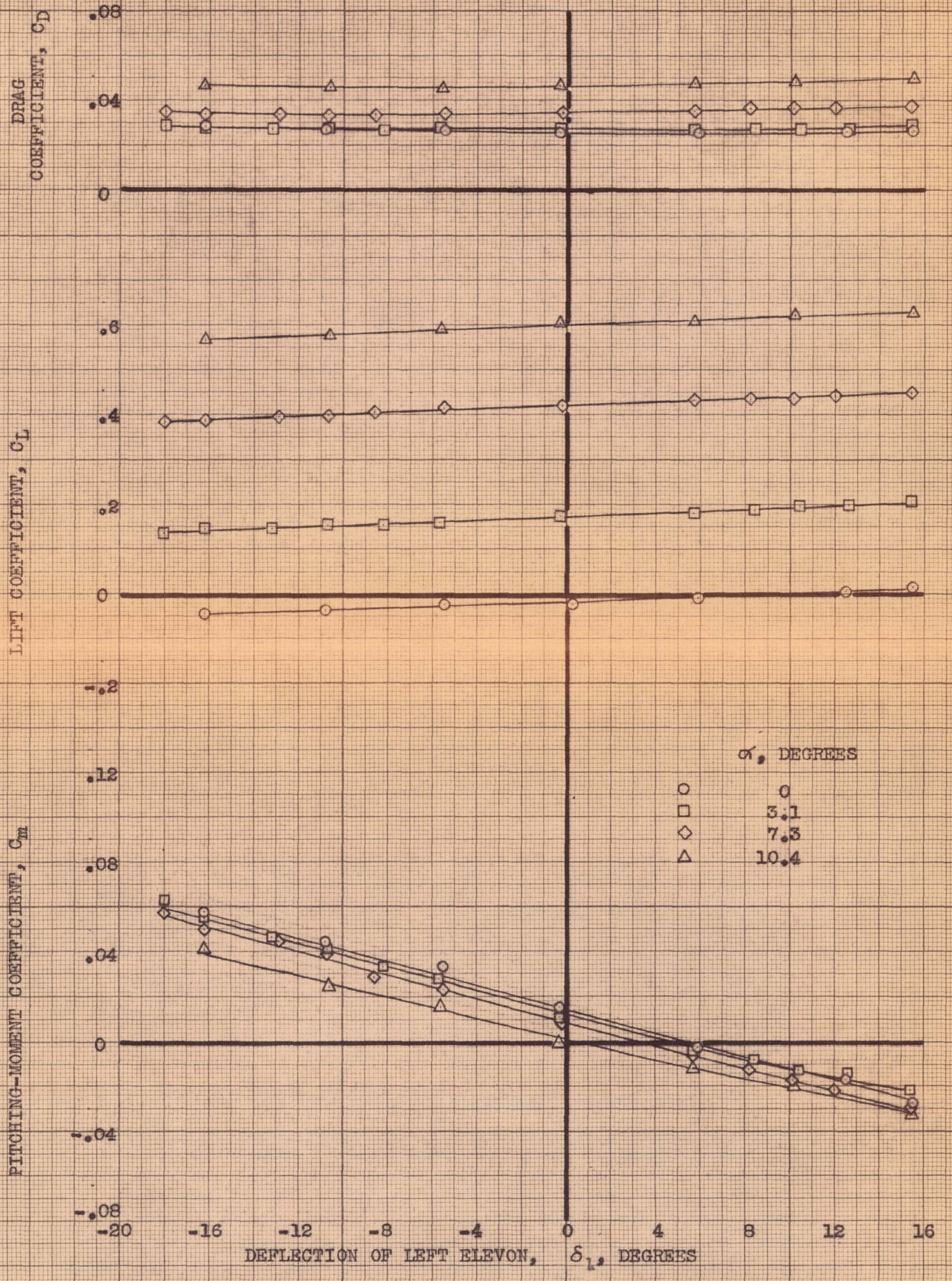

(a) C_D, C_L, C_m vs δ_l.

FIGURE 26.- VARIATION, WITH LEFT ELEVON DEFLECTION, OF THE AERODYNAMIC CHARACTERISTICS OF THE MISSILE AT SEVERAL ANGLES OF ATTACK. δ_r, 0°; R, 11 X 10^6; β, 3°.

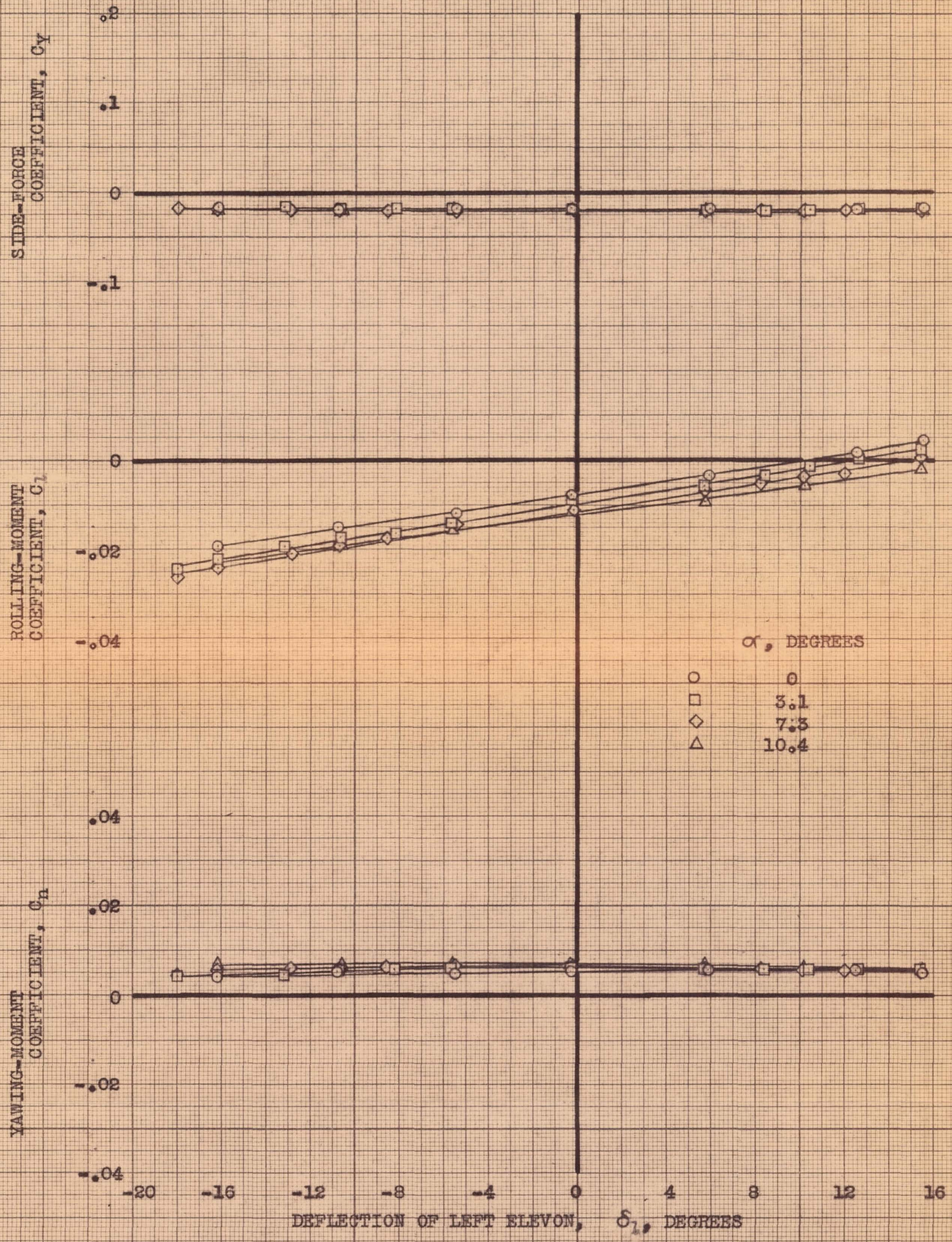

(b) C_Y, C_l, C_n vs δ_l.

FIGURE 26.- CONCLUDED.

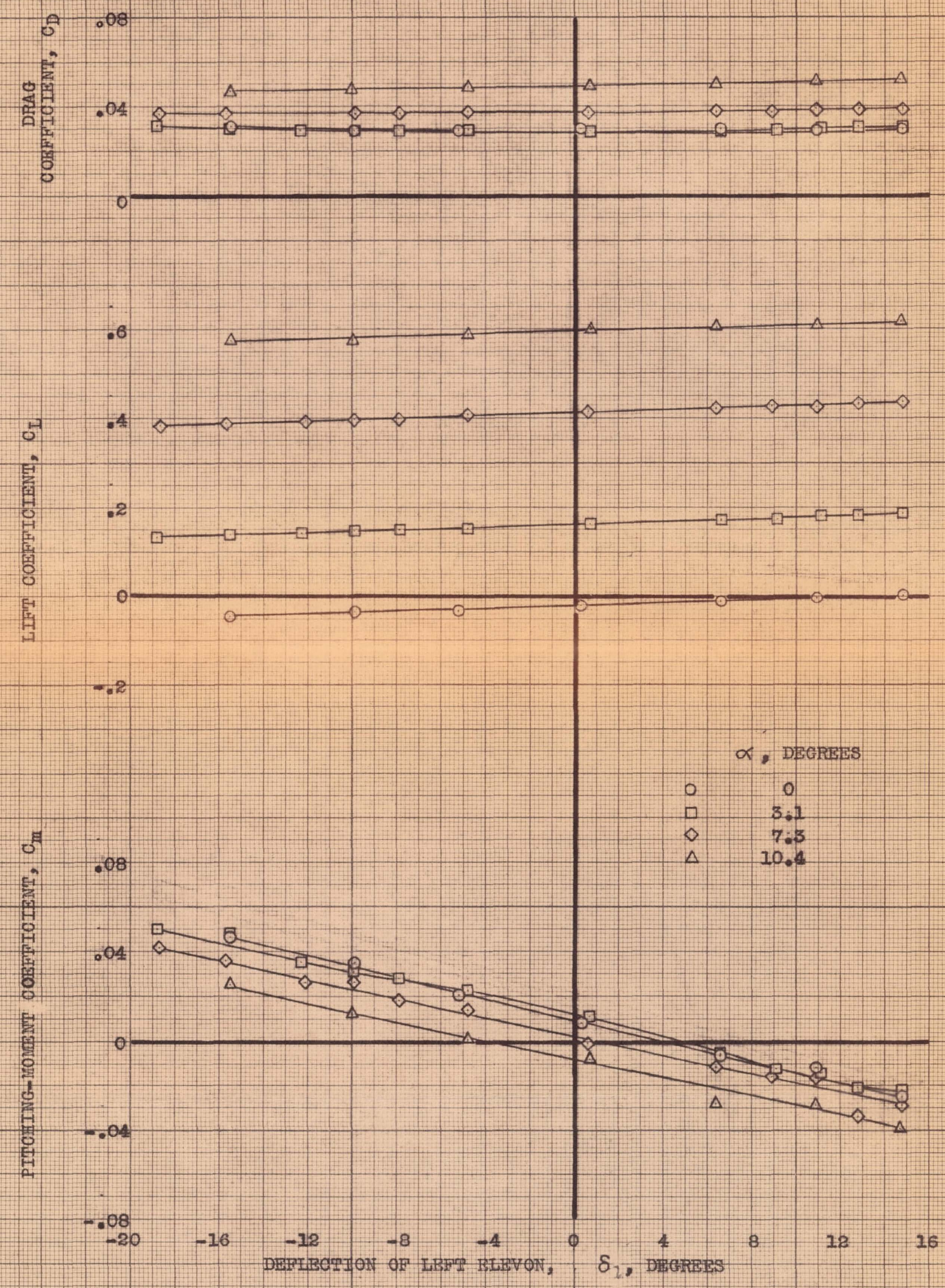

(a) C_D, C_L, C_m vs δ_l.

FIGURE 27.- VARIATION, WITH LEFT ELEVON DEFLECTION, OF THE AERODYNAMIC CHARACTERISTICS OF THE MISSILE AT SEVERAL ANGLES OF ATTACK. δ_r, 0°; R, 11 X 10^6; β, 7°.

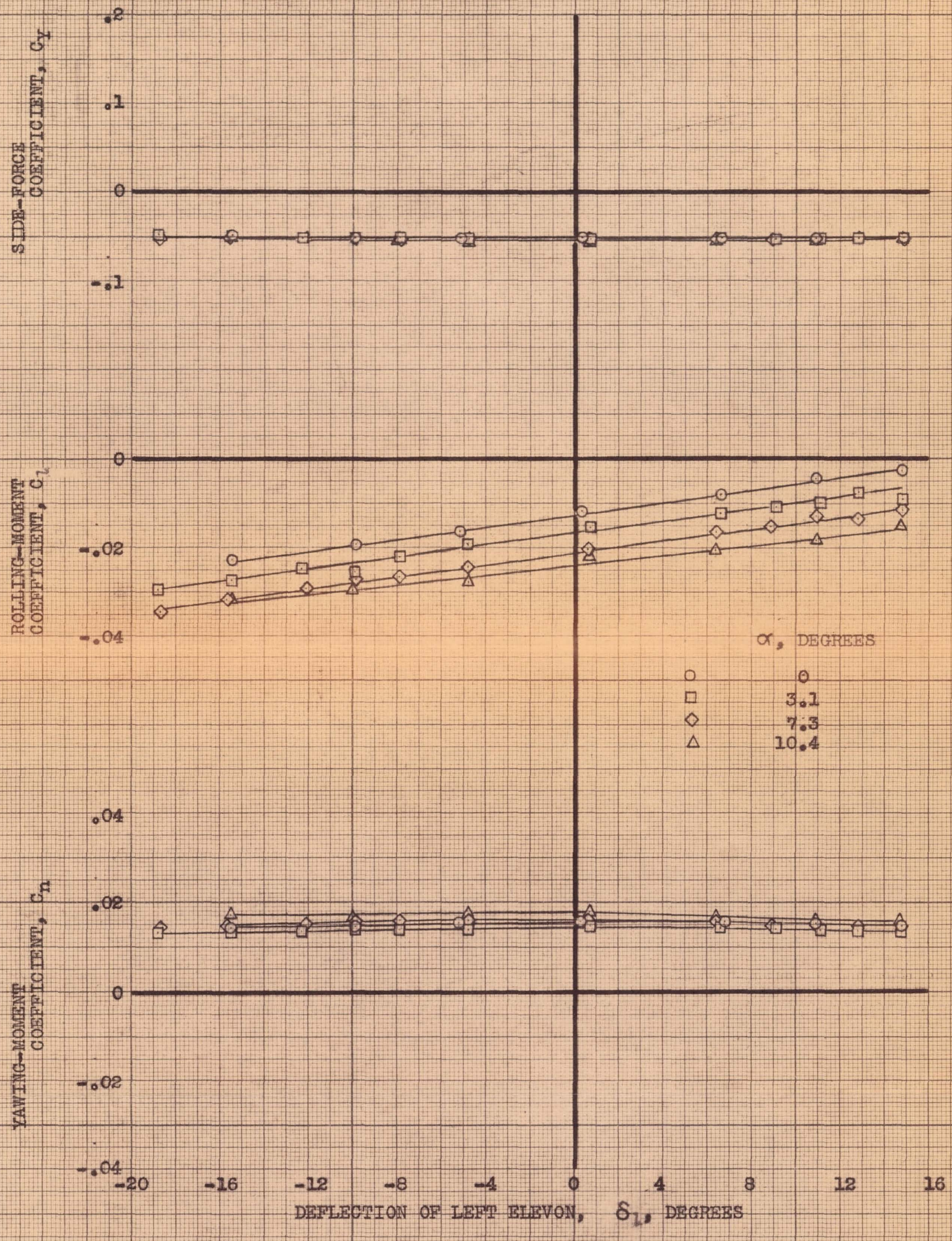

(b) C_Y, C_l, C_n vs δ_l.

FIGURE 27.- CONCLUDED.

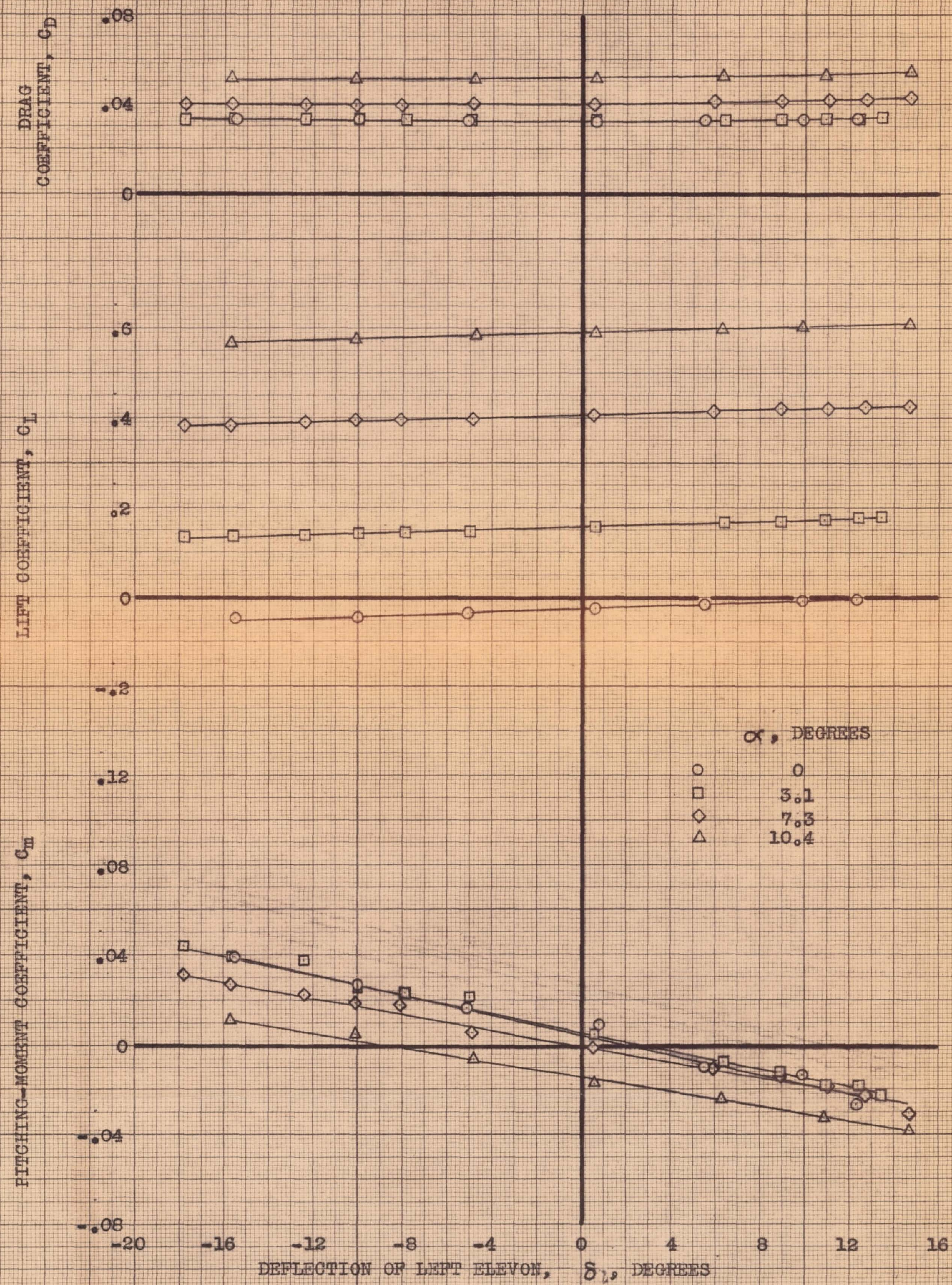

(a) C_D, C_L, C_m vs δ_l.

FIGURE 28.- VARIATION, WITH LEFT ELEVON DEFLECTION, OF THE AERODYNAMIC CHARACTERISTICS OF THE MISSILE AT SEVERAL ANGLES OF ATTACK. δ_r, 0°; R, 11 X 10^6; β, 10°.

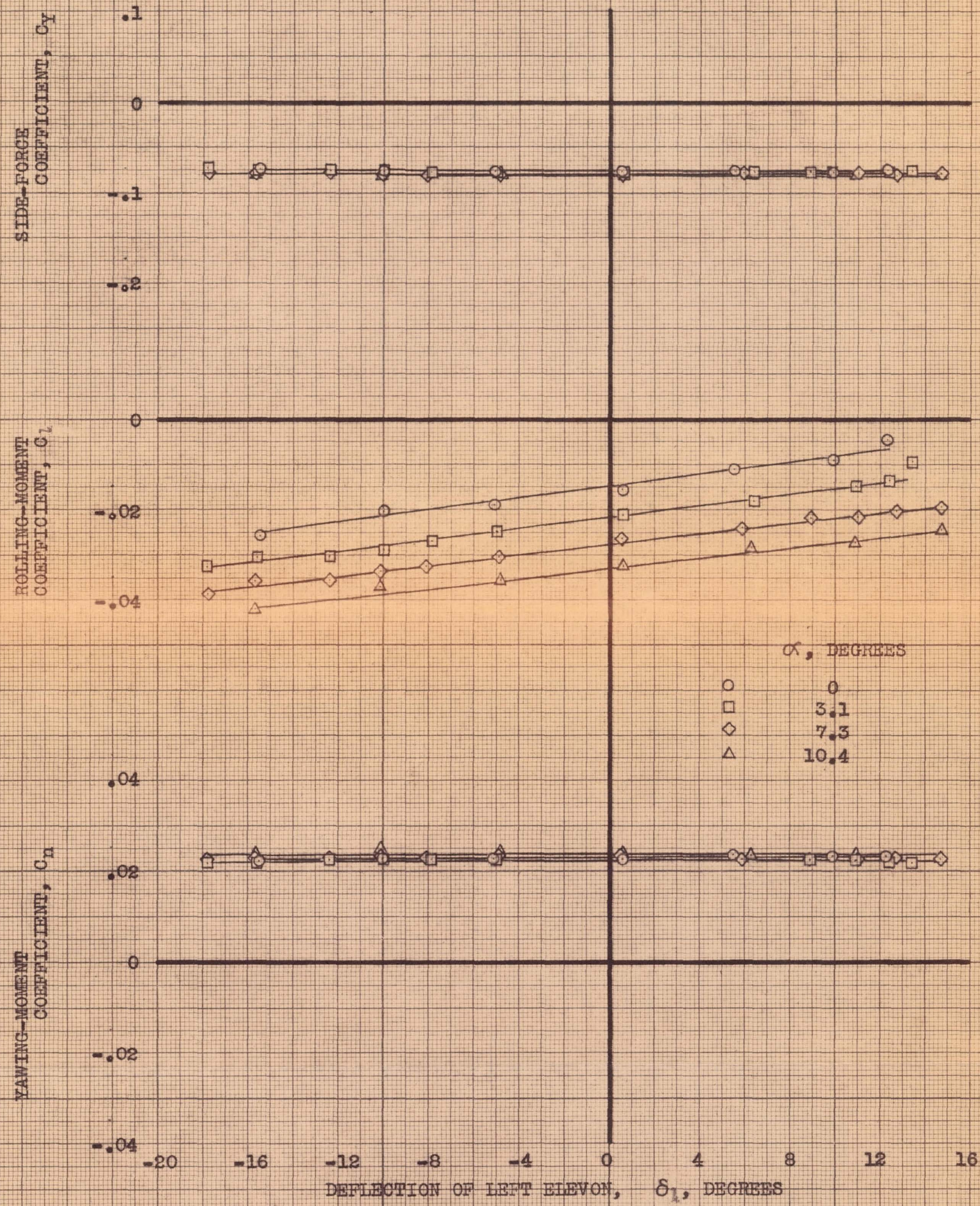

(b) C_Y, C_l, C_n vs δ_l.

FIGURE 28.- CONCLUDED.

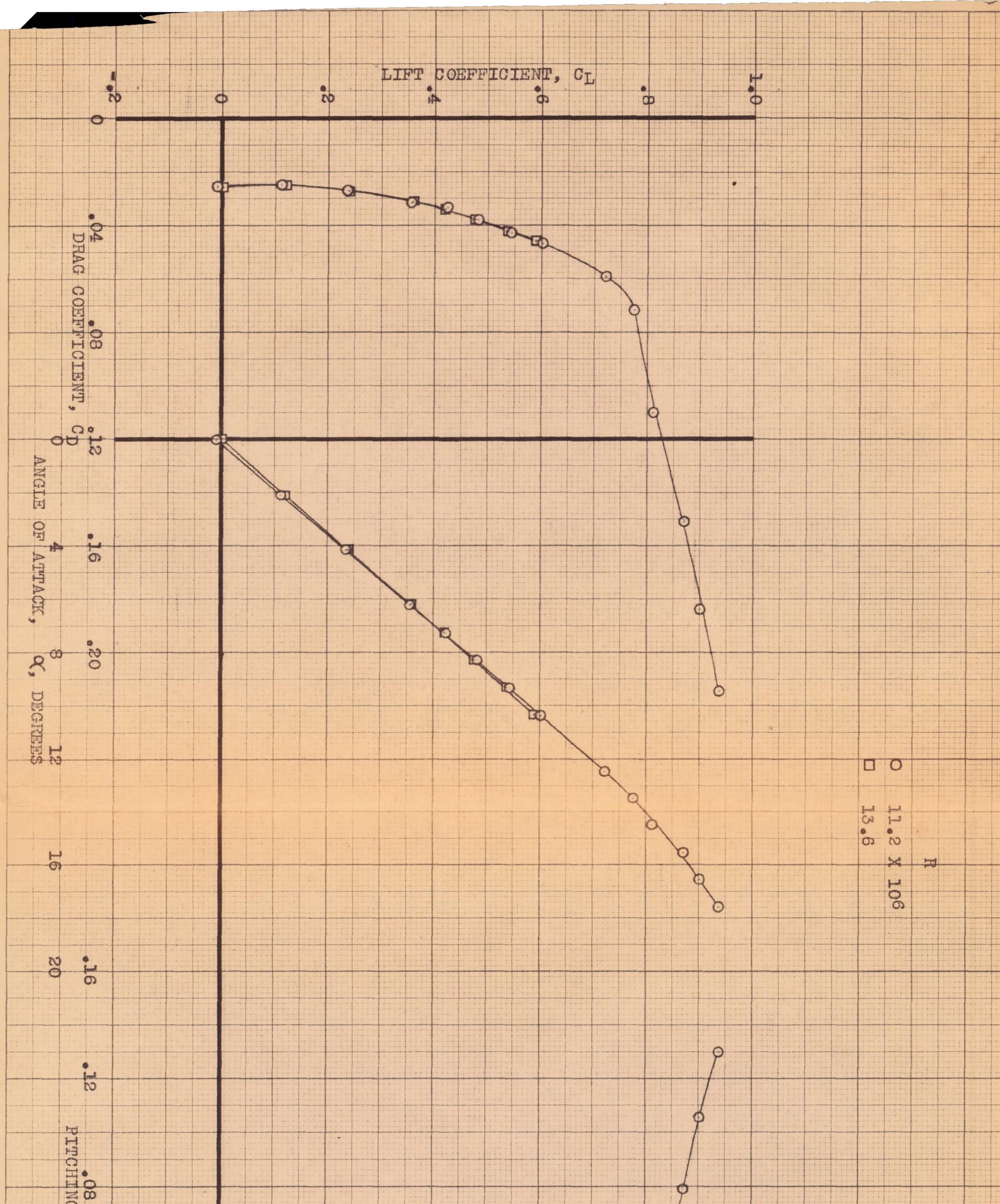

(a) δ_e, 0°.

FIGURE 29.- AERODYNAMIC CHARACTERISTICS IN PITCH OF THE MISSILE WITH DEFLECTION TARGET POSTS ON THE LEFT WING PANEL. TWO REYNOLDS NUMBERS; β, 0°.

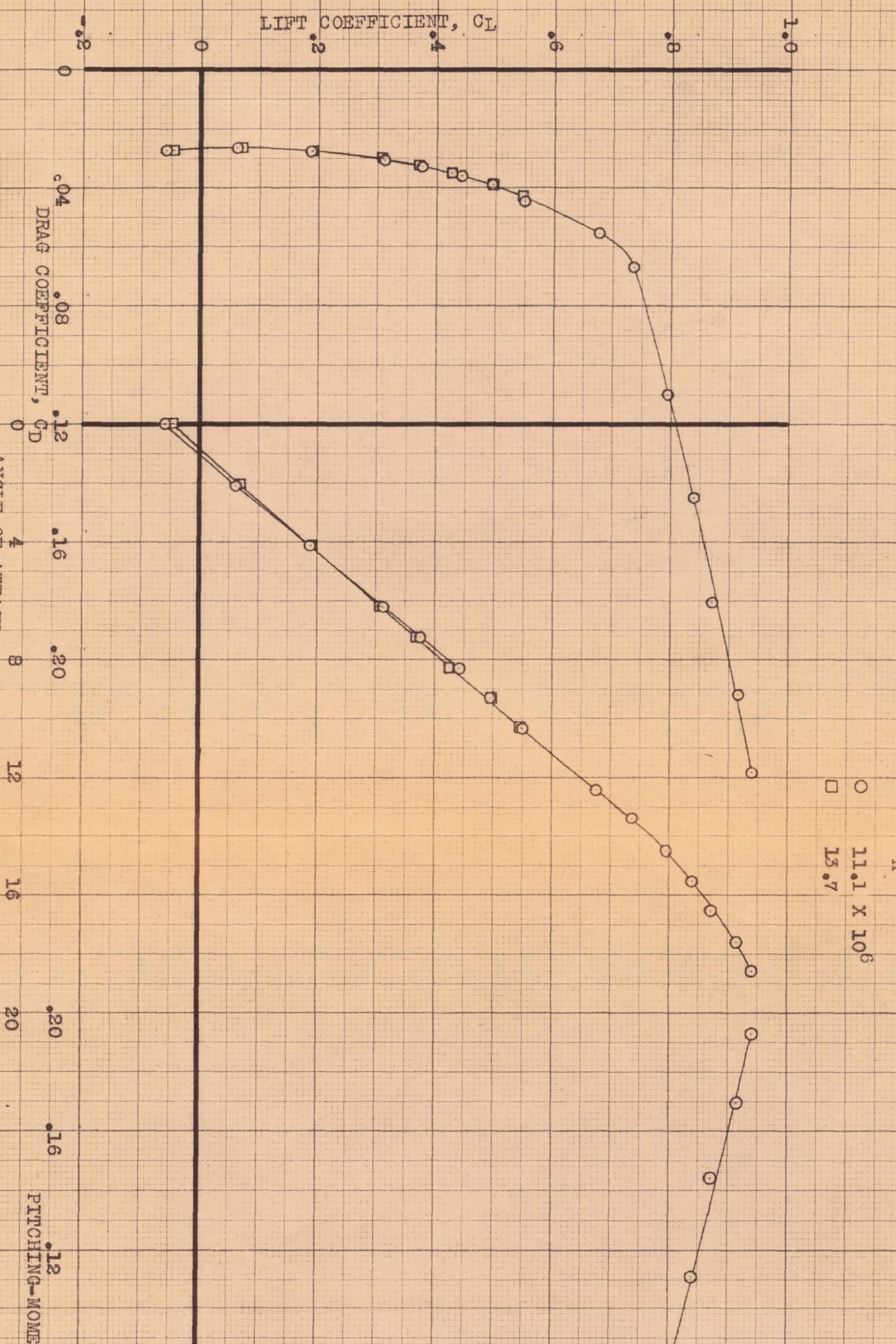

(b) δ_e, -10°.

FIGURE 29.- CONTINUED.

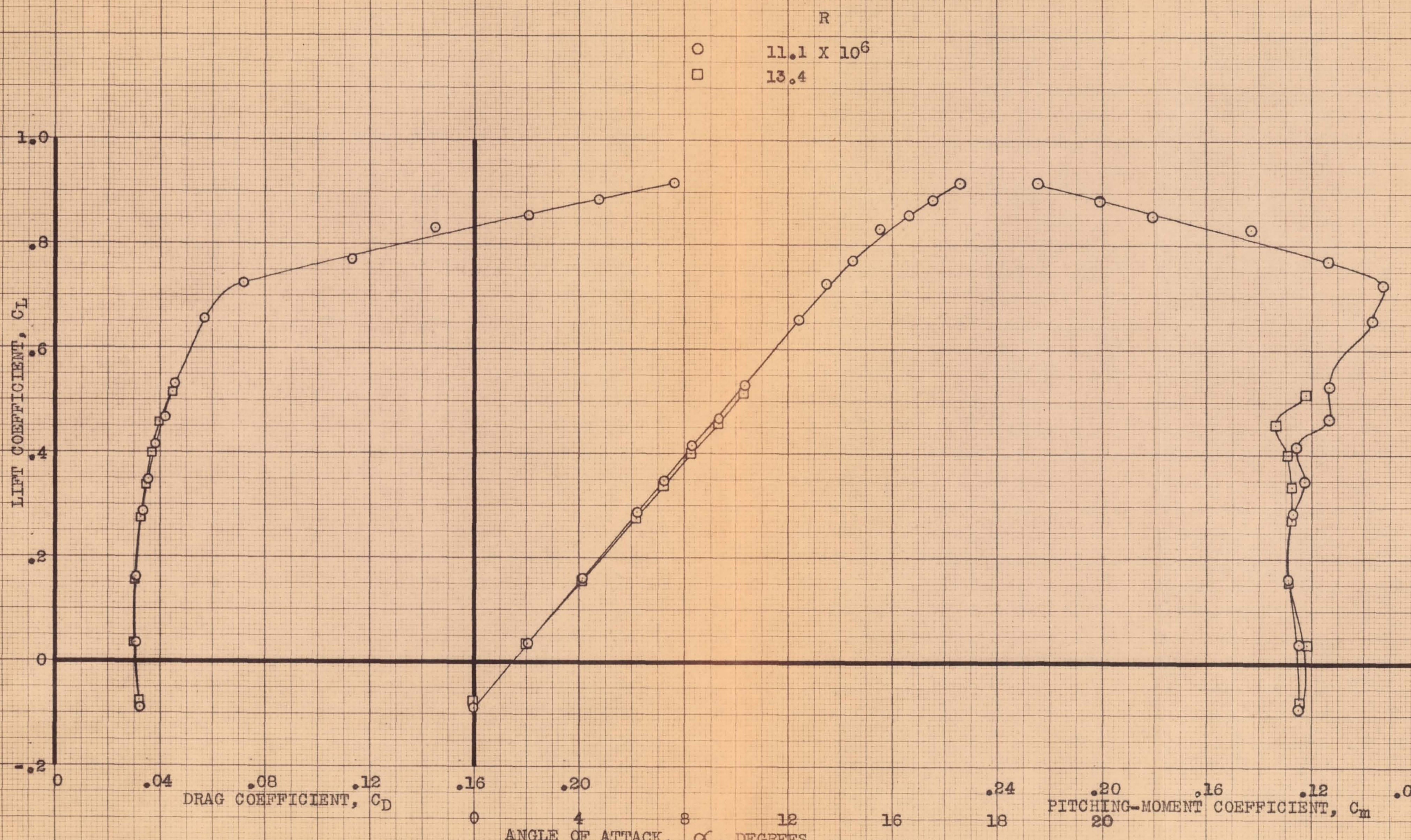

(c) δ_e, -18°.

FIGURE 29.- CONCLUDED.

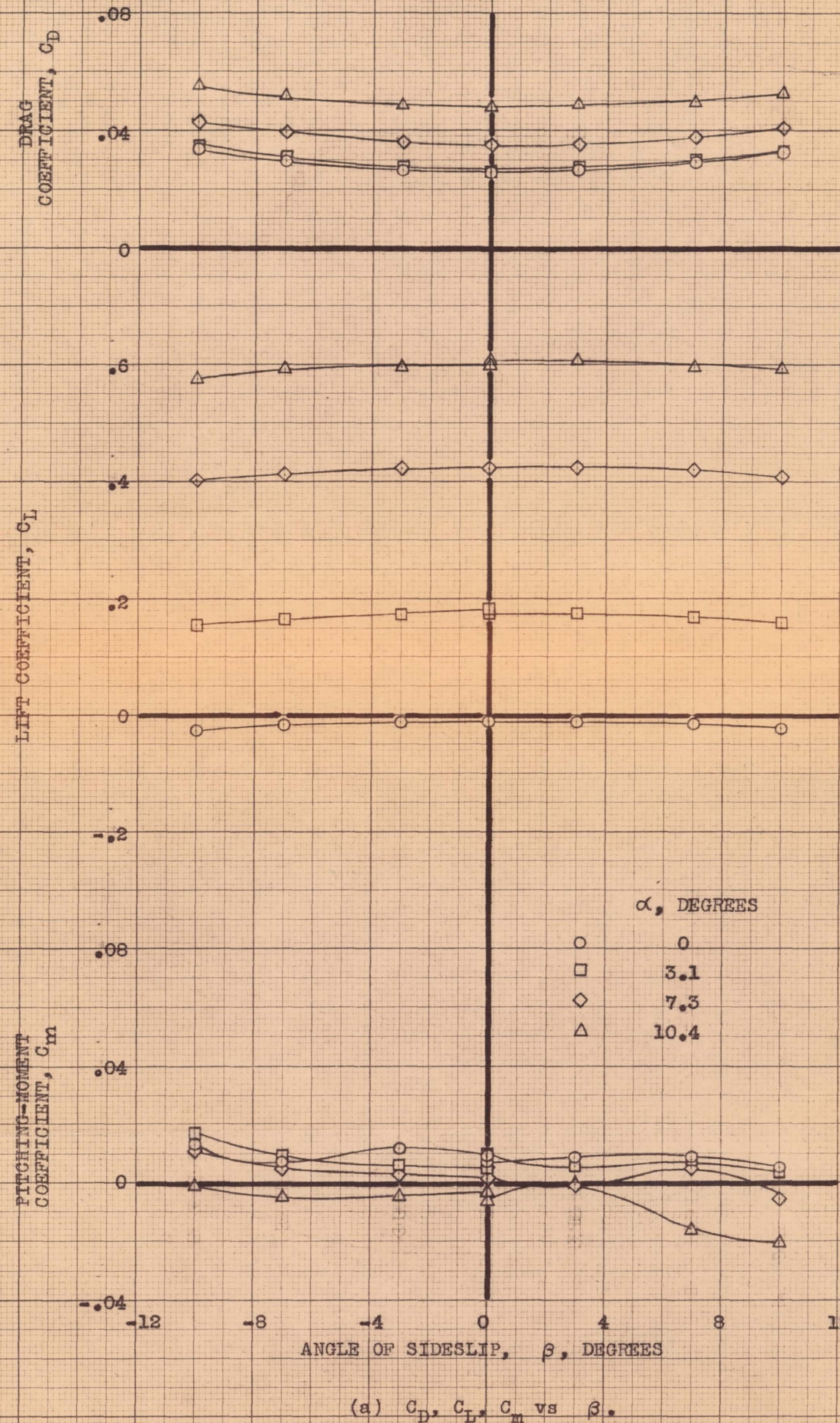

(a) C_D, C_L, C_m vs β.

FIGURE 30.- AERODYNAMIC CHARACTERISTICS IN SIDESLIP OF THE MISSILE AT SEVERAL ANGLES OF ATTACK WITH DEFLECTION TARGET POSTS ON THE LEFT PANEL. δ_e, 0°; R, 11 X 10⁶.

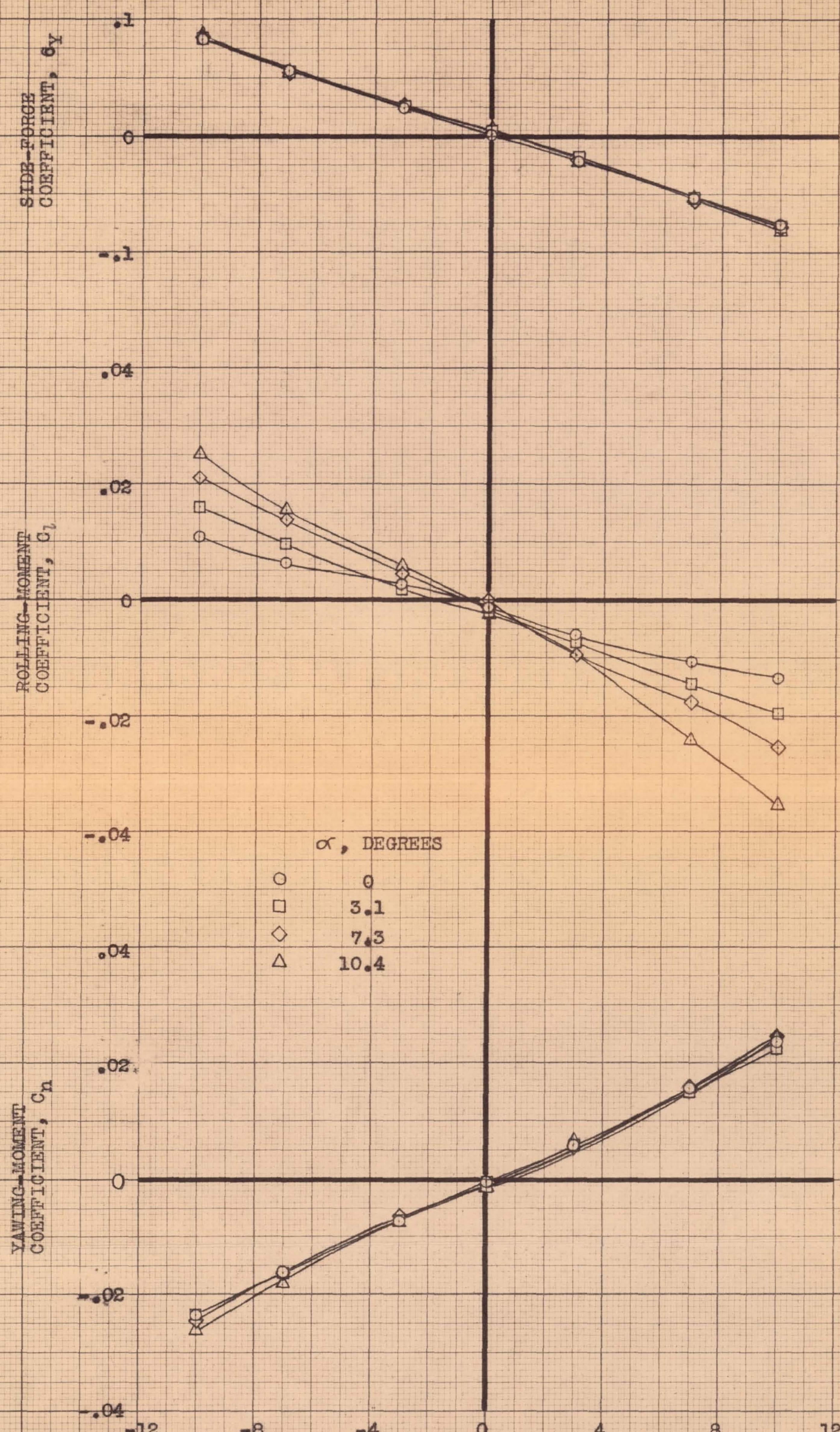

(b) C_Y, C_l, C_n vs β.

FIGURE 30.- CONCLUDED.

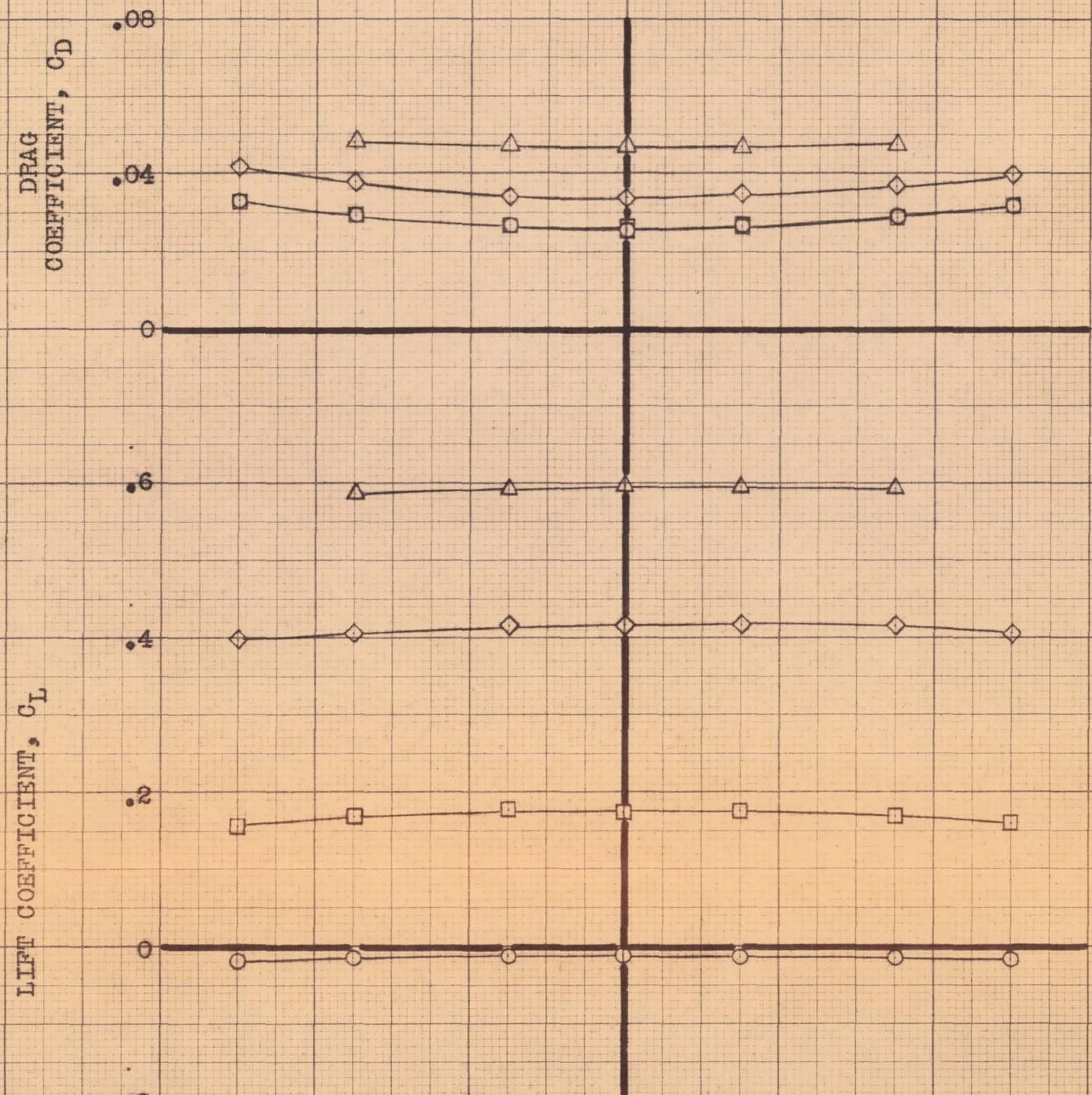

(a) C_D, C_L, C_m vs β.

FIGURE 31.- AERODYNAMIC CHARACTERISTICS IN SIDESLIP OF THE MISSILE AT SEVERAL ANGLES OF ATTACK WITH DEFLECTION TARGET POSTS ON THE LEFT WING PANEL. δ_e, 0°; R, 12.5×10^6.

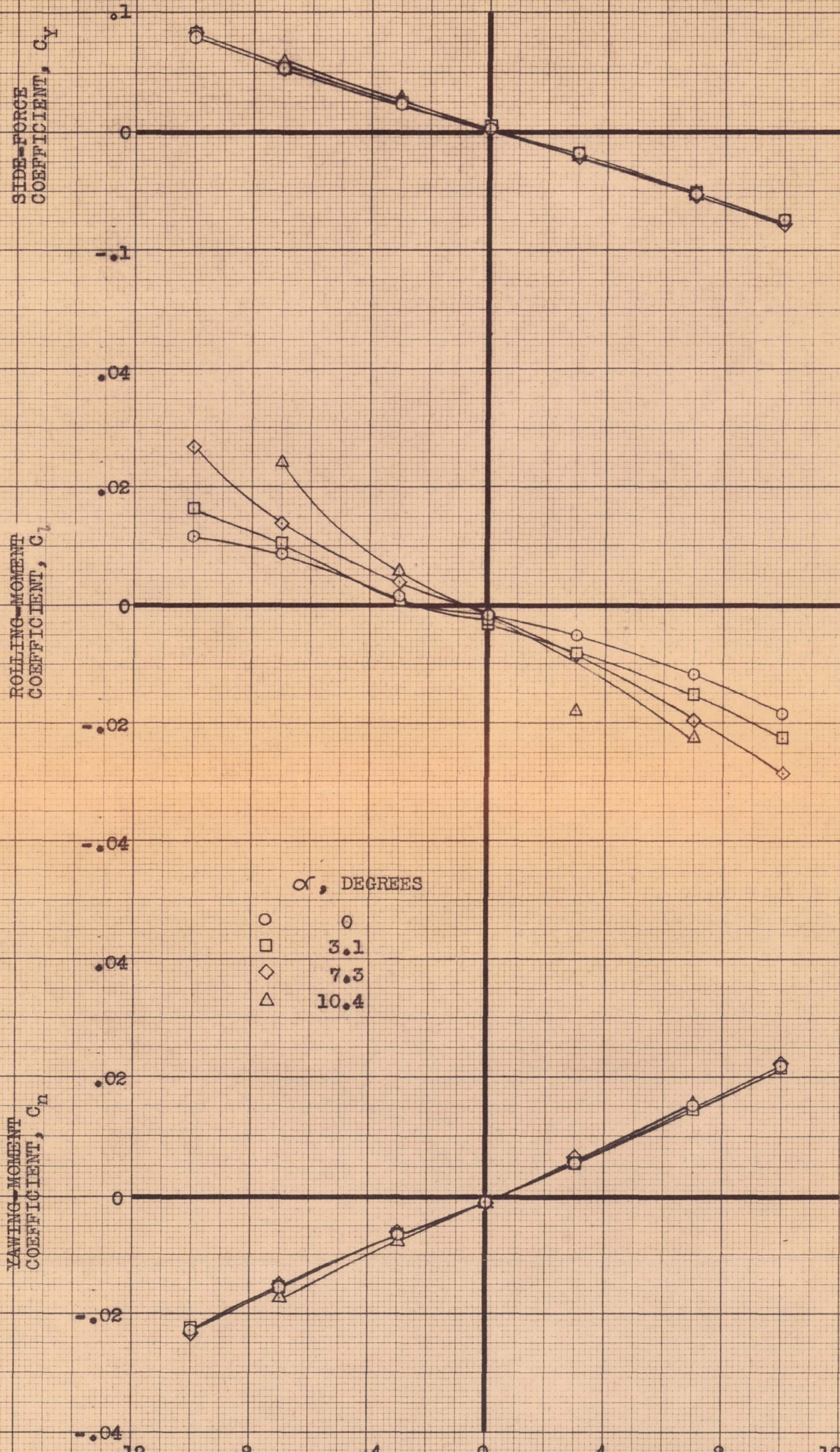

(b) C_Y, C_l, C_n vs β.

FIGURE 31.- CONCLUDED.

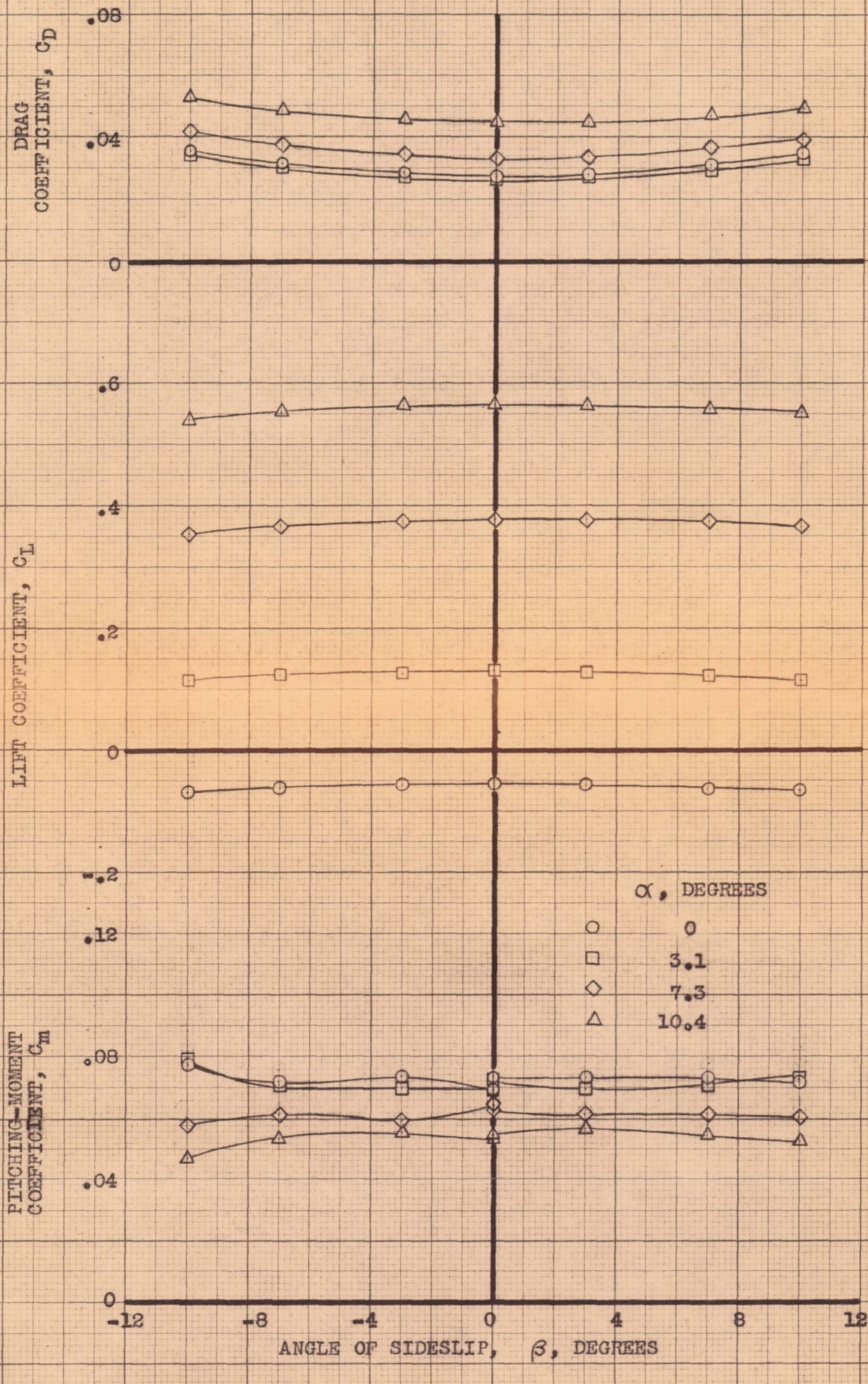

(a) C_D, C_L, C_m vs β.

FIGURE 32.- AERODYNAMIC CHARACTERISTICS IN SIDESLIP OF THE MISSILE AT SEVERAL ~~ANGLES OF ATTACK WITH DEFLECTION TARGET POSTS ON THE LEFT WING PANEL.~~ δ_e, -10°; R, 11×10^6.

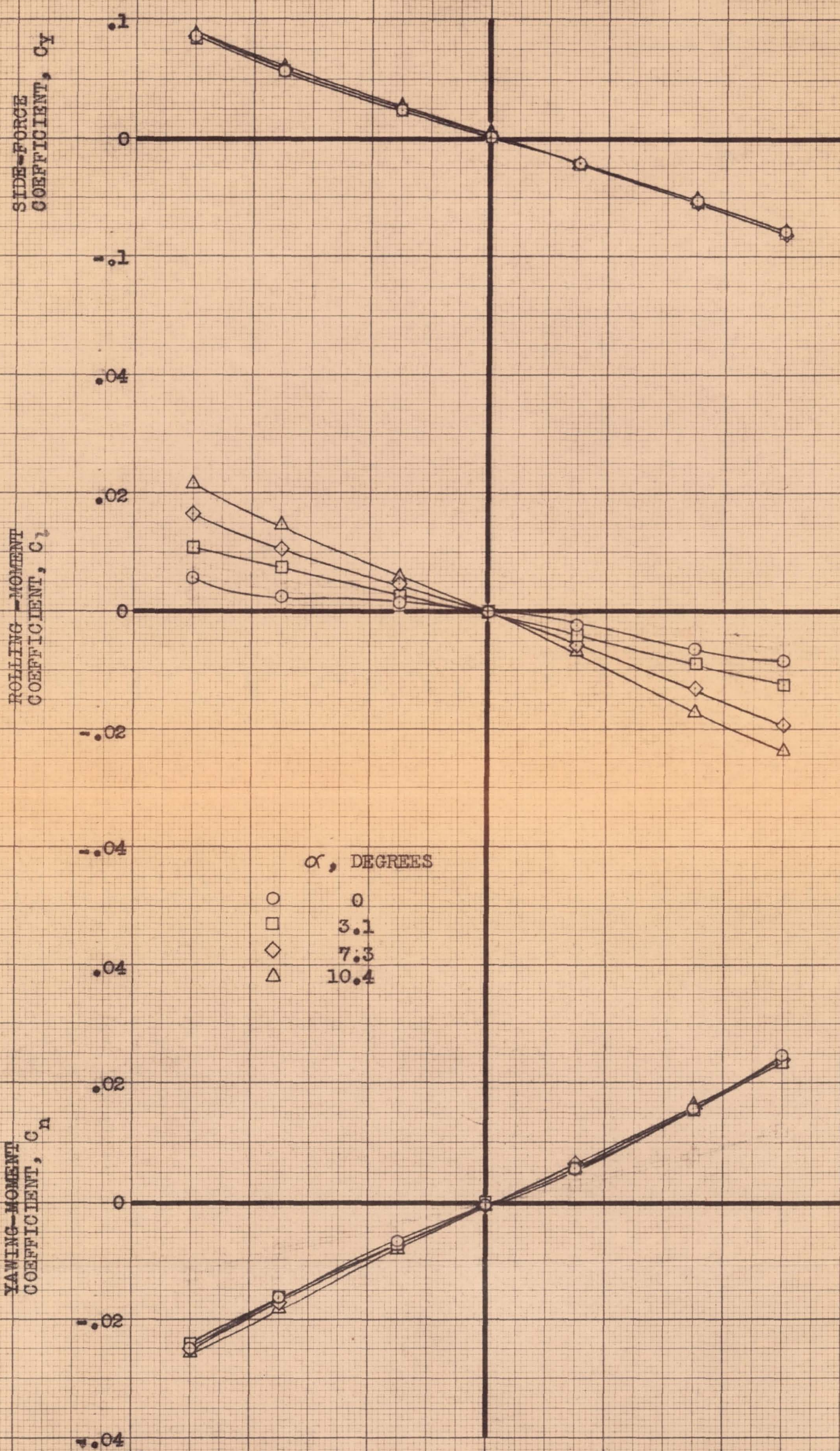

(b) C_Y, C_l, C_n vs β.

FIGURE 32.- CONCLUDED.

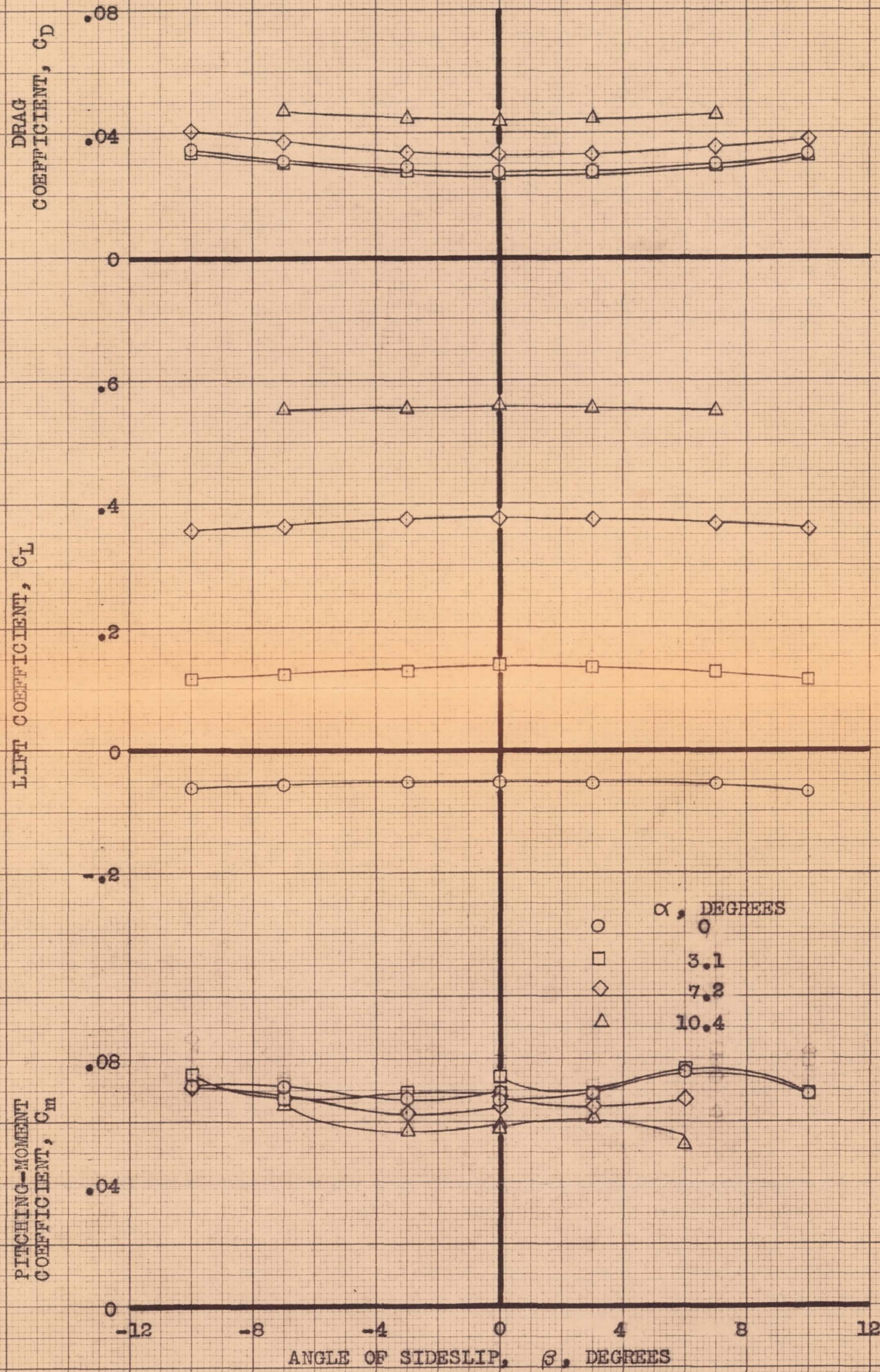

(a) C_D, C_L, C_m vs β.

FIGURE 33.- AERODYNAMIC CHARACTERISTICS IN SIDESLIP OF THE MISSILE AT SEVERAL ANGLES OF ATTACK WITH DEFLECTION TARGET POSTS ON THE LEFT WING PANEL. δ_e, -10°; R, 12.5×10^6.

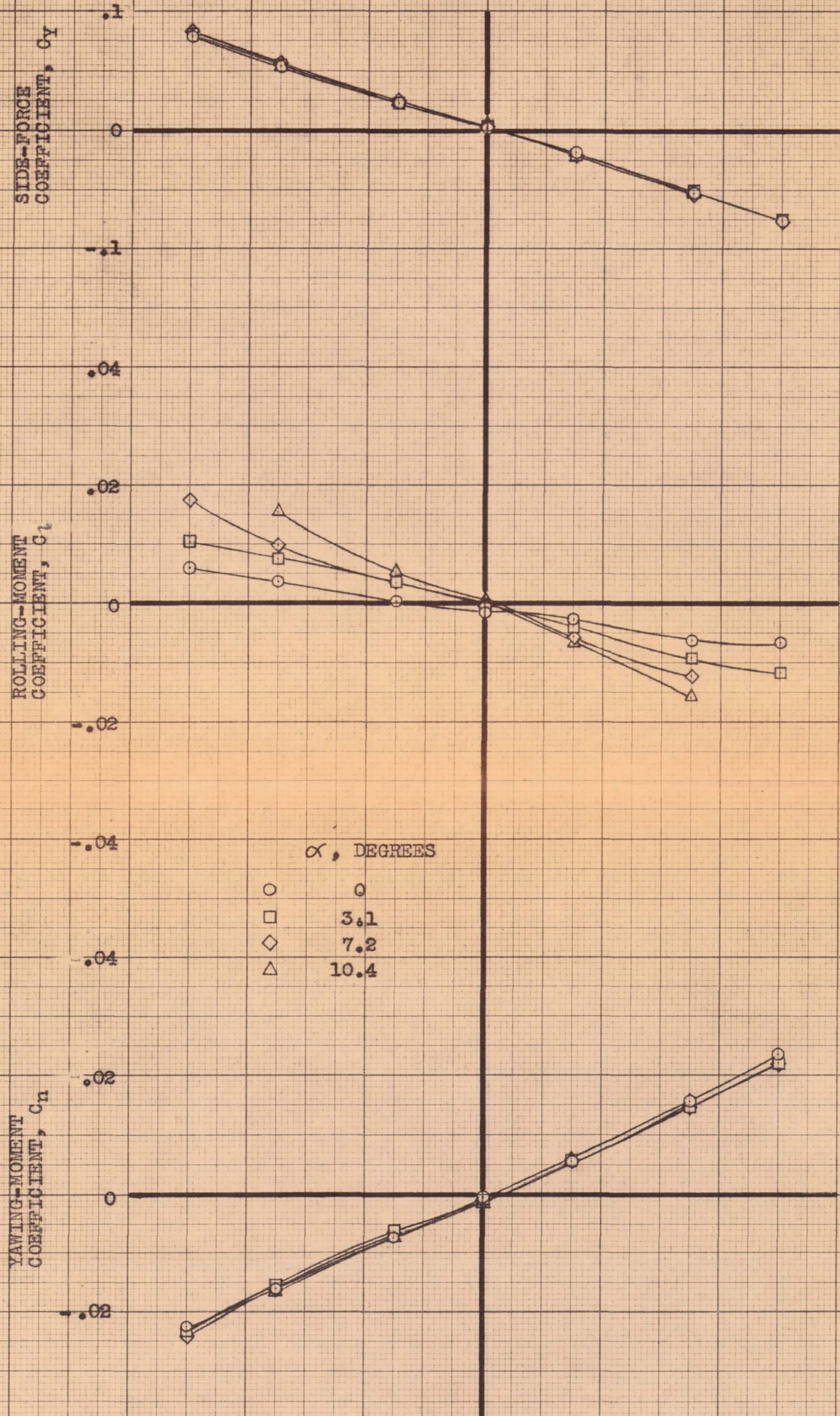

(b) C_Y, C_l, C_n vs β.

FIGURE 33.- CONCLUDED.

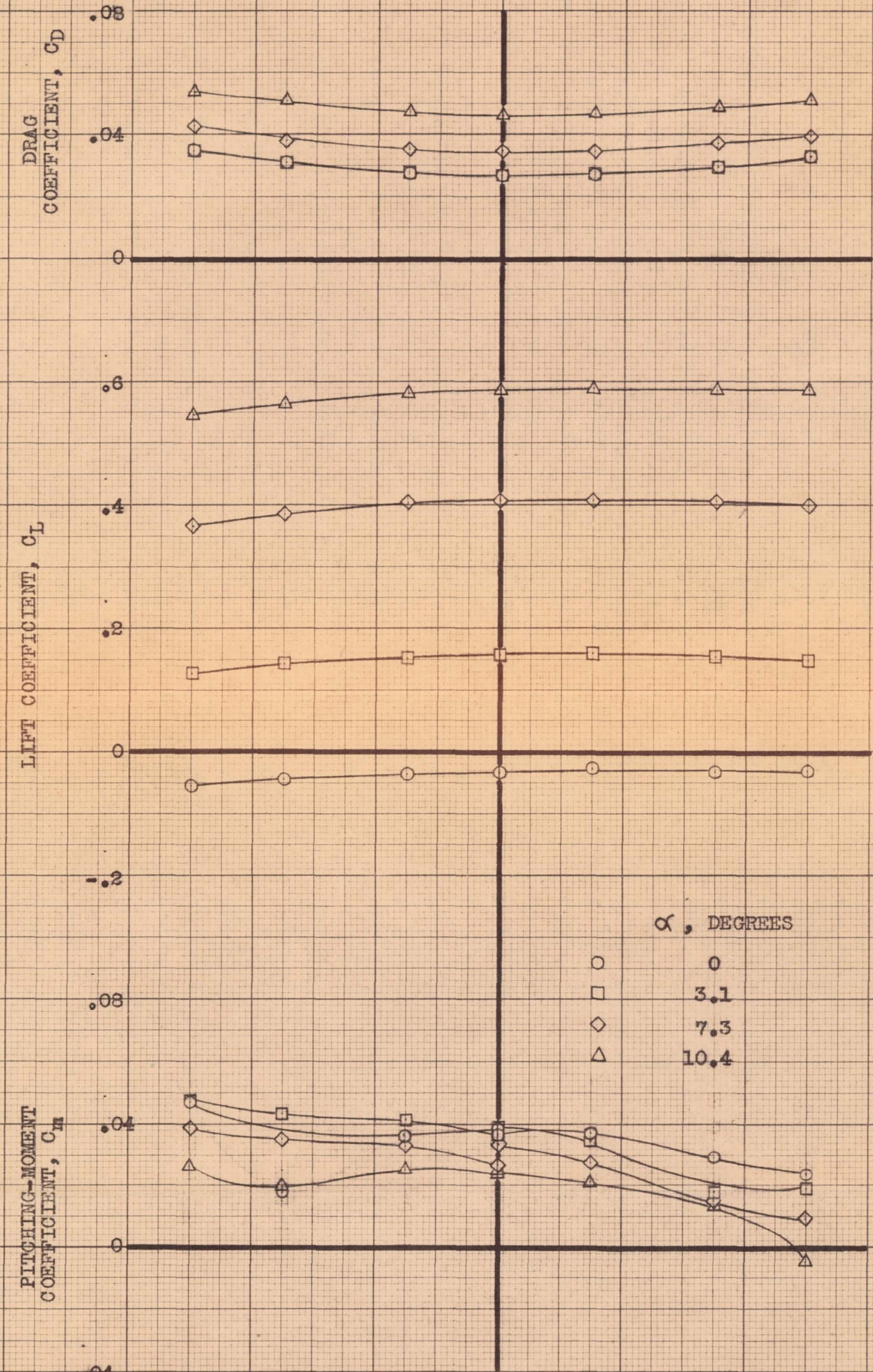

(a) C_D, C_L, C_m vs β.

FIGURE 34.- AERODYNAMIC CHARACTERISTICS IN SIDESLIP OF THE MISSILE AT SEVERAL ANGLES OF ATTACK WITH DEFLECTION TARGET POSTS ON THE LEFT WING PANEL. δ_r, 0°; δ_l, -10°; R, 11 X 10^6.

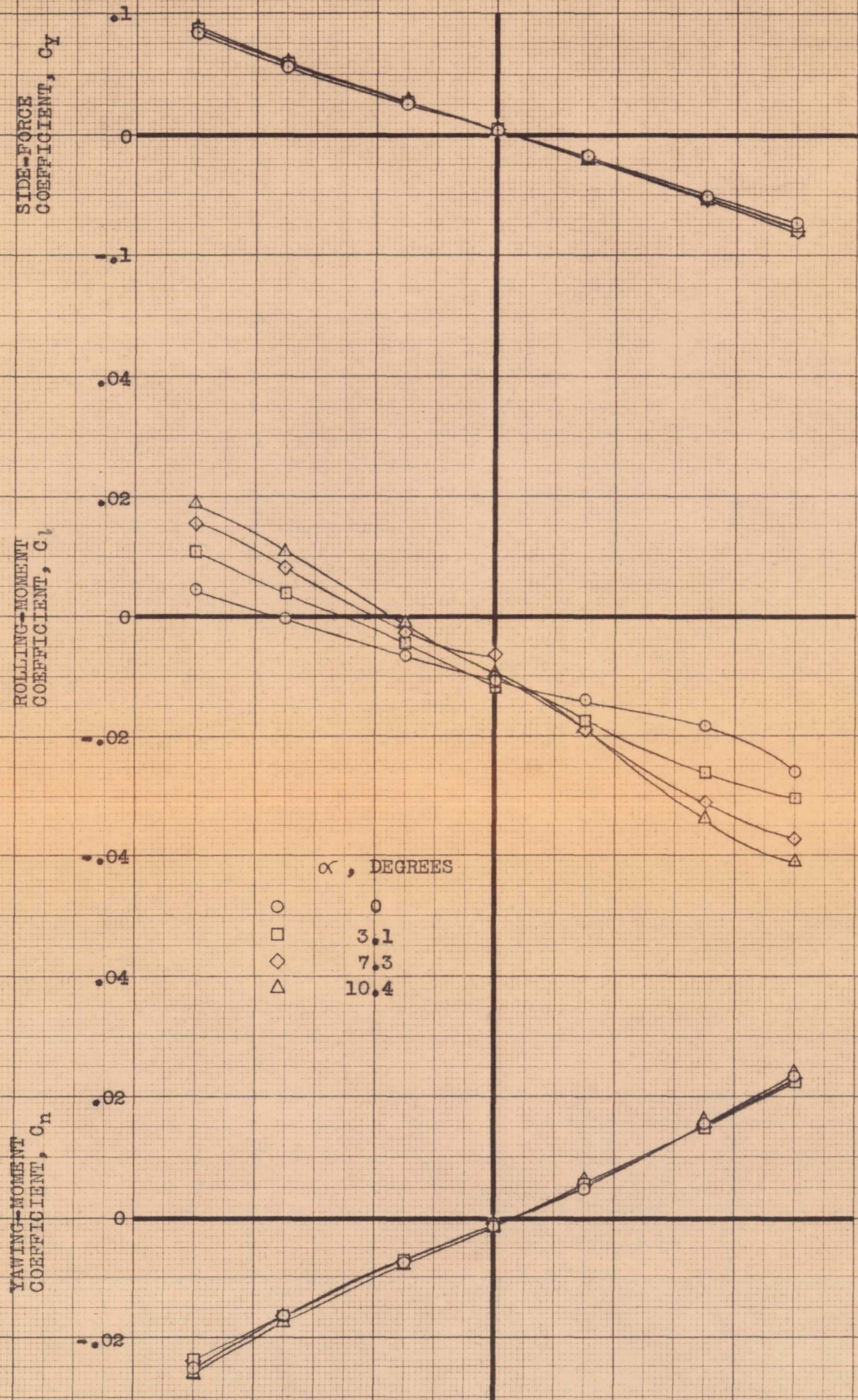

(b) C_Y, C_l, C_n vs β.

FIGURE 34.- CONCLUDED.

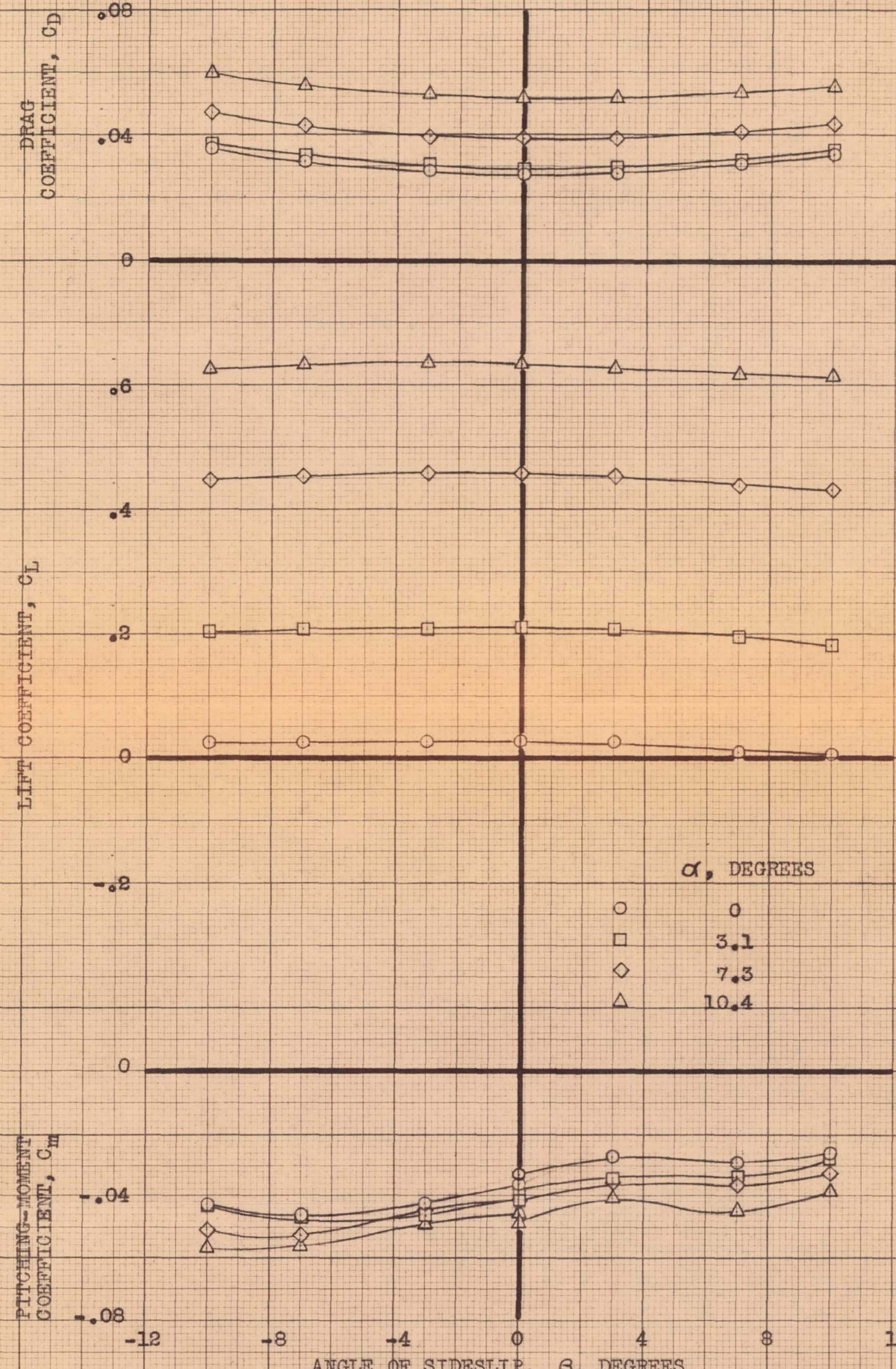

(a) C_D, C_L, C_m vs β.

FIGURE 35.- AERODYNAMIC CHARACTERISTICS IN SIDESLIP OF THE MISSILE AT SEVERAL ANGLES OF ATTACK WITH DEFLECTION TARGET POSTS ON THE LEFT WING PANEL. δ_r, 0°; δ_l, 15°; R, 11 X 10^6.

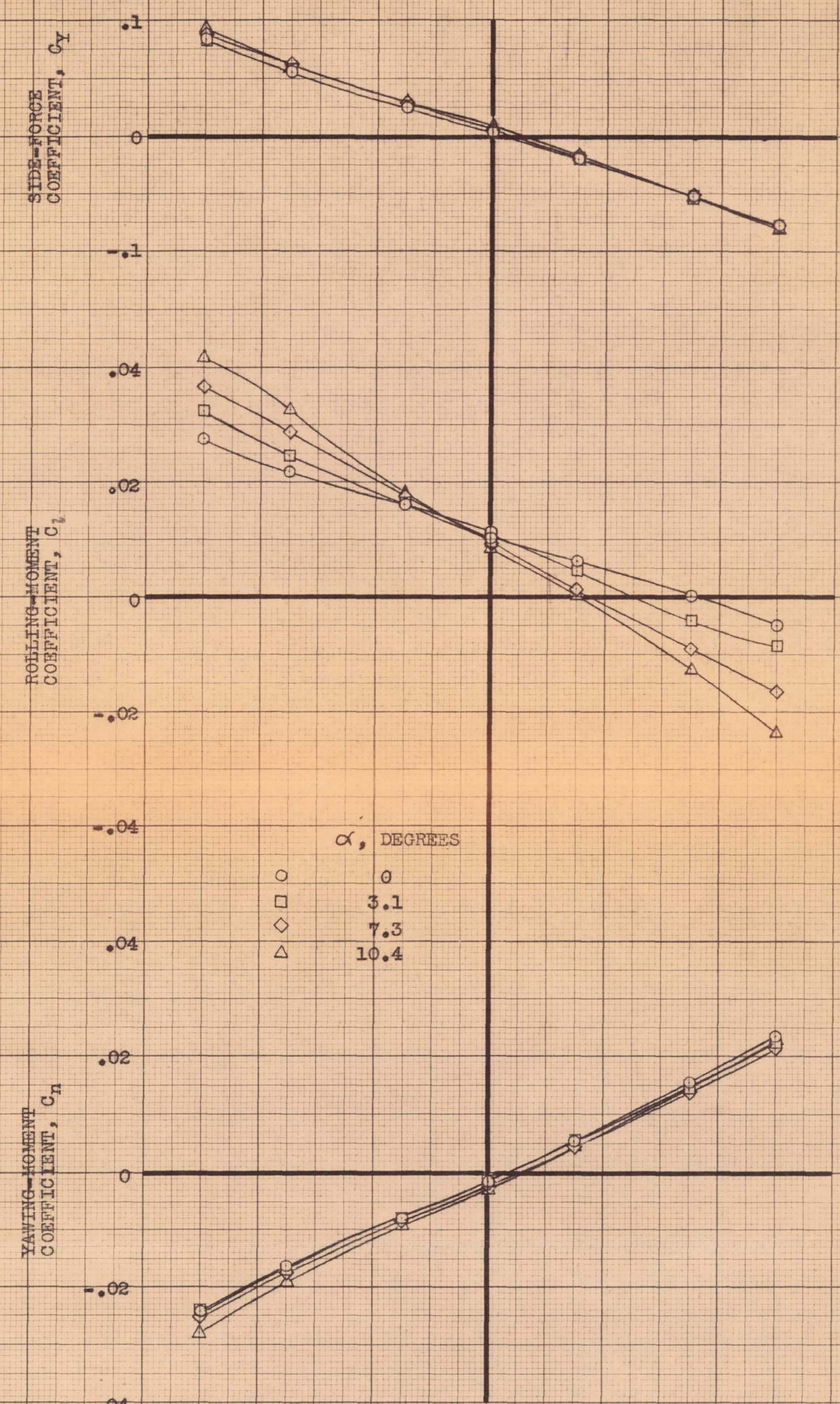

(b) C_Y, C_l, C_n vs β.

FIGURE 35.- CONCLUDED.

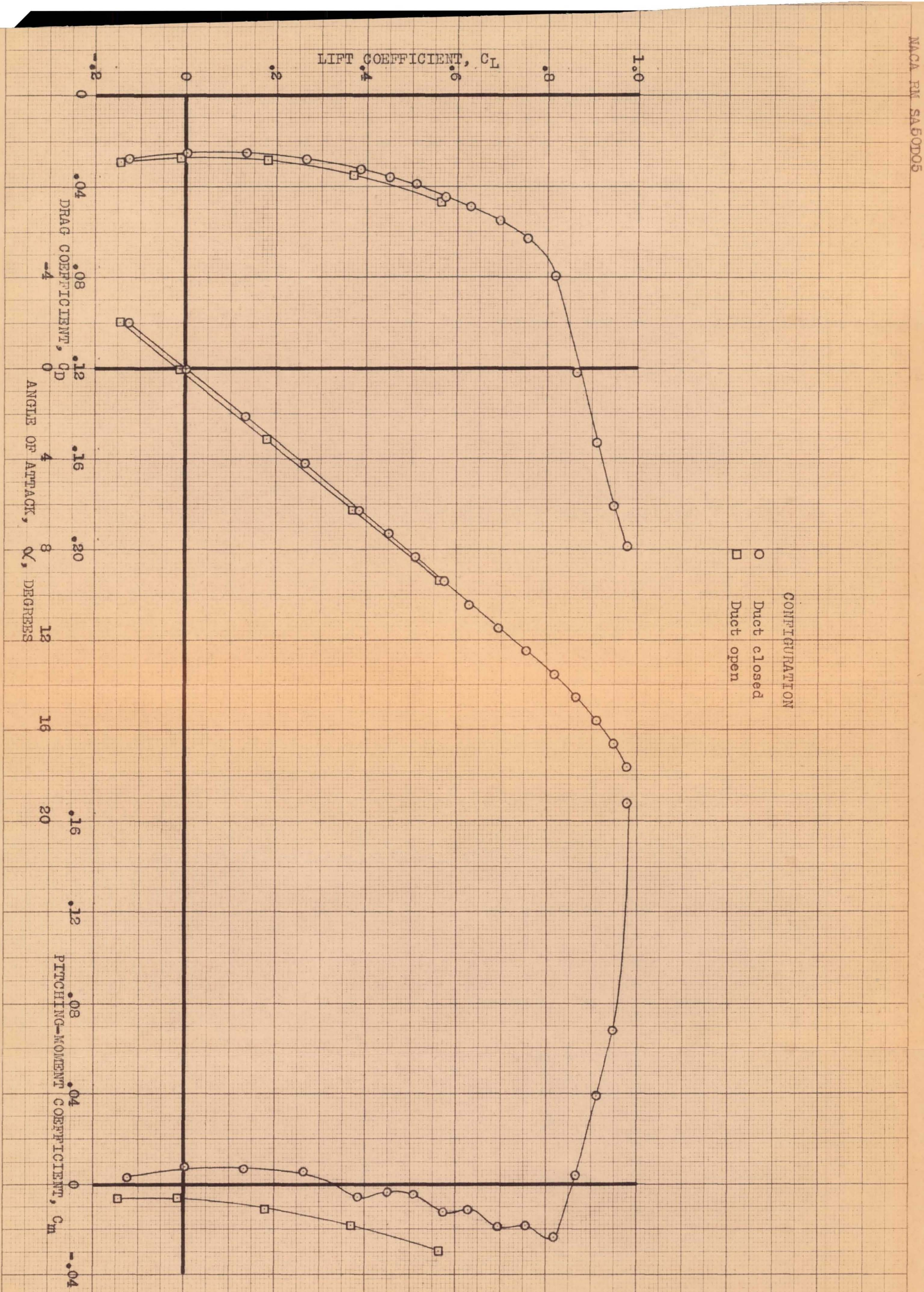

FIGURE 36.- COMPARISON OF THE AERODYNAMIC CHARACTERISTICS IN PITCH OF THE MISSILE WITH DUCT OPEN AND CLOSED. β, 0°; δ_e, 0°; R, 2 X 10^6.

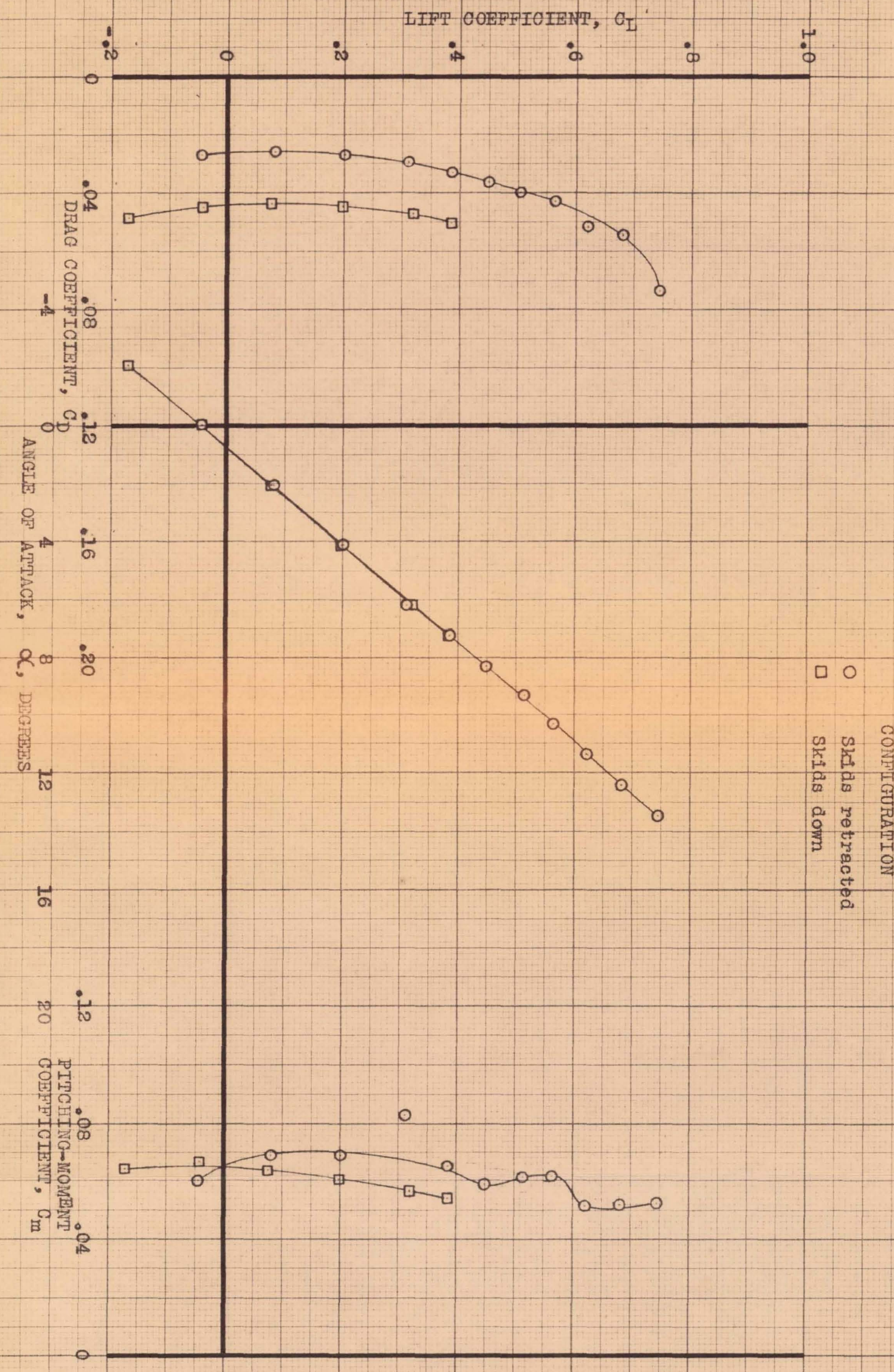

FIGURE 37.- EFFECT OF THE LANDING SKIDS ON THE AERODYNAMIC CHARACTERISTICS OF THE MISSILE IN PITCH. β, 0°; δ_e, -10°; R, 13.4×10^6.

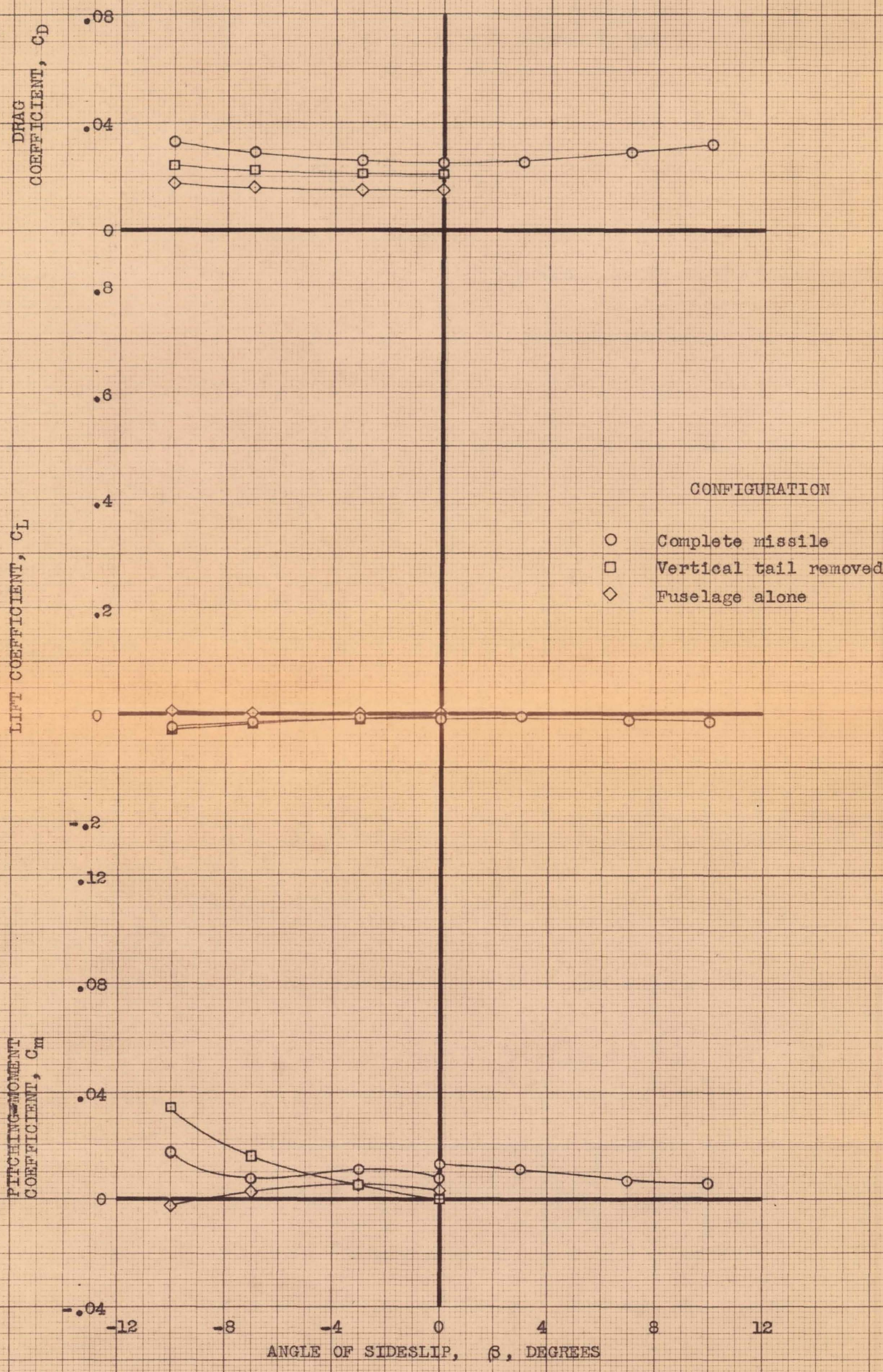

(a) C_D, C_L, C_m vs β.

FIGURE 38.- COMPARISON OF THE AERODYNAMIC CHARACTERISTICS IN SIDESLIP OF THE COMPLETE MISSILE WITH THE CHARACTERISTICS OF THE MISSILE WITH THE VERTICAL TAIL REMOVED, AND WITH THE FUSELAGE ALONE. R, 11 X 10^6; δ_e, 0°; α, 0°.

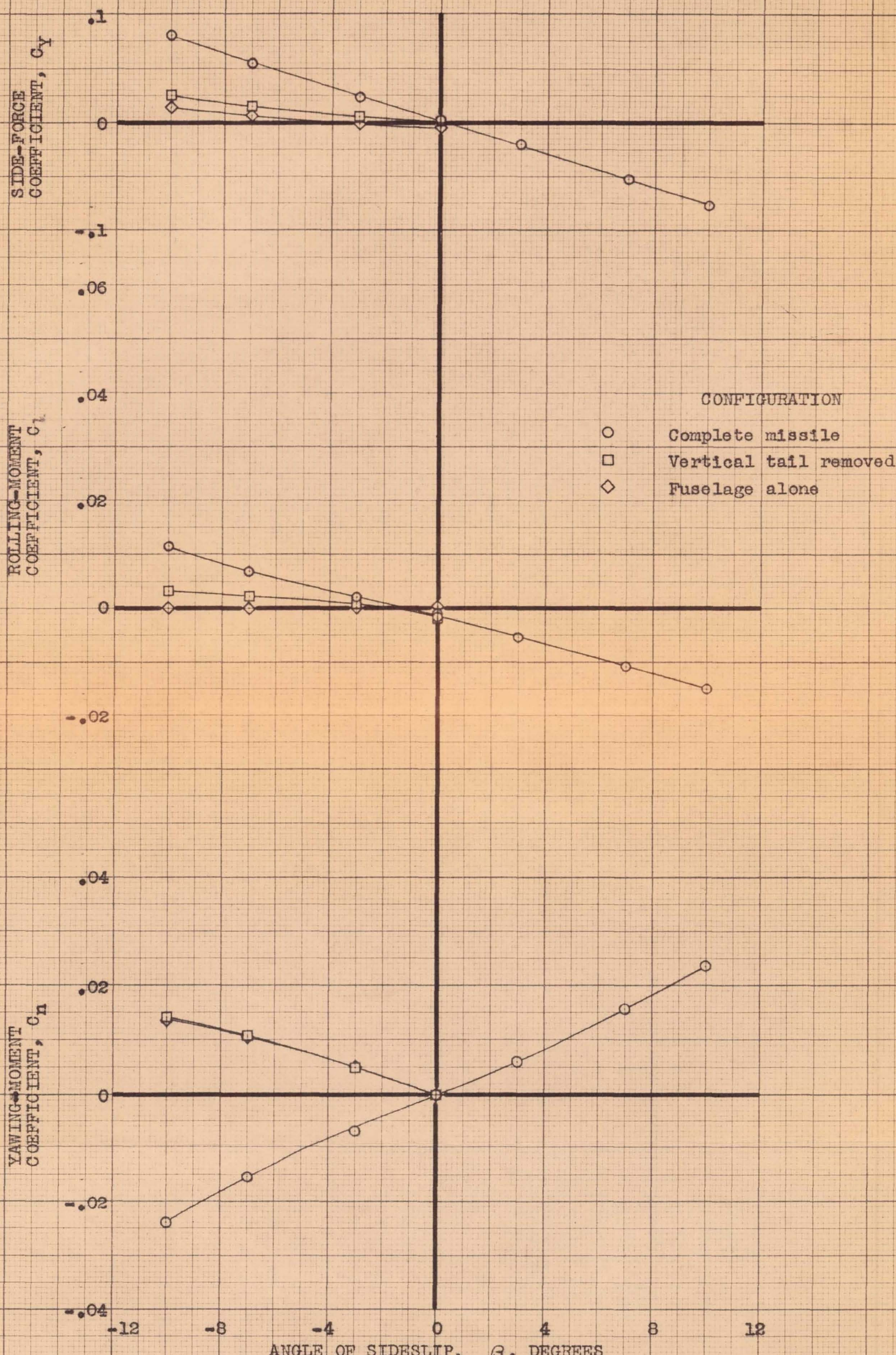

(b) C_Y, C_l, C_n vs β.

FIGURE 38.- CONCLUDED.

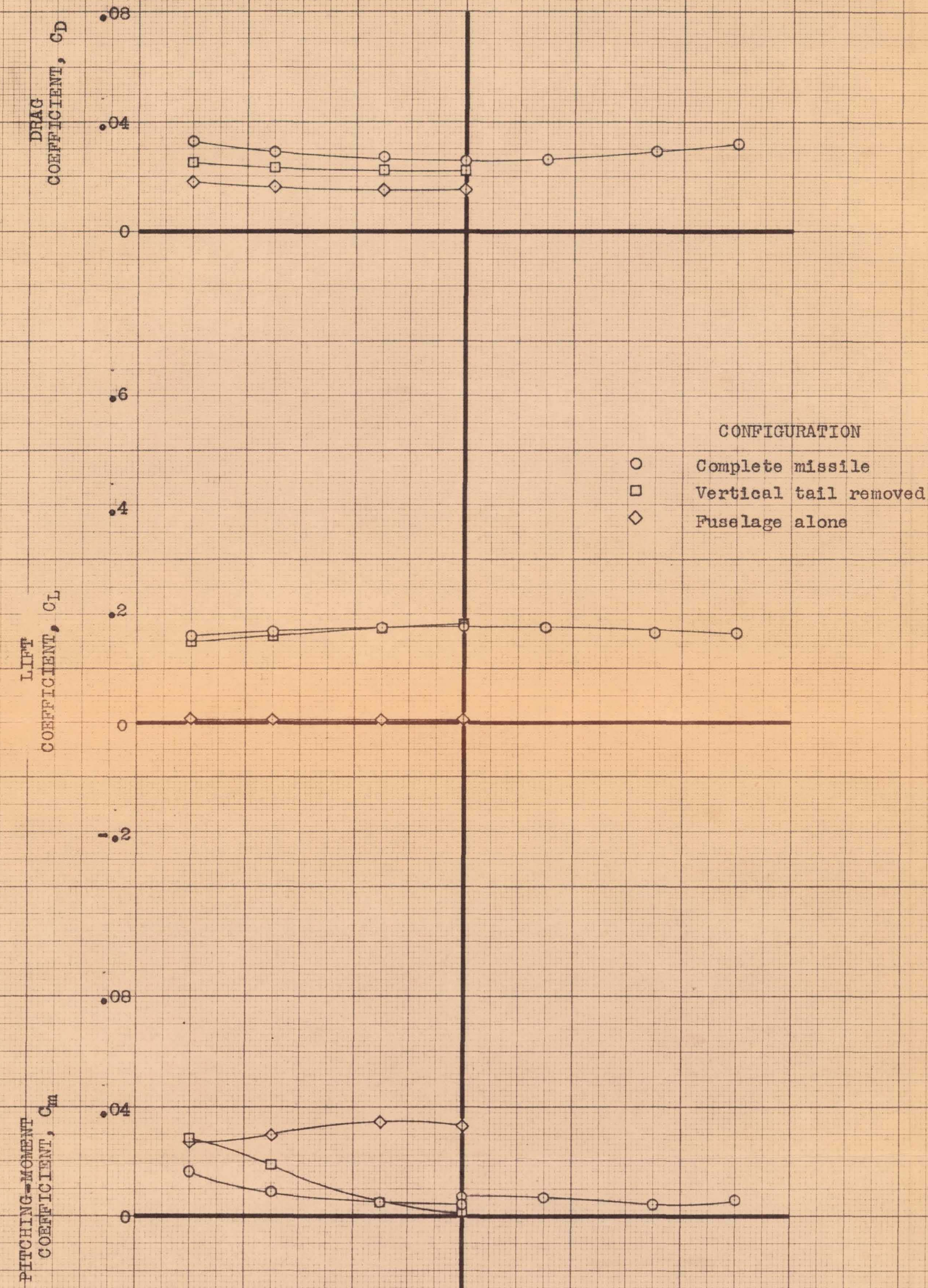

(a) C_D, C_L, C_m vs β.

FIGURE 39.- COMPARISON OF THE AERODYNAMIC CHARACTERISTICS IN SIDESLIP OF THE COMPLETE MISSILE WITH THE CHARACTERISTICS OF THE MISSILE WITH THE VERTICAL TAIL REMOVED, AND WITH THE FUSELAGE ALONE. R, 11 X 10^6; δ_e, 0°; α, 3°.

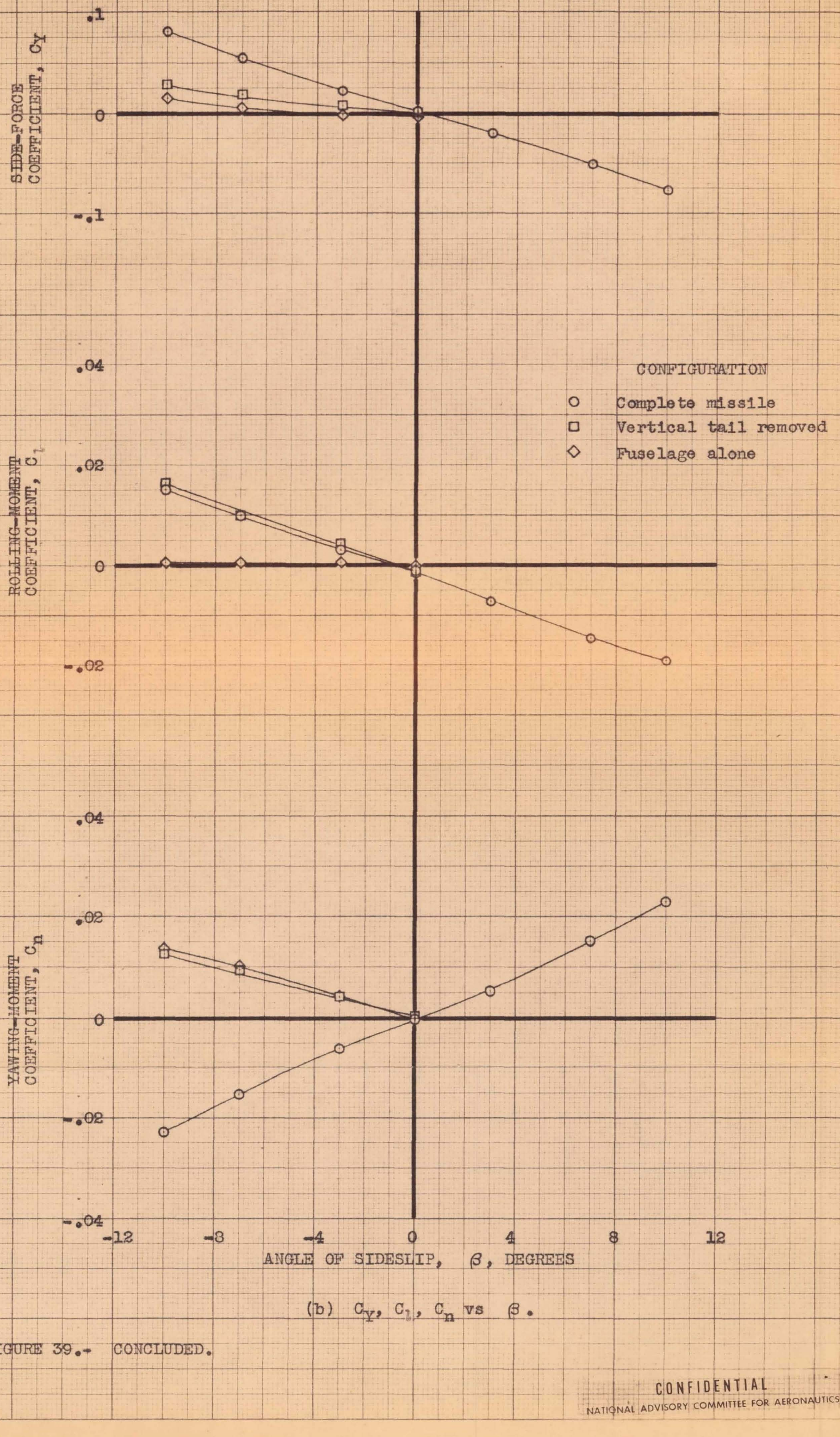

(b) C_Y, C_l, C_n vs β.

FIGURE 39.- CONCLUDED.

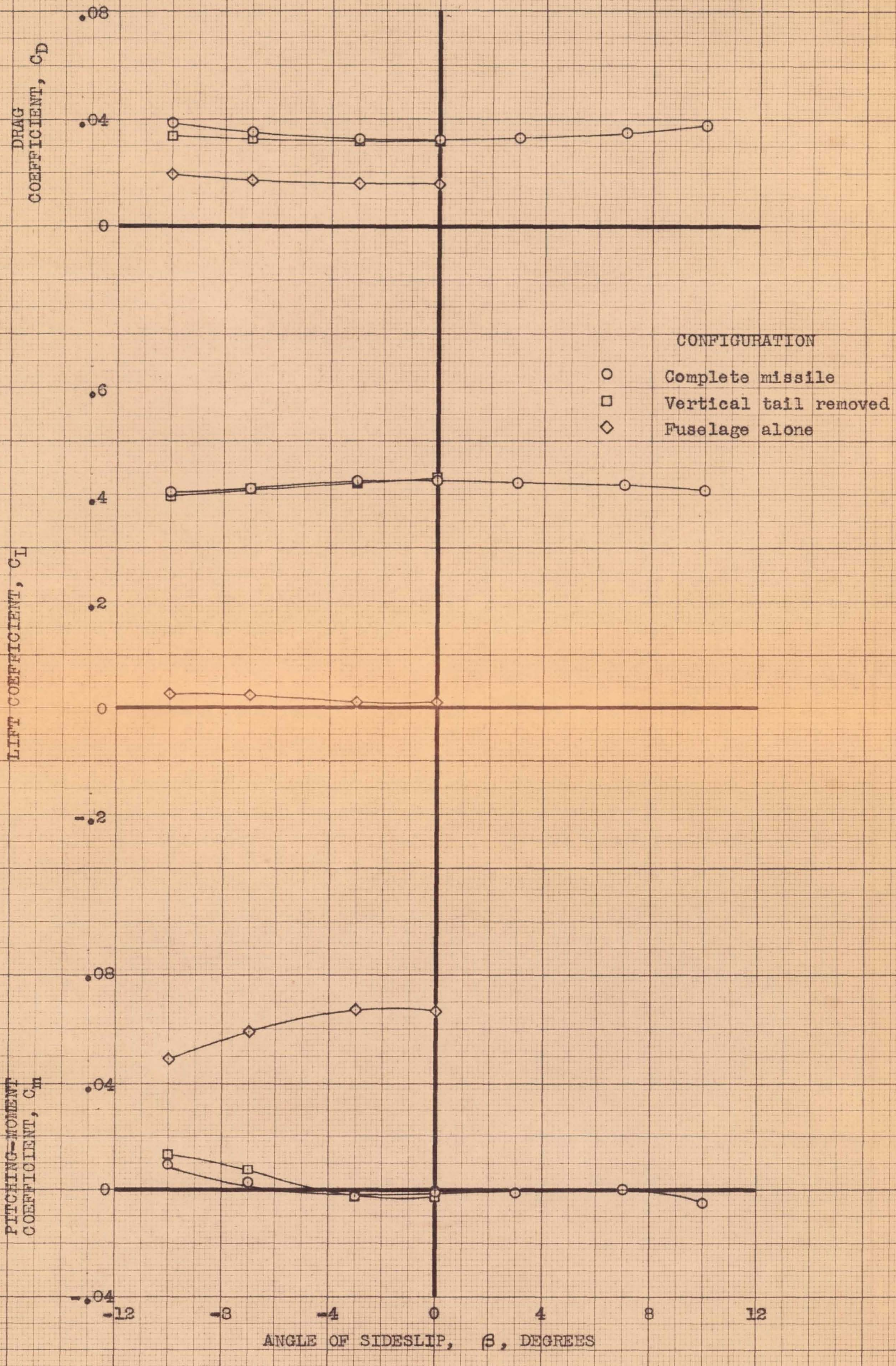

(a) C_D, C_L, C_m vs β.

FIGURE 40.- COMPARISON OF THE AERODYNAMIC CHARACTERISTICS IN SIDESLIP OF THE COMPLETE MISSILE WITH THE CHARACTERISTICS OF THE MISSILE WITH THE VERTICAL TAIL REMOVED, AND WITH THE FUSELAGE ALONE. R, 11×10^6; δ_e, 0°; α, 7°.

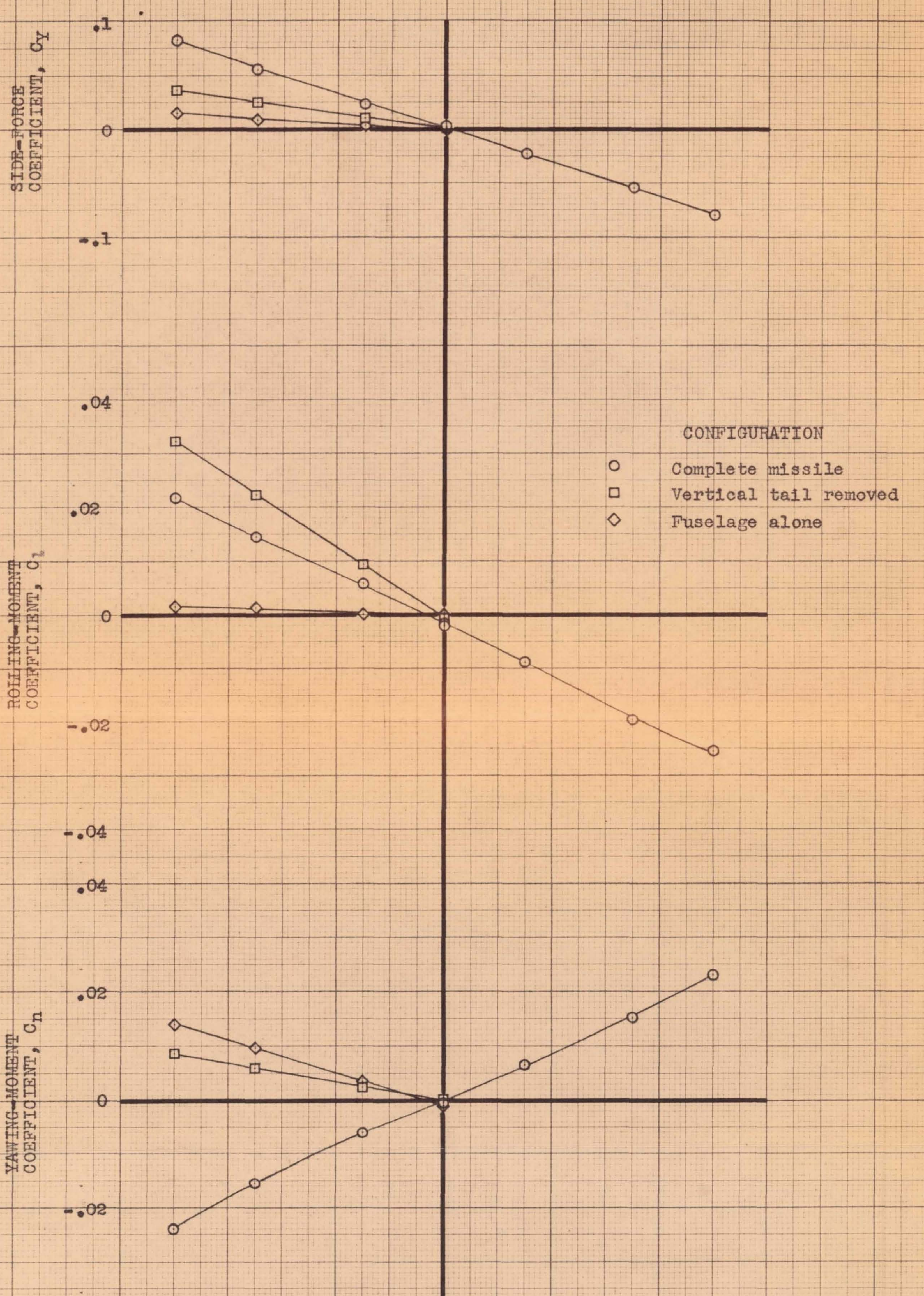

(b) C_Y, C_l, C_n vs β.

FIGURE 40.- CONCLUDED.

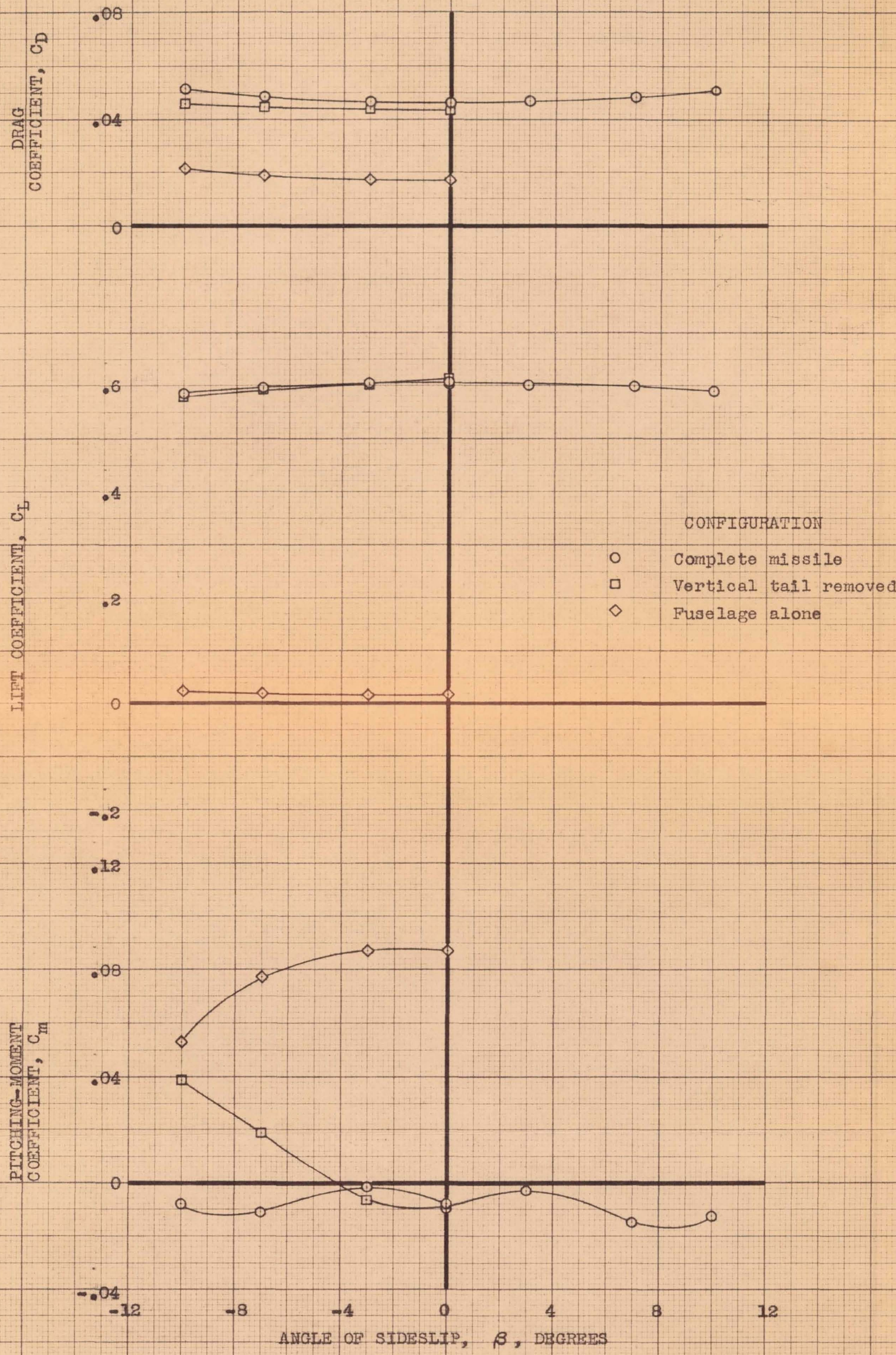

(a) C_D, C_L, C_m vs β.

FIGURE 41.- COMPARISON OF THE AERODYNAMIC CHARACTERISTICS IN SIDESLIP OF THE COMPLETE MISSILE WITH THE CHARACTERISTICS OF THE MISSILE WITH THE VERTICAL TAIL REMOVED, AND WITH THE FUSELAGE ALONE. R, 11×10^6; δ_e, 0°; α, 10°.

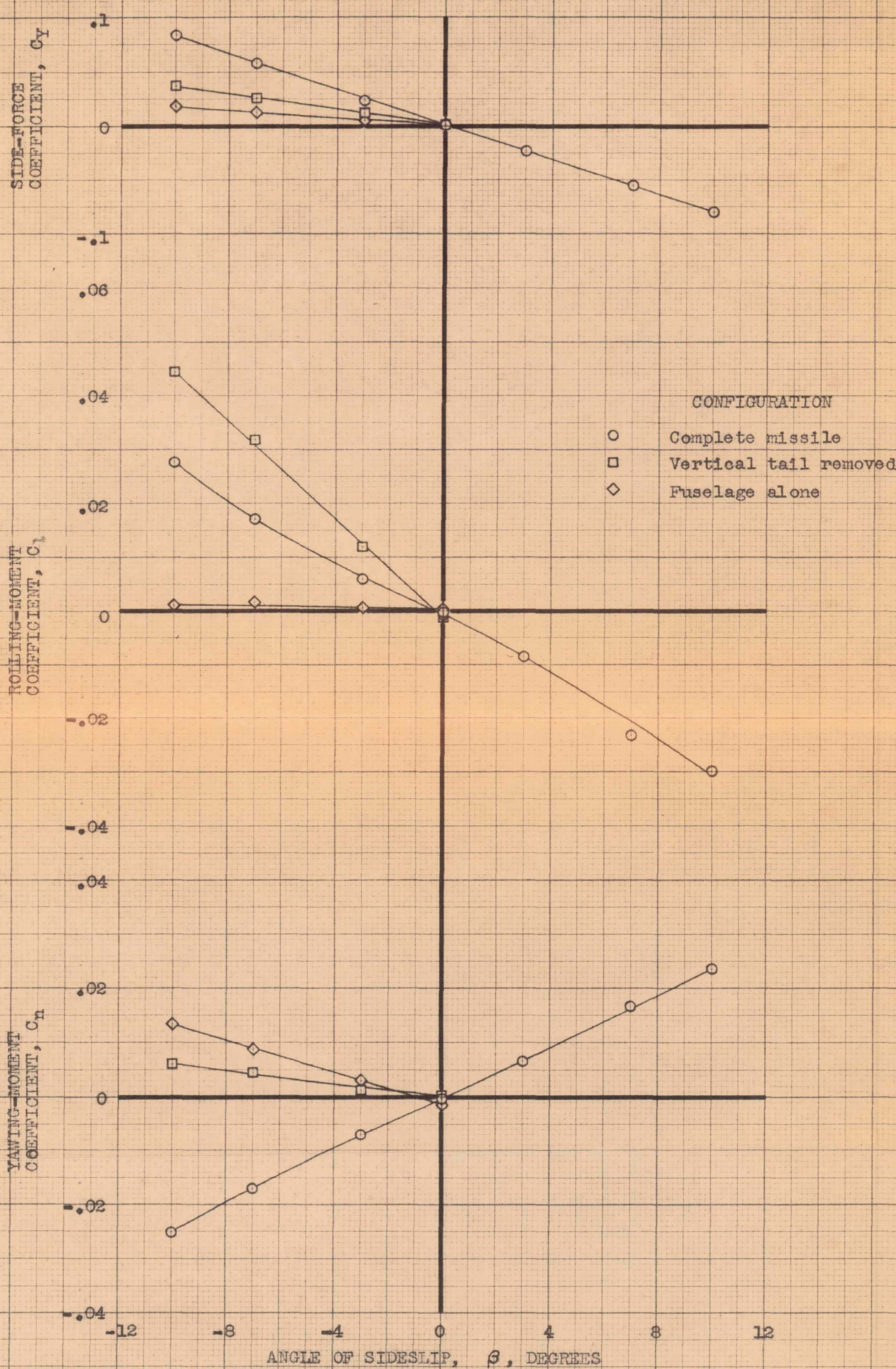

(b) C_Y, C_l, C_n vs β.

FIGURE 41.- CONCLUDED.